TOWARDS STABLE NANOLAYERS FOR EUV OPTICS

Cristina Sfiligoj

PhD Thesis, University of Amsterdam, June 2021

Towards stable nanolayers for EUV optics

Cristina Sfiligoj

ISBN: 978-94-92323-56-9

Cover design: Chiara Verdoliva

This thesis is printed on 100% recycled paper.

UNIVERSITEIT VAN AMSTERDAM

The work described in this thesis was carried out at the Advanced Research Center for Nanolithography (ARCNL), a public-private partnership between the Univer-sity of Amsterdam (UvA), the Vrije Universiteit Amsterdam (VU), the Dutch Research Council (NWO) and the semiconductor equipment manufacturer ASML

TOWARDS STABLE NANOLAYERS FOR EUV OPTICS

ACADEMISCH PROEFSCHRIFT

ter verkrijging van de graad van doctor
aan de Universiteit van Amsterdam
op gezag van de Rector Magnificus
prof. dr. ir. K.I.J. Maex
ten overstaan van een door het College voor Promoties
ingestelde commissie,
in het openbaar te verdedigen in de Agnietenkapel
op woensdag 30 juni 2021, te 16:00 uur

door
Cristina Sfiligoj
geboren te Chene Bourg

Promotiecommissie

Promotor:

prof. dr. J. W. M. Frenken	Universiteit van Amsterdam

Co-Promotor:

prof. dr. P. C. M. Planken	Universiteit van Amsterdam

Overige leden:

prof. dr. D. Bonn	Universiteit van Amsterdam
prof. dr. M. S. Golden	Universiteit van Amsterdam
prof. dr. M. D. Ackermann	Universiteit Twente
prof. dr. P. Rudolf	Universiteit Groningen
dr. R. Bliem	Universiteit van Amsterdam

Faculteit der Natuurwetenschappen, Wiskunde en Informatica

Table of Contents

1

Introduction

In 1973, science fiction writer Arthur C. Clarke presented his famous three laws on the nature of discovery and technology. Perhaps the best known is the third one, which states: "Any sufficiently advanced technology is indistinguishable from magic" [1]. With the development of nanotechnology, starting around that time and approaching its fiftieth birthday, today this observation rings even more true. Nanotechnology, the collection of devices working on the scale of ultrasmall dimensions, is invisible to the naked eye and even to the best optical microscopes, and yet it is immensely powerful and finds application in a diversity of fields. It is hidden in technologies we make use of on a daily basis, from computers to solar cells, as well as it constitutes a platform to explore new and exciting physics. One of the pillars below this advancement has been the continuous progress in device miniaturization.

The practical realization of a miniature device relies strongly on how well one can predict and control the properties of materials at the nanoscale. In fact, to assure that they function as intended, the devices should be fabricated sufficiently close to their designed structure and should remain sufficiently stable, also after prolonged operation. Thermodynamics [2], however, does not tend to favor artificially constructed structures – with abrupt changes in composition and atomically flat surfaces - particularly at such small scales. The drive towards thermodynamic equilibrium makes a system evolve towards lower-energy configurations, which often result in the deterioration of the structural properties of the device, and consequently of its efficiency, reliability and durability.

Since miniaturization is intrinsically accompanied by an increase in surface-to-volume ratio, the thermodynamic driving forces for these small structures are dominated by the properties of the surface. When designing a nanoscale device, therefore, the character of the surfaces acquires prominent importance, making it ever more necessary to understand how specific fabrication methods influence the structural and mechanical properties on the nanoscale.

One nanoscale geometry in which the surface-to-volume ratio is extreme, and so is its thermodynamic tendency to evolve, is that of ultrathin films (nanolayers) deposited on a substrate. As a result of this intrinsic thermodynamic driving force, a smooth surface may spontaneously transform in a landscape of mountains and valleys; two adjacent layers made of different materials may form a compound; a thin membrane may deform and ultimately break. Because of these reasons, nanolayers that may appear superior in theory, in practice may perform worse than those that appear slightly less promising, but are more stable thermodynamically.

The central focus of this thesis is on the stability of ultrathin metal films, both as single layers and as stacked systems. This subject is of general interest to a wide variety of applications in the context of nanotechnology. In this thesis, the specific choices of materials and structures that have been investigated were motivated by the ongoing work on nanoscale architectures found in the field of Extreme Ultraviolet (EUV) optics for next-generation photolithography. This particular application area is briefly described in Section 1.1. The other introductory sections aim to provide the main ingredients of thin film technology that are useful in view of the approaches to increase their thermodynamic stability, treated in this thesis. Specifically, in Section 1.2.1, we review the growth of thin films, with an emphasis on the two deposition techniques used in this thesis, namely e-beam evaporation and magnetron sputtering. In Section 1.2.2, the different types of interaction at the interfaces are reviewed and in Section 1.2.3 we introduce the build-up of stress in thin films.

1.1 Nanolayers for EUV optics

The miniaturization of devices that we have been witnessing in the course of the last century has been brought about largely by the enormous progress in a technology called photolithography. Photolithography, from the Greek words *photo* (light), *lithos* (stone) and *graphy* (writing) uses light to print images on semiconductor plates, which are then processed to create electronic circuits. The resulting devices, e.g. processor or memory chips, in turn, form part of an ever growing spectrum of applications, many of which we make use of on a daily basis, such as computers, smartphones and tablets, and many of which we are often not even aware of, such as components for watches, cars and household appliances. Thanks to the continued advances in photolithography, a continuously larger number of transistors can be fit in the same amount of space, leading to more powerful and faster chips.

But how can we create smaller and smaller electronic circuits, using the same concept of photolithography? We exploit the fact that light can have different wavelengths (infrared, visible, ultraviolet, etc.). Using shorter and shorter wavelengths, it is as if one can write with sharper and sharper pencils. State-of-the-art photolithography machines use extreme ultraviolet light, ($\lambda = 13.5$ nm) to write details with dimensions below 10 nm and ongoing developments in the optical system will introduce further improvements [3].

In an EUV lithography machine, as the one depicted in Figure 1.1, 13.5-nm light is generated by a powerful source (a CO_2 laser hitting a stream of 30 µm-diameter droplets of liquid tin) and then transported through a series of concave and convex mirrors that focus it, shape it and finally project it onto a semiconductor wafer. The exposed wafer, which is coated with a photo-sensitive polymer layer, is then processed using standard cleanroom techniques. This procedure is repeated several times, each time projecting a different geometrical pattern, in order to build up the complete, three-dimensional architecture of the semiconductor devices that are produced.

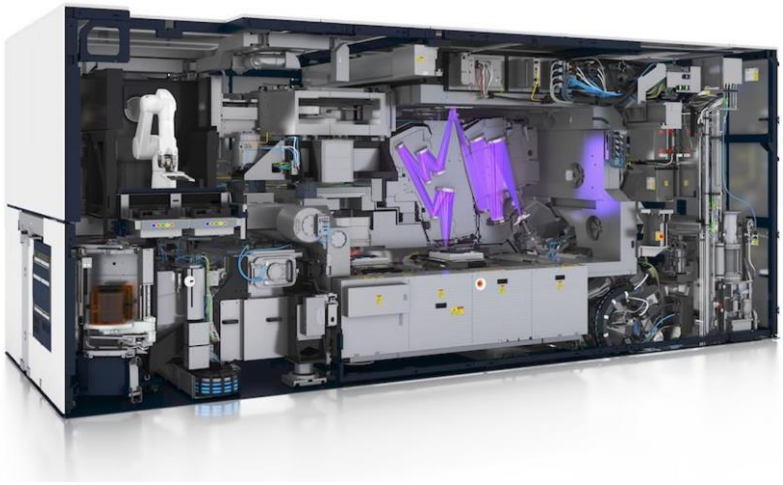

Figure 1.1 Artist impression of the inside of an NXE 3400 machine from the company ASML for photolithography with EUV light. The optical light path is indicated in purple, with the EUV source at the bottom right and the mask at the top. The entire machine has the size of a locomotive, and is operated under vacuum conditions (image source: ASML).

To use EUV light, a series of challenges need to be tackled. Among those [4]–[12], the manufacturing of highly efficient and stable optics occupies a central position. Nanolayers form a key ingredient in these special optical structures, and they form the focus of this thesis.

The basic optical elements that are employed in EUV photolithography machines are of two types (see

Figure **1.2**): mirrors, which work in reflection and are used to bounce off the light multiple times from the source to the wafer stage; and pellicles, which work in transmission and are used to block particles from landing on the so-called reticle, which is the patterned mirror, that acts as the mask in the lithography process. If a particle would land on the reticle, its silhouette would be projected on all copies of the pattern on the silicon wafer, thus potentially disabling all chips made with that reticle.

In the remainder of this section, we briefly review these two types of optics.

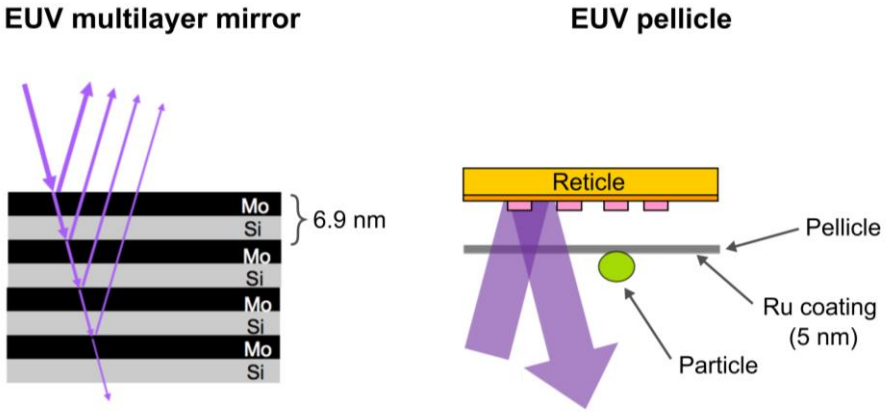

Figure 1.2 Cartoons of relevant nanolayers for EUV lithography-optics: the Mo/Si multilayer stack for 13.5 nm light reflection (left) and the Ru coating for reduced heating of transparent pellicles (right).

EUV mirrors. Mirrors are being used instead of refractive optics, for the simple reason that the absorption of EUV light is so strong that almost no EUV light would make it even through a single lens. EUV mirrors, however, are different from regular mirrors. In the mirrors in our bathrooms, for example, visible light (λ in the range 380-750 nm) reflects off a metal layer (silver, typically), protected with glass (a form of silicon oxide). The metal reflects because light waves shake the freely moving electrons in the metal, which absorb and reemit photons in the process. Glass, by contrast, lets most light pass through because its electrons are not free to engage in this process and they can therefore not interact much with visible light. EUV light, however, would fry this type of mirrors, because both silver and glass absorb heavily at the EUV wavelength. In fact, almost all matter strongly absorbs light with a wavelength of 13.5 nm (or, equivalently, a photon energy of 92 eV), even air (this is why the entire EUV photolithography machine shown in Figure 1.1 is enclosed in a chamber that can be brought to vacuum).

This problem is solved by using a technology that was invented in 1939 [13]. A metal and a dielectric layer are alternated multiple times to create a multilayer stack (left panel of

Figure **1.2**). For reflecting EUV light at normal incidence, the two materials are usually chosen to be molybdenum (Mo) and silicon (Si). These combine relatively low absorption coefficients with one of the largest relative differences in the index of refraction at this wavelength. The thickness of each Mo/Si bilayer matches half the wavelength of the light (6.9 nm, in this case). In this way, even though a single bilayer reflects only a small fraction of the EUV light, the reflections from all layers together interfere constructively, increasing the intensity of the specularly reflected beam at the proper wavelength. Using this solution, the efficiency of an ideal Mo/Si multilayer mirror (MLM) can reach a record value of 75 % [14].

EUV pellicles. These are membranes made of materials with a relatively low absorption at EUV wavelengths. They are made as thin as possible in order to limit absorption. Inevitably, however, part of the light gets absorbed and converted into heat. During operation, a pellicle can easily reach temperatures between 500 and 1000 °C. In order to remove as much heat as possible, ultrathin metallic films are used to coat these membranes. They are selected to combine a high infrared emissivity with a low EUV absorption coefficient, so that they efficiently radiate off the heat from the membrane, without contributing too much to further absorption of the EUV light. Ruthenium (Ru) coatings are commonly used for this purpose, with a typical thickness of 5 nm.

By design, both multilayer mirrors and pellicles are based on films that are only a few nanometers thick and where there is a sharp transition between layers of different materials. Such systems are inherently thermodynamically unstable. Intrinsic to their configuration there are forces that tend to drive the system towards equilibrium, by changes in either geometry or composition, or both.

As a result of these thermodynamic forces, in real, fabricated Mo/Si MLMs, for example, the ideally sharp and perfectly smooth interfaces become blurred and rough, while in real pellicles, the continuous Ru nanolayer spontaneously can form holes and ultimately break up into small beads [15]. Such effects represent a serious bottleneck for the performance of multilayer optics for EUV photolithography.

It is important to note that operation under the powerful EUV beam heats up the optical structures, which is a particularly strong effect for pellicles, as these are freestanding structures without any possibility to get rid of excess heat through thermal conduction. High temperatures accelerate the degradation processes just described.

The development of high-performance EUV optics requires a reliable prediction of and, ideally, a high degree of control over the stability of the nanolayers in these structures. The combination of the driving forces that they experience for evolution and the atomic mobilities by which they can respond to those driving forces, determine the rate at which their properties degrade and, thus, their lifetime. In this thesis, I explore how a role can be played in these matters by the precise methods by which the nanolayers are deposited and by the chemical 'affinity' between the materials that are combined in the structure. In the following sections, we will briefly review the main factors at play.

1.2 Film formation and evolution

When materials are deposited on a substrate in the form of atomic vapor, a film forms through a series of three stages (nucleation, grain growth and coalescence) that are governed by the interplay between thermodynamic driving forces and kinetic factors [16],[17].

For thin films, a dominant thermodynamic driving force is introduced by the minimization of the surface free energy γ (in units of J/m^2). There will be three possible modes of film growth, depending on the relative magnitudes of the surface energies of the deposited material, γ_f, the underlying substrate, γ_s, and the substrate-film interface, γ_i. The first two are (1) layer-by-layer growth, also referred to as "Frank-Van der Merwe" (FM) growth, where the film wets the substrate because $\gamma_i + \gamma_f < \gamma_s$, and (2) "Volmer-Weber" (VW) or island growth when $\gamma_i + \gamma_f > \gamma_s$, where three dimensional islands nucleate on the substrate and only coalesce in a later stage to form a closed film. When $\gamma_i + \gamma_f < \gamma_s$ and the deposit grows epitaxially on the substrate, taking over its lattice distances in directions parallel to the interface, the third mode is often observed, namely (3) "Stranski-Krastanov" (SK) growth, where after a number of closed layers, the growth proceeds with three-dimensional island formation, in order to

minimize the buildup of strain energy in the film due to lattice mismatch between the deposit and the substrate.

Together with the thermodynamic properties of the materials involved, also kinetic factors play a central role in film growth and these are in turn influenced by the process conditions. In the following, we will review the energetics of the two deposition techniques used to grow the thin films studied in this thesis, namely electron-beam evaporation and DC magnetron sputtering. Most metallic films grown on inert substrates using these two techniques follow a Volmer-Weber type of growth. The outcome is commonly non-equilibrium structures, either polycrystalline or amorphous.

1.2.1 Fabrication techniques – sputtering and evaporation

In a physical vapor deposition (PVD) process, such as evaporation or sputtering, atoms in the vapor phase have an initial average kinetic energy of $\frac{3}{2}\mathrm{k_B T_{source}}$. This energy is transferred from the newly arriving atom to the substrate within a few atomic vibrational periods, which is usually too short a time to contribute to significant surface migration of the atom [17],[18] and therefore can be safely ignored, under the assumption the combination of these arrivals has a negligible effect on the substrate temperature, T_{sub}.

The mobility of the atoms on the surface (adatoms) is instead mainly determined by the local energy barriers and the substrate temperature, through the Arrhenius equation for the diffusion coefficient, D [16]:

$$D = D_0 \, exp \frac{-E_a}{k_B T_{sub}} \tag{1.1}$$

Here, D_0 is the maximal diffusion coefficient (in m^2/s) and k_B is the Boltzmann constant (in $J/(mol \cdot K)$). E_a is the activation energy of diffusion. For the first arriving atoms, this will be their diffusion barrier over the energy landscape of the substrate material. Once the substrate is covered, this is replaced by the energy barrier for diffusion over the deposited material itself. The latter energy is typically in the order of one

sixth of the cohesive energy of the deposited material, which, in turn, is proportional to the melting point of that material [19],[20]).

In electron-beam evaporation, a material is evaporated from a source by use of an electron beam that is generated from a hot filament and steered via electric and magnetic fields towards the source. The process takes place in (ultra) high vacuum, so that the evaporated atoms have generally large mean free paths and retain their initial direction and energy in their trajectory from source to substrate. In an evaporation process, the the atoms arrive at the substrate with an energy similar to their initial thermal energy, in the order of ~ 0.1 eV) [16]

Evaporation is mostly advantageous for depositing films with low concentrations of impurities in the film and induced defects in the substrate, as it takes place in UHV and no energetic particles hit the growth substrate. One of the main drawbacks is, however, that not all materials can be evaporated. In particular, the deposition of low-vapor-pressure materials and compounds is difficult to achieve.

In magnetron sputter deposition, a target plate is bombarded with high-energy ions of an inert gas (typically argon, Ar). The magnetron, inserted in proximity of the target, provides two main advantages: first of all, for the same applied power, less inert gas is required to sustain the plasma, thereby decreasing the amount of gas trapped during film growth; secondly, negatively charged-, highly energetic-particles, such as ionized oxygen molecules or electrons, can be guided away from the growth substrate by the magnetic field that is oriented parallel to the target plane.

Using sputtering, in contrast to evaporation, any material can be deposited, provided that enough momentum is transferred from the ions to the target atoms. The energy distrubtion of ions generating from the plasma usually peaks around 1 keV and leads to the ejection of multiple target atoms per incident ion [21]. Some ions become charge neutralized when they hit the target and are reflected back retaining much of their intial kinetic energy. Note that these particles won't feel the magnetic field, and possibly will reach the growth substrate, where they can create defects upon impact.

The typical average kinetic energy of the sputtered atoms is around 10 eV, which is much larger thant the thermal value of ~ 0.1 eV for evaporated

atoms. For a given system geometry and plasma power, the angular and energy distributions of the sputtered atoms is determined by the pressure of the working gas (in the order of a few µbar). At high pressures (~ 10 µbar), the sputtered atoms thermalize with the gas atmosphere before reaching the substrate, thereby significantly reducing their initial energy and spreading their angular distribution. At low pressures (~ 1 µbar), the target atoms retain much of their initial energy and direction. This energy is enough to cause 'knock-on' sputtering at the substrate, of either the already deposited atoms or of substrate atoms.

E-beam evaporation and sputter-deposition are therefore intrinsically different and produce films with different structural and mechanical properties. Extensive reviews on this topic can be found, for example, in the books of Ohring [16] and Smith [18]. In Figure 1.3 we summarize the main energetics aspects.

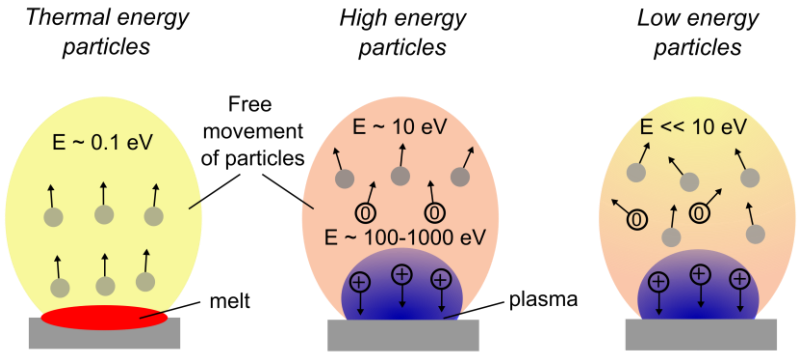

Figure 1.3 From left to right: principle of e-beam evaporation, magnetron sputtering at low and high deposition pressures (figure reproduced after [14]).

In both cases, additional treatments can be used to deliberately alter the growth. For instance, wetting of the substrate can be assisted by increasing γ_s or decreasing γ_f. The former can be achieved, for example, by creating dangling bonds at the surface through low-energy irradiation [22]. On the other hand, the surface of the film can be deactivated using surfactants, such as tin [23].

Another powerful way to influence the growth is through kinetic factors, such as the substrate temperature, which influences the mobility of the adatoms on the surface, and thus, the growth [16],[18].

1.2.2 Interfaces

As films become thinner, the interface regions occupy a larger fraction of the total volume and therefore their contribution to the overall stability of the layer becomes more important. Often it is desired to have films with sharp interfaces, even though such a configuration is often far out of equilibrium: most materials, when in contact, have the tendency to interact, and blur out any abrupt transition - either via interdiffusion or compound formation. This process is driven by the reduction in Gibbs free energy, ΔG , which can be obtained entropically, i.e. through the randomization in structural order, and energetically, via the release of interaction energy. When ΔG is negative the system will have a strong tendency to evolve, while when ΔG is positive for all possible changes in film and interface structure, the system is already in a stable configuration. In general, the magnitude of ΔG for a rearrangement indicates how far a state is from equilibrium. The processes at the interface via which the free energy can be reduced are illustrated in Figure 1.4.

Both processes illustrated in Figure 1.4 arise due to diffusion of atoms across the interface. The extent of interaction between materials is hard to predict, as interdiffusion depends on several factors, such as surface energies, structure, mechanical strain, and defects. However, the type of interaction can be predicted by looking at the corresponding phase diagrams. A weak degree of interaction is represented in the central panel of Figure 1.4. In this case the two elements do not prefer any specific compound together, but they are miscibile with each other and can form so-called “solid solutions”: atoms of one material are incorporated into the other by replacing an atom in the lattice (substitutionally), or by fitting into the space between atoms (interstitially). As a result, the crystal structures of the two materials do not change, but their physical properties exhibit a continuous variation over the interface region [24]. This often happens when two materials are close to each other in the periodic table. Interdiffusion can be asymmetric, meaning that one material can migrate

into the other, but not viceversa. Such a situation would be represented by the case in central panel of Figure 1.4, in which the oppositely pointing arrows would differ in size, indicating different diffusion coefficients.

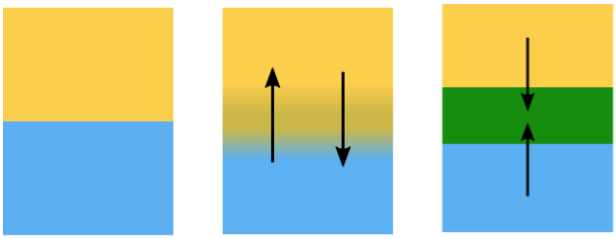

Figure 1.4 Types of interaction at the interface between two materials (arrows indicate the direction of movement of the atoms): no interaction (left); interdiffusion (middle); formation of stable compound (right).

Many pairs of elements react to form compounds rather than just interdiffuse. This situation is illustrated in the right panel of Figure 1.4. A well-defined chemical compound can be formed for various reasons. Often, compounds result when the electronic configuration of the participating elements is very different. This is the case for elements that are further apart in the periodic table, such as metal silicides, which form strong covalent bonds [25]. In other cases, the materials are not very different from an electronic perspective, e.g. two metals, but the atomic sizes are so different that they like to form specific geometrical arrangements, corresponding to specific compounds. In a binary phase diagram, stable compounds are indicated as vertical lines, as shown for example in the phase diagram of Ru-Si in Figure 1.5. When multiple compounds appear in the diagram, the combination of the thermodynamic preference and the competition between the deposition and the diffusion kinetics determines whether all or only some of these form at a film interface between the two pure materials of the diagram. In the particular case of Ru-Si, we note that the two materials can form three stable compounds (silicides), while the solubilities of Ru in Si and Si in Ru appear negligibly low.

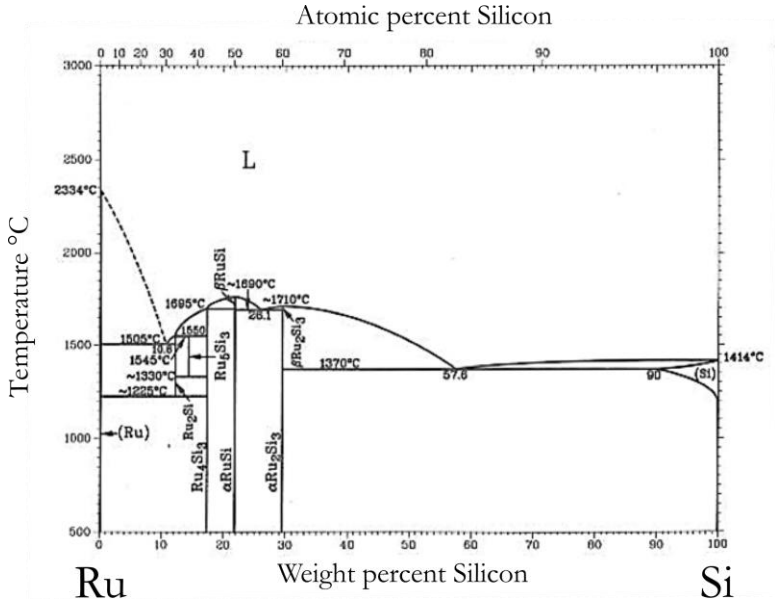

Figure 1.5 Binary phase diagram of Ru-Si [26].

To prevent reactions at the interface, for example in a multilayer mirror of thin Mo and Si films, diffusion barrier layers can be used. They form the ultimate strategy to separate the thermodynamic and kinetic aspects of the thin-layer system. Even for a system in which the thermodynamics would be strongly in favor of intermixing or compound formation at the interface, an effective, intermediate layer may completely prevent the two materials from reaching each other. The best choice for such a diffusion barrier layer is a compound with a negative ΔG with respect to compound formation with either of the two materials that it is supposed to separate, so that it will not react, and with a dense structure, so that it will block interdiffusion of the two. As an example, the spontaneous oxidation in air of some materials leads to the formation of a thin oxide that serves as a robust barrier against further oxidation and against interaction with other materials. In the case of Mo-Si MLMs, often thin B_4C-layers are used for this purpose. Next to the advantage of such intermediate films for preventing the interaction between Mo and Si, are the disadvantages that these films do not add to the ideal constructive interference of the reflections of the sequence of interfaces and that they absorb a modest, but noticeable fraction of the EUV light.

1.2.3 Stress

Virtually all thin films are in a stressed state, even when there is no external load applied to them. The stress in a thin film deposited on a substrate may be tensile (i.e., the film tends to contract in one or both directions parallel to the substrate surface) or compressive (i.e., the film tends to expand in one or more directions parallel to the substrate surface). Such stress can be due to the structural inhomogeneity within the film itself and the forces exerted between the film and the substrate.

The stress can be categorized as extrinsic or intrinsic. Intrinsic stresses develop during the deposition process, for example due to the accumulating effects of crystallographic flaws within the film. These flaws can be the consequence of the specific growth mechanism, including kinetic factors [27],[28] – and can therefore be closely linked to the film structure. They can also be the result of the misfit, either induced by the difference in lattice parameter between substrate and coating, or by the presence of interstitial or substitutional defects. Extrinsic stresses, on the other hand, arise after the deposition, for example as the result of the change in temperature between the manufacturing of the film and the conditions under which the film is, when there is a difference in thermal expansion coefficients between the coating and the substrate.

The presence of residual stress in thin films is usually undesirable, although there are cases where it can be beneficial. Tempered glass is an example of a material made tougher by inducing compressive stress at the surface, while the bulk is under tension. In most cases, however, stress is detrimental for applications. Film cracking, delamination, void formation and blistering may all be related with film stress.

The macroscopic manifestation of the build-up of stress in thin films is substrate bending, which is in fact the quantity often measured for monitoring the stress. To explain this effect, we consider a film on a substrate that is not rigid. The stress in the substrate will have to follow and compensate the one in the film. As in the equilibrium state the total force and the total bending moment must be zero, the substrate necessarily bends to balance the forces induced by the constraining film. The behavior of the film-substrate system is represented schematically in Figure 1.6 [16].

In Figure 1.6-a), the film would like to shrink relative to the substrate, however it is firmly connected to the substrate. It is thus forced to be stretched with respect to its preferred dimensions and the substrate contracts accordingly. The compressive forces in the substrate counteract the tensile forces in the film. As a result of these opposing forces, the film-substrate system bends to bring the system to equilibrium. Thus, films containing internal tensile stresses bend the substrate concave, which is upward in the schematic of Figure 1.6-a. Equivalently, compressive stress develops in films that would prefer to expand relative to the substrate and makes the substrate bend convex, i.e. downward in Figure 1.6-b.

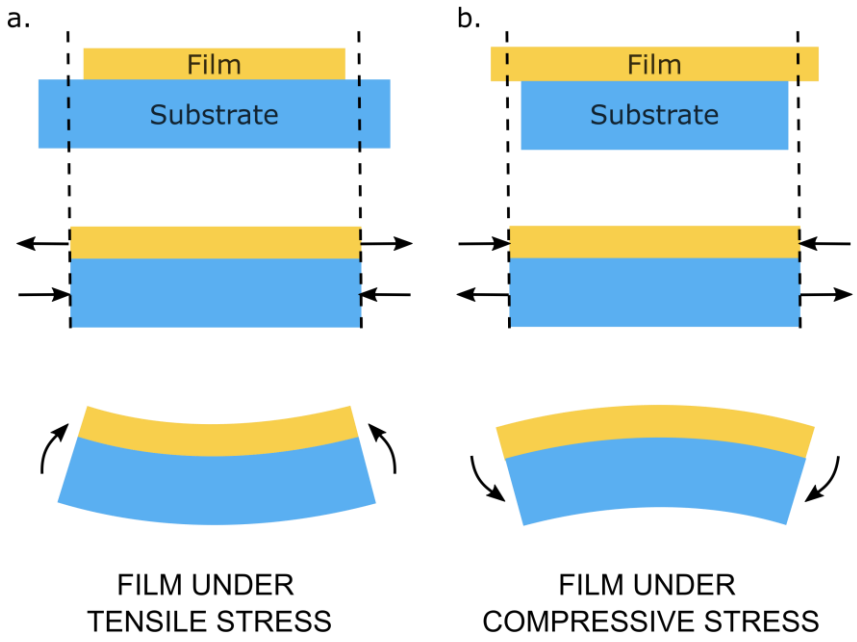

Figure 1.6 Evolution of film/substrate cross-section under the load of a) tensile and b) compressive stress in the film [16].

For thicknesses of the film much smaller than the thickness of the substrate, one can easily derive the stress in the film σ_f from the measured radius of curvature, as described by Stoney's equation [29]:

$$\sigma_f = \left(\frac{Y_s}{1-\nu_s}\right)\frac{t_s^2}{6t_f R} \tag{1.2}$$

Here, t_s and t_f are the thickness of the substrate and film, respectively, and R is the radius of curvature. The substrate's Young's modulus Y_s and its Poisson ratio ν_s determine how strongly the substrate responds to the stress, exerted by the film. The sign of R directly reflects whether the stress is tensile ($R > 0$) or compressive ($R < 0$).

Equation 1.2 describes the macroscopic behavior of a film deposited on a substrate. However, although we will not review this here, it is important to note that stress is not necessarily homogeneous throughout the film. This can manifest itself as a variation as a function of depth within the film. But, in addition, most materials have a polycrystalline structure, in which each individual grain contributes its own distribution of internal forces. This also leads to variation in stress in directions parallel to the plane of the film. The first measurement of the microscopic distribution of internal stress has been performed only recently, by means of AFM [30].

1.3 This thesis

In this thesis, we present our materials-science approach towards improving the stability of nanolayers, with specific attention to the challenges in the context of the optics in EUV lithography machines. In Chapter 2, we review the materials that can be used in the context of EUV multilayer mirrors and propose an alternative solution. In Chapter 3, we investigate the link between sputter-deposition conditions, in particular the working gas pressure, and the initial film structure and thermal stability of Ru nanolayers. In Chapter 4 we present the working principle and the performance of our novel STM-MOSS setup, a powerful tool for the investigation of the origin of intrinsic stress in thin films, e.g. of Ru nanolayers deposited by e-beam evaporation.

2

Effect of Rb incorporation on the EUV optical properties and intermixing in Mo/Si multilayer mirrors

High reflectivity and long-term stability in multilayer mirrors (MLMs) are crucial for EUV photolithography applications. The conventional base stack to reflect 13.5 nm light is a Mo/Si multilayer, which offers a maximum theoretical reflectivity of 75%. In practice, however, the efficiency of the mirror is strongly affected by intermixing between Mo and Si. Diffusion barriers have therefore been adopted, which nevertheless do not provide a perfect solution. In this work, we propose to suppress intermixing in Mo/Si MLMs by substituting the pure Si with a Si compound that can ensure higher thermodynamic stability, while simultaneously providing comparably high EUV theoretical reflectivity, with the net effect of increasing both reflectivity and lifetime. Our theoretical calculations indicate that rubidium silicide is the most promising material for this purpose. We estimate the optical and thermodynamic properties for each phase of rubidium silicide, and we show that Mo/Rb12Si17 provides the highest theoretical reflectivity, while Mo/RbSi is the most thermodynamically stable. The suppression of intermixing in Mo/RbSi MLMs should lead to a maximum reflectivity at least 2% higher than the best Mo/Si MLMs, integrated with diffusion barriers. The proposed Mo/RbSi MLM solution has the potential to increase the total EUV lithography throughput by ~50%.

2.1 Introduction

Molybdenum and silicon (Mo/Si) multilayer mirrors (MLMs) are to date the most viable technology to construct the optics systems for extreme-ultraviolet lithography (EUVL). The choice of Mo and Si as materials for the bilayers is mainly motivated by their high optical contrast and their low absorption at the EUV wavelength of 13.5 nm, adopted by the semiconductor industry. For Mo/Si MLMs, a theoretical peak reflectivity of 75% can be calculated [14], but in practice the maximum efficiency that can be achieved is only 69.5% [31]. Given that in EUVL machines, 10 mirrors are used in series to project a pattern onto a wafer, this value for the reflectivity implies that at best only $\sim$ 3% of the original radiation reaches the end-stage. Improving the reflectivity of each MLM by as little as 1% would lead to a $\sim$ 15% increase in the total EUVL throughput, accelerating the production speed and reducing the costs. Much effort has therefore been devoted to the suppression of the effects responsible for the deficit in experimental reflectivity.

The primary factor for the loss in reflectivity in Mo/Si MLMs is the intermixing between Mo and Si at the interface. Previous studies have shown that the interface sharpness can be improved via grazing-incidence ion bombardment. While this technique is very effective in reducing the roughness of freshly deposited layers, it does not suppress the tendency of the bilayer constituents to diffuse and form compounds.

For that purpose, ultra-thin diffusion barriers have been integrated in Mo/Si MLMs and an experimental reflectivity as high as 71% could be obtained [3–5]. This method, however, presents two major limitations that prevent higher performance from being achieved. First of all, the additional layers introduce unwanted absorption and reflections, and secondly, these films are too thin to entirely prevent intermixing between Mo and Si, particularly at elevated temperatures and under the load of power flux of photons and particles [6], [7].

An alternative strategy to improve the quality of the interfaces in MLMs is to reduce the thermodynamic driving forces responsible for the intermixing, which can be achieved by substituting the pure bilayer

constituents with compounds. Several studies have investigated the use of Mo-based materials [37],[38], demonstrating that by using Mo_2C or $MoSi_2$ instead of Mo the thermodynamic stability of the multilayer could be improved. Nevertheless, the experimental reflectivity of these mirrors remained lower than that of Mo/Si MLMs integrated with diffusion barriers, due to inferior optical properties of the added elements.

To our knowledge, the use of Si compounds has not been investigated yet in the context of MLMs. In this work, we show that by introducing Rb in the Si layer an overall efficiency superior to current best Mo/Si MLMs integrated barriers can potentially be achieved. Singh and Braat [39] have already proposed the incorporation of Rb in the form of RbCl to the Si layer. However, we are the first to study Rb_mSi_n compounds and to highlight the effect of using Si-based materials to increase the thermodynamic stability in MLMs, via suppression of intermixing. The choice of rubidium silicide is the result of an extensive search of the optical properties of all elements in the periodic table that could form a compound with Si while maintaining their EUV reflectivity comparable to that of standard Mo/Si MLMs.

2.2 Rubidium as additive to silicon in Mo/Si MLMs

To improve the performance of Mo/Si MLMs, we scrutinized possible compounds of Si that could simultaneously provide high EUV theoretical reflectivity and reduce the intermixing with Mo. In this search, we first calculated the EUV reflectivity for several elements X of the periodic table. In Table 2.1, we report the materials giving the highest MLM peak reflectivity, Peak1, at a wavelength of 13.5 nm and normal incidence. The reflectivity was calculated using the software IMD [40], designed for modeling the optical properties of multilayers. In all calculations, we set the number of bilayers $N = 100$. We optimized the bilayer period, $d = d_{Mo} + d_X$, and the thickness fraction of Mo, $\Gamma = d_{Mo} / d$, so that, at the given wavelength, the reflectivity is maximal. The roughness σ was set to zero for all interfaces, corresponding to ideally flat and sharp interfaces. Since for the conventional EUVL sources (of the tin-based laser-produced plasma type) the peak of the emission spectrum around 13.5 nm is much broader than the full width at half maximum of a typical MLM reflectivity

profile (see *Appendix A*) [41], not only the peak reflectivity is relevant in the context of maximizing the total EUVL throughput, but also the width of the reflectivity peak.

Table 2.1 Theoretical maximum reflectivity in Mo/X MLMs (for a selection of elements X) at 13.5 nm and normal incidence, assuming perfectly sharp and smooth interfaces. Columns *Peak1*, *NrInt1* and *NrInt10* indicate respectively the peak reflectivity of a single MLM, and the normalized integrated reflectivities of a single MLM and a combination of 10 MLMs in series [42]. The density ρ, the multilayer period d and the Mo/X thickness ratio Γ are also listed. See *Appendix A* for the complete reflectivity profiles.

	MLM parameters			Reflectivity [%]		
Mo/	ρ [g · cm^{-3}]	d [nm]	Γ	*Peak*1	*NrInt*1	*NrInt*10
Si	2.33	6.89	0.38	75.3	100	100
Rb	1.53	6.86	0.30	81.2	89.8	172.4
Be	1.85	6.92	0.36	74.3	86.9	74.3
Sr	2.64	6.94	0.36	74.2	83.2	68.7
K	0.86	6.94	0.40	71.2	92.0	53.5
Ba	3.51	6.98	0.51	66.1	107.5	28.8
La	6.16	6.97	0.47	64.9	98.5	24.6
Ca	1.55	8.00	0.60	58.6	70.5	6.3
Y	4.47	5.56	0.58	55.6	58.3	3.1
Pr	6.77	7.08	0.51	50.5	62.4	1.3
Li	0.53	7.09	0.54	47.8	69.3	0.9
Zr	6.52	7.07	0.45	44.7	34.9	0.2

For a single mirror, the integral of the reflectivity peak should thus be regarded as the more relevant quantity. We therefore included in Table 1 the quantities *NrInt1,* which represents the normalized integral for a single MLM, and *NrInt10*, which represents an optical system with 10 MLMs in

series [42]. Note that the *NrInt10* value contains the effects of both peak height and width on the total throughput of the lithography machine. In our calculations, we aim to find the multilayer mirrors with the highest *Peak1,* as it provides the most substantial contribution to the throughput of EUV light after multiple reflections.

As Table 2.1 illustrates, Mo/Rb MLMs show the highest peak reflectivity (Peak1 = 81.2%). Accordingly, their normalized integrated reflectivity after 10 consecutive reflections is the highest, more than 70% higher than the theoretical *NrInt10* value for Mo/Si MLMs. Despite these superior optical properties, elemental Rb is not a practical option for EUVL, due to its low melting point (39.3 °C), high vapor pressure at room temperature (2.85×10^{-5} Pa) and strong chemical reactivity. All other combinations in Table 1 perform less well than Mo/Si MLMs. For the scope of our work, however, material combinations with a theoretical reflectivity of at least 70%, such as Be, K, Sr and La, are interesting to be investigated as additives to the Si layer.

All these materials are known to react with Si and form various silicide phases, with the exception of beryllium [43]. Beryllium has been successfully used as a diffusion barrier between Mo and Si, leading to a record EUV reflectivity [34]. However, a hypothetical Be-Si mixture would be thermodynamically unstable and, hence, prone to spontaneous segregation. We therefore excluded such mixtures from the following discussion.

From Table 2.1 we selected the elements X = rubidium (Rb), strontium (Sr), potassium (K), and lanthanum (La), which have the highest *NrInt10* values in their chemical groups. For the silicides of these elements, we calculated the reflectivities of the corresponding Mo/X_nSi_m MLMs. In these calculations, we assumed all interfaces to be perfectly sharp and flat and we took the densities of X_nSi_m films from their crystalline forms, acquired from X-ray diffraction measurements.

As shown in Table 2.2, most Mo/XnSim MLMs give lower theoretical peak reflectivities than the best thinkable Mo/Si MLM, and all of them give lower integrated reflectivities. The fact that Mo/RbnSim shows a theoretical reflectivity lower than Mo/Si - even though the reflectivity for Mo/Rb was higher (see Table 2.1) - should not come as a surprise. In fact,

the EUV reflectivity is the highest when the absorption coefficients of the bilayer constituents are minimal, and the optical contrast between the two is maximal. Defining the complex refractive index as $n = 1 - \delta + i\beta$, in order to achieve the greatest refractive index contrast at the interfaces with Mo, we should thus substitute Si by a material for which the optical constants δ and β are as low as possible. Note that a low value of β is also favorable for minimizing the absorption. In the EUV regime, the refractive index n of a compound can be approximated as a linear combination of the real and imaginary atomic scattering factors of its elemental constituents f_{1j} and f_{2j} [40]:

$$n = 1 - \frac{r_0 \lambda^2 \rho N_A}{2\pi} \frac{\sum_j x_j \left(f_{1j} - i f_{2j}\right)}{\sum_j x_j M_j} \tag{2.1}$$

Here, $r_0 = e^2/4\pi\varepsilon_0 m_e c^2$ is the classical electron radius, λ the wavelength, and N_A Avogadro's number. We chose a form of this expression in which the mass density of the compound ρ appears explicitly, in combination with the molar masses M_j and compositional fractions x_j of the constituents.

Table 2.1 and Table 2.2 show that the density of Rb_nSi_m is greater than that of either Rb or Si. From Equation 2.1, we see that this makes the refractive index of the silicide deviate further from unity, reducing the optical contrast with Mo. In turn, the EUV reflectivity of the silicide-based MLM becomes lower than that of Mo/Si. For the same reason, also for K and Sr, the theoretical reflectivity values of the corresponding Mo/X_nSi_m MLMs are lower than those of Mo/X MLMs. By contrast, Mo/LaSi and Mo/$LaSi_2$ show higher reflectivities than Mo/La, as their densities are lower than that of La.

As mentioned before, the replacement of the Si layer with a silicide is motivated by a reduction in thermodynamic driving force towards intermixing. If the intermixing is suppressed sufficiently, a Mo/X_nSi_m MLM could in principle reach a reflectivity higher than the current best Mo/Si MLM integrated with diffusion barriers. This is suggested in Table 2.2, in particular for three Mo/Rb_nSi_m MLMs with different silicide compositions. We therefore focus the remainder of our discussion on the Mo/Rb_nSi_m system.

Table 2.2 Theoretical maximum reflectivities of Mo/*X*Si MLMs at 13.5 nm wavelength and normal incidence, with X = Rb, Sr, K and La, assuming perfectly sharp and flat interfaces. Columns *Peak1*, *NrInt1* and *NrInt10* indicate respectively the peak reflectivity of a single MLM, and the normalized integrated reflectivities of a single MLM and a combination of 10 MLMs in series [42]. The mass density ρ, the multilayer period d and the Mo/X layer thickness ratio Γ are also listed. See *Appendix A* for reflectivity profiles.

	MLM parameters			Reflectivity [%]		
Mo/	ρ [g $\cdot$ cm^{-3}]	d [nm]	Γ	*Peak1*	*NrInt1*	*NrInt10*
Si	2.33	6.89	0.38	75.3	100	100
RbSi	2.72 [44]	6.92	0.36	74.9	89.4	82.7
$Rb_{12}Si_{17}$	2.53 [45]	6.91	0.36	75.6	91.5	92.4
Rb_6Si_{46}	2.76 [46]	6.91	0.38	73.9	95.1	79.6
Sr_2Si	3.40 [47]	6.97	0.39	70.4	80.4	41.0
SrSi	3.50 [47]	6.97	0.39	70.1	81.8	40.0
$SrSi_2$	3.42 [47]	6.96	0.4	70.6	85.7	45.3
KSi	1.78 [44]	6.99	0.44	66.0	86.2	24.5
$K_{12}Si_{17}$	1.76 [46]	6.97	0.43	67.8	89.2	32.9
K_8Si_{46}	2.46 [48]	6.94	0.42	69.6	92.8	44.0
La_5Si_3	5.75 [49]	6.98	0.47	64.3	91.1	20.5
LaSi	5.10 [49]	6.97	0.45	66.0	93.1	26.9
$LaSi_2$	5.04 [49]	6.97	0.45	66.2	93.2	27.8

Literature on the properties of rubidium silicide is rather scarce. Two main equilibrium crystal structures are known, depending on the concentration of Rb. The clathrate phase (Rb content $< 10\%$ at.) consists of Rb^{+1} cations, encapsulated in Si_{20}, Si_{24} or Si_{28} cages [48],[50]. The Zintl phase (Rb content 40 - 50 at.%) consists of Si_4^{-4} or Si_9^{-4} Zintl clusters, surrounded by Rb^{+1}

cations [44],[45]. The clathrate phase, Rb_6Si_{46}, and the two Zintl phases, RbSi (also known as Rb_4Si_4) and $Rb_{12}Si_{17}$, are the most common ones.

In either phase, Rb_nSi_m presents several favorable properties over elemental Rb. First of all, the decomposition temperatures of Rb_6Si_{46} and RbSi are reported to be 803 K [50] and 623 K [51] respectively, which are considerably higher than the melting point of Rb. Secondly, while Rb violently reacts with air, the clathrate phase is reported to be as stable as pure silicon [50]. The two Zintl phases are reported to be highly unstable in contact with air [51]. However, this would not render their application in EUVL impractical since capping layers could be used to separate them from the ambient. In addition, the EUV MLMs are fabricated and operated under vacuum conditions. Hence, by implementing proper preparation and handling procedures, all Mo/Rb_nSi_m combinations mentioned in Table 2 could constitute valid options for EUVL.

In our study, we assume the silicide phases to be in a crystalline form. However, typical layers of as-deposited EUV MLMs are amorphous or polycrystalline. Although in the EUV regime the optical constants of a material can be assumed to be independent of the relative arrangements of its atoms, the mass densities ρ of amorphous phases are usually somewhat lower than their ideal crystalline counterparts. For example, the density of amorphous Si is 1.8% less than that of crystalline Si [52]. As discussed above, a decrease in density would lead to an enhanced reflectivity (see Equation 2.1). Using the IMD software, we calculated that a 2% reduction in the density of RbSi from its crystalline value of 2.72 g cm^{-3} would increase the *Peak1* reflectivity of Mo/RbSi by approximately 0.25%. Despite this favorable contribution, for the remaining of our analysis we will disregard the effect of density deviations since it is expected to be modest in comparison with the other factors (e.g. suppression of intermixing).

In the following sections we give estimates for Rb_nSi_m of the optical constants, the thermodynamic stability and the reflectivity of Rb_nSi_m/Mo MLMs.

2.2.1 EUV optical properties

In Figure 2.1 we show the complex index of refraction as a function of photon energy for the three materials of interest - Mo, Si, and Rb. The real $(1-\delta)$ and imaginary component (β) are represented in red and blue respectively, and have been calculated using reference [53]. The optical properties of the Rb and Si atoms in the silicide, however, are not the same as those in the individual elements. In fact, when a compound is formed, it is known that the electronic energy levels of the constituent atoms are shifted [54]. Even though this chemical shift is usually ignored (as in Equation 2.1), the scattering factors that determine the optical properties of the compound can be strongly affected. In what follows we explore the effect of the chemical shift on the EUV reflectivity in Mo/ Rb_nSi_m MLMs.

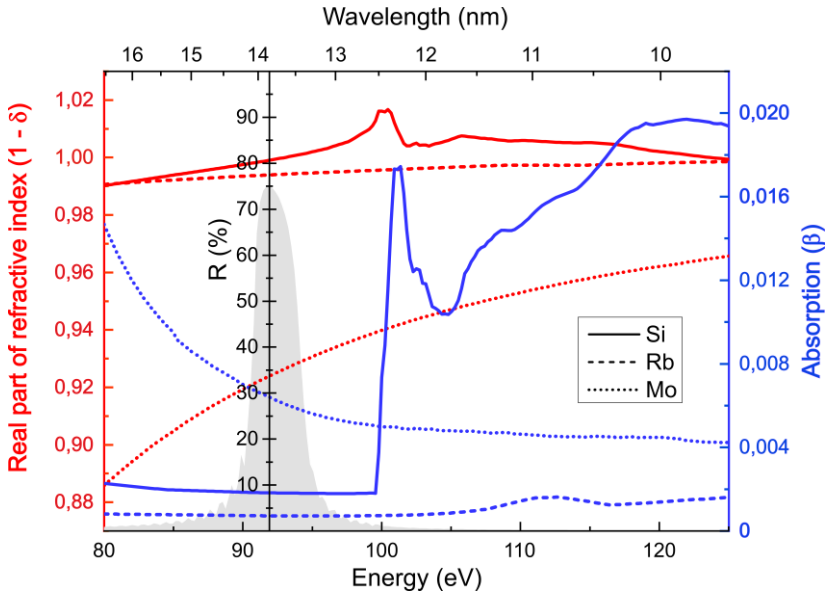

Figure 2.1 Real (red) and imaginary component (blue) of the index of refraction in the vicinity of 13.5 nm (91.8 eV), for Si (solid lines), Rb (dashed lines) and Mo (dotted lines). The gray area represents the calculated reflectivity profile of a single Mo/Rb_nSi_m MLM.

In the case of Rb_nSi_m, the chemical shift undergone by Si is expected to be negative, as the low electronegativity of Rb - one of the lowest in the periodic table - negatively charges the Si atoms. In turn, by looking at

Figure 2.1, we see that a translation of the optical spectra towards lower values leads to an increase in the refractive index of Si (red solid line) at the EUV energy of 91.8 eV. Therefore, the optical contrast between Rb_nSi_m and Mo becomes slightly higher than what predicted by Equation 2.1, thereby contributing to a raise in reflectivity.

The absorption coefficient of Si (blue solid line in Figure 2.1), on the other hand, stays practically unchanged, provided that the chemical shift is not large enough that the adsorption edge at 100 eV enters into the EUV reflectivity window of the MLM (depicted in gray in Figure 2.1).

The precise magnitude of the chemical shift in Si depends on the spatial arrangement of the atoms and the nature of the chemical bonds within the silicide. Qualitatively, the shift of the absorption edge is proportional to the effective charge of the absorbing ions, following Suchet's empirical rule [55]. Using this rule, we can calculate for Si a chemical shift of approximately -1.0 eV (see *Appendix A* for further details on the calculations).

We note that Suchet's rule does not take into account the detailed bonding characteristics or the crystal structure of the compound [55], which might influence the chemical shift, as for the case of rubidium silicide in the Zintl phase. Here, the Si atoms - forming Si_4^{-4} tetrahedral clusters - have an electric charge of -4 on 4 closely packed Si atoms. Thus, the negative electric field and, accordingly, the effective negative charge contributing to the chemical shift, are expected to increase. For an accurate determination of the shift in energy induced by this effect, X-ray absorption measurements would be necessary, as the precise atomic geometry of a freshly deposited Rb_nSi_m film is not known. However, we predict that the refractive index of Si, and thus, the EUV reflectivity, would increase even further.

In the case of Rb, we do not have sufficient information to calculate the chemical shift. However, its sign is expected to be positive and to have a negligible effect on the scattering factors of Rb in the silicide, as they are nearly constant around 13.5 nm.

To estimate the effect of the chemical shift of Si on the reflectivity of Mo/Rb_nSi_m MLMs, we recalculated the theoretical reflectivity substituting

the original Si optical constants with those shifted by -1.0 eV. For Mo/RbSi MLMs, for example, this correction leads to an increase in *Peak1*, *NrInt1*, and *NrInt10* of 0.02%, 0.27%, and 0.58%, respectively.

Since the chemical shift has a modest impact on the MLM reflectivity with respect to other factors (such as suppression of intermixing or density variations), we will neglect it in the following analysis. However, our results suggest that the addition of Rb and the special arrangement of Si atoms in the Zintl phase can potentially result in a noticeable increase in reflectivity, via the chemical shift of the electronic states of the Si atoms.

2.2.2 Intermixing with molybdenum

It is known that the measured reflectivities of EUV MLMs are lower than the theoretical values and that they decrease over time and with increased operation temperature. This is due to the evolution of the interfaces in the multilayer stack: sharp, non-equilibrium interfaces tend to lower their free energy by becoming intermixed and roughened through diffusion and compound formation. This process is driven by thermodynamics and mostly by the (negative) change in free energy $\Delta G_r = \Delta H_r - T\Delta S_r$ due to compound formation. Here, ΔH_r and ΔS_r are the reaction enthalpy and entropy, respectively. Since in solid-state reactions, entropy changes are often orders of magnitude smaller than enthalpy changes [56], we will neglect ΔS_r. We therefore approximate the free energy change due to the formation of a compound as $\Delta G_r \sim \Delta H_r$. When the MLM is not protected by diffusion barriers, compound formation will continue, in principle, until the entire stack is turned into a single, homogeneous mixture. In practice, the mixed interfaces have widths of several atomic layers to several nanometers.

For completeness, we should mention that there is an additional thermodynamic driving force for interface mixing, deriving from the reduction of the interfacial free energy. This effect has a short-range character and would, by itself, lead to interface widths in the order of one or just a few atomic layers [57]. As this interface-energy effect is bound to be modest compared to the enthalpy effect, we leave it out of our analysis.

Next to thermodynamics, also kinetics plays an essential role in determining the rate of intermixing. For a lack of detailed information, we simply assume here that we should not expect essential differences in diffusion coefficients between the materials that we address. Instead, we base our predictions of the interface widths in Mo/Rb_nSi_m MLMs fully on the differences in the enthalpies of compound formation.

In agreement with the above considerations, it has been shown experimentally that the roughness in Mo/Si MLMs is mainly caused by silicide formation [58],[59]. The three possible molybdenum silicide phases are Mo_3Si, Mo_5Si_3 and $MoSi_2$ [60].

For the case of Mo/Rb_nSi_m MLMs, interdiffusion and compound formation between Rb and Mo can be excluded, as they are mutually insoluble at room temperature and do not form any intermetallic phase [61]. Therefore, similarly to Mo/Si MLMs, also for Mo/Rb_nSi_m MLMs, molybdenum silicides are the main product of intermixing.

Using the reaction equations shown in *Appendix B*, we calculated the enthalpies of formation for one mole of atoms for each molybdenum silicide phase (see Table 2.3). In this calculation, the Si is recruited either from the pure Si layers in an Mo/Si MLM, or from an Mo/RbSi MLM.

Table 2.3 Formation enthalpies of three Mo_nSi_m compounds in Mo/Si MLMs (second column) and Mo/RbSi MLMs (third column).

Compound	ΔH_r[kJ] in Mo/Si MLMs	ΔH_r[kJ] in Mo/RbSi MLMs
Mo_3Si	-30.5 ± 1.5	-5.6 ± 2.3
Mo_5Si_3	-39.2 ± 1.5	-2.8 ± 2.5
$MoSi_2$	-45.3 ± 1.5	+10.6 ± 3.0

Table 2.3 shows that for Mo/RbnSim MLMs, where the Si atoms have already reacted with the Rb atoms, the thermodynamic driving force for the formation of Mo_nSi_m is significantly decreased, by 82% for Mo_3Si and

92% for Mo_5Si_3. The enthalpy of formation of $MoSi_2$ even turns positive, which corresponds to full, thermodynamic protection against the formation of that silicide in Mo/RbSi MLMs.

As Rb in the silicide phase is in the +1 oxidation state, the higher the Rb content the more positive is the enthalpy of the Mo_nSi_m formation. Therefore, in the sequence, RbSi (50.0 at.% Rb), $Rb_{12}Si_{17}$ (41.4 at.% Rb) and Rb_6Si_{46} (11.5 at.% Rb), the first will provide better protection against the formation of Mo_nSi_m. For this reason, in the following discussion we will focus only on Mo/RbSi. We note, however, that since Mo/Rb12Si17 gives a higher theoretical reflectivity (see Table 2.2) the optimum rubidium silicide composition in practice might not be RbSi.

The suppression of Mo_nSi_m formation in Mo/RbSi multilayer mirrors should lead to sharper interfaces and therefore to an EUV reflectivity closer to the theoretical value. In order to quantify the expected reflectivity, we now proceed to associate the calculated enthalpies with expectations for the interface thickness.

We begin by calculating the interface width in Mo/Si MLMs. The theoretical reflectivity matches the maximum experimental value for such mirrors of 69.5% when we introduce in our numerical model an interface width of $\sigma = 0.71\,\mathrm{nm}$. This value for σ is comparable to the thickness of intermixed regions observed with TEM [62],[63].

To predict the reduction in intermixing in Mo/RbSi MLMs, we use the approximation that the reduction in the width of the intermixed region in Mo/RbSi MLMs scales proportionally to the suppression of the Mo_nSi_m formation. We note that this method actually underestimates the reduction of the interface width. It would be more realistic to expect changes in the activation energy for interdiffusion to scale linearly with changes in the enthalpy for compound formation. As the activation energy appears in the exponential factor that governs the interdiffusion rate, a super-linear effect should be expected on the interface width. A second conservative estimate is introduced by our choice in the remainder of this article to concentrate on the weakest reduction in the enthalpy for compound formation, namely that of 82% with respect to Mo3Si (see Table 2.3).

In addition to the enthalpy-driven intermixing, we also take into account the contributions to the width of all interfaces deriving from the initial roughness of the substrate and from the kinetics of the deposition process. AFM experiments have shown that the roughness levels of the individual layers in the MLM can be lowered down to 0.1 nm rms by ion polishing [14]. As a conservative estimate, in our calculations we added a roughness of 0.2 nm to all interfaces, including the substrate surface and the surface of the top layer. We thus estimate that a suppression of intermixing of 82% leads to an interface width in Mo/Rb_nSi_m of $\sigma \sim 0.71$ - (0.71 - 0.20) $\times$ 82% nm = 0.29 nm.

In Table 2.4 we report the values for the reflectivity for a Mo/RbSi MLM, calculated including $\sigma = 0.29$ nm (second line) to the ideal multilayer structure. We also explored the result for the case that the suppression of intermixing were a factor 2 more modest (only 41% suppression of the intermixing in Mo/RbSi compared to Mo/Si), corresponding to $\sigma = 0.5$ nm (third line).

2.3 Results and discussion

Table 2.4 summarizes our estimates for the interface width in Mo/RbSi MLMs and the corresponding values of the EUV reflectivity. As before, we optimized the periodicity d and the bilayer thickness ratio Γ in order to reach the highest possible peak reflectivity *Peak1*. For all cases, the number of MLM periods was $N = 100$ and the interface widths of the substrate and top surfaces were set to $\sigma = 0.2$ nm. For all other interfaces we used $\sigma =$ 0.29 nm (or $\sigma = 0.5$ nm, assuming half the suppression of intermixing).

We also include the normalized integral reflectivities for a single mirror *NrInt1* and for a series of ten mirrors, *NrInt10*. For reference, we show the corresponding numbers for a Mo/Si MLM [14] (first line in Table 2.4) and for the type of mirror currently employed in EUV lithography machines, i.e. a Mo/Si MLM with B_4C diffusion barriers [32]. For these two reference systems, we used the experimental values of the peak reflectivity to fit the interface width and subsequently calculated the other MLM properties.

As previously mentioned, the theoretical reflectivity matches the experimental value in Mo/Si MLMs when we set σ to 0.71 nm for all Mo-

Si interfaces. For Mo/Si MLMs with 0.30 nm thick B_4C interlayers, separating the Mo layers from the Si layers, we have to assume an effective $\sigma = 0.57$ nm for all B_4C-mediated Mo/Si interfaces, in order to match the experimentally reported reflectivity.

Table 2.4 Calculated maximum achievable reflectivities for Mo/Si, Mo/RbSi and Mo/Si/B_4C MLMs, at 13.5 nm and normal incidence. The choices for the interface width σ are discussed in the text. The columns Peak1, NrInt1 and NrInt10 indicate respectively the peak reflectivity of a single MLM, and the normalized integrated reflectivities of a single MLM and a combination of 10 MLMs in series [42]. See Appendix A for the complete reflectivity profiles.

	MLM parameters					Reflectivity [%]		
Mo/	Inter-layer	σ [nm]	ρ [g cm^{-3}]	d [nm]	Γ	Peak1	NrInt1	NrInt10
Si	None	0.71	2.33	6.92	0.38	69.5 [14]	100	100
RbSi	None	0.29	2.72 [44]	6.92	0.36	73.9	112.1	200.9
RbSi	None	0.50	2.72 [44]	6.92	0.36	71.9	102.6	141.3
Si	B_4C [0.3 nm]	0.57	2.33	6.92	0.35	70.15 [32]	110.0	128.6

From Table 2.4, we find that the reflectivity performance expected for Rb-based mirrors is far superior to that of Mo/Si MLMs and that of Mo/Si MLMs integrated with B_4C barrier layers, even if we assume the more modest suppression of the intermixing, corresponding to $\sigma = 0.50$ nm.

We recognize that the *NrInt1*-values reflect not only the changes in the peak reflectivity, but also in the width of the reflectivity spectrum. On the other hand, the *NrInt10*-values vary much more strongly with the peak reflectivity because this effect is factored in 10 times. Comparing the

normalized, integrated reflectivities of 10 mirrors in series (*NrInt10*), we see that the Mo/RbSi MLMs with the sharpest interfaces can in principle reach a reflectivity that is 56% higher (200.9% instead of 128.6%) than Mo/Si MLMs integrated with B_4C diffusion barriers.

Regarding the feasibility of implementation of these mirrors in EUV lithography technology, some additional considerations are relevant. First of all, Rb-based mirrors should be operated well below their decomposition temperatures. In current EUVL optics, the mirror closest to the EUV light source – the collector mirror – reaches temperatures of 700-800 °C during operation; the other MLMs - constituting the illuminator and projection optical stages - are subjected to progressively lower temperatures. As previously stated, the decomposition temperature of RbSi is 1000 °C [50], which would therefore not restrict its application for EUVL. However, as the EUV source power continues to be raised, the collector mirror temperature may become a future point of concern in this respect.

Another important factor is that in current EUVL machines with sources of EUV light based on laser-produced tin plasma, the MLMs are operated in a hydrogen-rich environment, with a H_2 partial pressure in the order of 5 Pa. The hydrogen serves to mitigate the effect of tin in these machines and avoid and/or counteract contamination by tin of the EUV optics. In combination with the intense EUV light, this puts the MLMs in contact not only with H_2 gas, but also with H^+ ions and H radicals, which are known to lead to degradation (e.g. blistering [64]) of Mo/Si MLMs. While a Mo/RbSi MLM would be stable under vacuum conditions, in a hydrogen environment, RbSi may absorb hydrogen and eventually even form RbH and $RbSiH_3$. This could potentially lead to a significant volume expansion and increase of the EUV wavelength at which the reflectivity of the MLM peaks, which should be regarded as a form of degradation of this type of MLM. Rb-based MLMs should therefore have to be adequately protected from hydrogen incorporation with suitable capping layers. It has been already shown however that implanting the Si layer with low energy (150 eV) hydrogen ions leads to a significant reflectivity enhancement in Mo/Si MLMs [65]. Multilayer mirrors based on hydrogenated rubidium or hydrogenated rubidium silicide, if appropriately designed for reflecting 13.5 nm light may therefore constitute a potential route for enhancing the MLM reflectivity even further.

In the context of the experimental realization of the proposed MLM structures, we have not found information in the literature about the deposition of Rb compounds. We expect that it should be possible to use techniques such as sputter-deposition and pulsed-laser-deposition for this purpose, which are both applied for the deposition of complex compound materials. In addition to deposition experiments, aiming to implement the proposed Mo/RbSi multilayer structure, measurements need to be carried out to verify the predicted EUV-reflectivity properties and to verify the predicted stability of the structure at elevated temperatures.

2.4 Conclusion

In the search for new ways to improve the reflectivity and stability of Mo/Si-type multilayer EUV mirrors, we explored new multilayer structures, consisting of bilayers of molybdenum and silicon-based compounds. We aimed for material combinations with high optical contrast and minimal absorption around 13.5 nm, and with a minimal thermodynamic driving force for intermixing at the interfaces. Our numerical calculations have shown that, among the various considered material combinations, Mo/Rb_mSi_n provides the highest theoretical reflectivity in the spectral regime 12.5-14.5 nm. The favorable optical properties of Rb, the chemical shift in Si induced by the formation of a compound with Rb, and the thermodynamic suppression of intermixing at the Mo/Rb_mSi_n interfaces are all argued to contribute to enhancements in reflectivity and stability of these MLMs, with a calculated reflectivity exceeding by more than 2% that of the current best Mo/Si MLMs, integrated with diffusion barriers. This result is expected to increase the EUV throughput of a 10-mirror system by more than 50% [66]. We believe that this research represents a new approach for the design and optimization of EUV multilayer mirrors, which may be relevant for future generations of projection lithography tools.

3

Ruthenium nanolayers under heat – the influence of the sputtering pressure on the thermal stability

In this chapter we investigate the effect of the sputtering pressure on the structure and thermal stability of ultrathin Ru films. The films were deposited on a silicon substrate, using low Ar pressure (2.7×10^{-3} mbar), high (2.7×10^{-2} mbar), and a combination of the two in subsequent stages of the deposition, namely high for the first stage and low for the second. The films were annealed in vacuum at temperatures ranging from 250 to 800 °C and characterized by AFM, SEM and XPS. From the analysis of the height-difference correlation function on the AFM data, we obtained the evolution of the morphological properties, such as grain size and roughness, as a function of temperature. The films deposited at low pressure, characterized by a dense and uniform initial structure, show strong grain growth and coarsening, starting already at 500 °C. In contrast, the films deposited at high pressure and the bilayer, characterized by a rougher intial morphology, remain remarkably stable up to 600 °C. We attribute this result mainly to the different initial grain boundary configuration, and we discuss the possible surface-energy minimization processes driving the evolution.

3.1 Introduction

Ultrathin ruthenium (Ru) films are interesting for a wide spectrum of applications, spanning EUV mirrors and pellicles [67],[68], catalysis [69] and microelectronics [70]. For these applications, the stability of nanolayers is a basic requirement, inherently difficult to guarantee due to the extreme surface-to-thickness ratio of these structures, as discussed in Chapter 1. In this respect, the choice of the fabrication method is extremely important, as it influences the structural and mechanical properties of the films, such as morphology, adhesion and stress, which, in turn, affect their thermodynamic stability.

Among the available techniques for depositing Ru (e.g., electron-beam evaporation [71], atomic layer deposition (ALD) [72] and pulsed laser deposition [73]), magnetron sputtering [74] is often the process of choice, owing to the ease of the deposition and the multiple parameters that can be tuned to achieve various desired film properties. For example, the working gas pressure can be varied to change the angular distribution and the energy of the sputtered particles, resulting in films with different structures and intrinsic stress [75],[76].

In this chapter, we investigate the effect of the sputtering pressure on the initial structure and thermal stability of Ru nanolayers. We deposited ~ 6 nm-thick Ru films on a silicon substrate, using three different Ar pressures: low (2.7×10^{-3} mbar), high (2.7×10^{-2} mbar) and a combination of the two (2.7×10^{-2} mbar followed by 2.7×10^{-3} mbar). We annealled the three Ru series in vacuum at temperatures in the range 250-800 °C. We report on the evolution of the morphology as a function of temperature by means of AFM, SEM and XPS measurements, and we discuss the main mechanisms driving the evolution.

3.2 Methods

Ultrathin Ru films were deposited on a Si(100) substrate with a native oxide layer by DC magnetron sputtering, at room temperature. Three series of films were obtained by changing the working gas pressure conditions (see below). Each series was divided into five samples that were annealed

in vacuum for 30 minutes at 250, 500, 600, 700 and 800 °C, respectively. In the following, we describe in detail the fabrication methods and characterization techniques, as well as the statistical model used for the analyisis of the film morphology (Section 3.2.1).

Sample preparation. Ru was deposited on Si(100) substrates using a magnetron sputtering system (Polyteknik Flextura M506 S). The substrates were cleaned using a standard procedure: 10 minutes of ultrasonic cleaning in acetone, flushing in isopropanol and drying with pressurized nitrogen. They were then inserted in the deposition chamber, which was pumped down to a background pressure of 1×10^{-8} mbar. The distance between the target and the substrate was 18 cm. The Ru target (99.99%, AmericanFellow, USA) was pre-sputtered for 500 s before opening the shutter for the actual deposition.

Following the recipes provided by [77], we prepared three series of Ru films using three different working gas (Ar, 99.99%) pressures during deposition, while keeping the power fixed at 200 W. One series was deposited at low pressure (2.7×10^{-3} mbar), one at high (2.7×10^{-2} mbar), and one by dividing the deposition in two subsequent stages, namely high for the first stage and low for the second stage. In all three cases, the total deposition time was 10 s. The recipes are summarized in Table 3.1. Throughout this chapter, we will refer to these three series of films as $Ru_{(l)}$, $Ru_{(h)}$ and $Ru_{(h\text{-}l)}$.

Table 3.1 Average nominal thicknesses of Ru films deposited at low (2.7×10^{-3} mbar), dual (2.7×10^{-2} mbar followed by 2.7×10^{-3} mbar) and high (2.7×10^{-2} mbar) Ar pressures. The error margin on the thickness value corresponds to the standard error of the mean.

Film	Deposition conditions			Thickness (nm)
	Power (W)	Ar pressure (mbar)	Time (s)	
$Ru_{(l)}$	200	2.7×10^{-3}	10	5.4 ± 0.2
$Ru_{(h\text{-}l)}$	200	2.7×10^{-2} 2.7×10^{-3}	6 4	6.8 ± 0.1
$Ru_{(h)}$	200	2.7×10^{-2}	10	6.9 ± 0.2

The thickness of the films was measured by scanning with a profilometer (KLA Tencor P7) over the edge of an open region of the film. The open region was obtained by drawing a ~ 5 mm^2-spot at the center of the Si substrate using a permanent marker, which served as a "resist" layer to lift-off the portion of film deposited on top. The best vertical and horizontal profilometer-resolutions were 0.4 nm and 25 nm, respectively. The nominal thicknesses of the films were obtained by averaging over 5 different profile scans. Average values and standard errors are reported in Table 3.1.

Annealing. The three series of $Ru_{(l)}$, $Ru_{(h)}$ and $Ru_{(h\text{-}l)}$ were divided in five samples. Each sample was annealed in a home-built vacuum furnace pumped down to a base pressure of ~ 5.5×10^{-7} mbar. We used cycles of 30 minutes at the temperatures 250, 500, 600, 700 and 800 °C. During sample insertion from the loadlock to the pre-heated main chamber, the temperature remained constant and the background pressure increased to ~ 1×10^{-5} mbar, which restored within ~ 300 s. The samples were cooled by natural convection when we admitted air into the loading chamber right after the completion of the heating cycle.

Sample characterization by Scanning Electron Microscopy (SEM) and Atomic Force Microscopy (AFM). Images of the Ru films before and after annealing were acquired using a FEI Verios 460 scanning electron microscope (SEM) at 5 kV in secondary electron (SE) mode, using a high-efficiency in-lens detector.

Topography measurements were carried out on a Bruker Multimode 8 AFM setup operating in ScanAsyst™ mode [78]. The probes were standard ScanAsyst-air silicon nitride cantilevers with triangular geometry, and a nominal tip radius of 2 nm (for more details, see [79]). Images were typically acquired with a resolution of 512 × 512 pixels and a scan size of 1000 nm, unless stated otherwise. So as to improve the statistical analysis, we acquired three AFM images per sample, on different regions.

Data processing in Python. We used Jupyter Notebook running Python 3.7.1 to process the data from our SEM and AFM measurements, plotting individual images and obtaining the parameters of interest from the calculation of the height-difference correlation function, described in the following section. The data analysis method is presented in Section B2 of the *Appendix*.

3.2.1 Height-difference correlation function analysis

When using probe microscopy techniques, such as AFM, the main types of information that one retrieves are the topography of the surface and the mechanical properties (elasticity and damping). Here, we concentrate fully on the topographical aspects, from which we derive detailed information on the statistics of the height variations. By analyzing the correlation in height variations between different points in the same scan line, we can characterize the topography of the surface in terms of roughness, grain size and short-range variations. We will use these three parameters to describe the morphologies of Ru films deposited at different working gas pressures, before and after heating.

The local height $h(\boldsymbol{x})$ measured by a tip scanning over a surface describes the height difference between the surface at an in-plane position $\boldsymbol{x}$ and a plane of reference. The reference plane can be defined arbitrarily, but it is convenient to choose it such that any tilt or curvature is removed, and the mean surface height $\overline{h} = \langle h(\boldsymbol{x}) \rangle$ is equal to zero.

As practical films are not perfectly flat, most local heights deviate from the mean value, i.e. most $h(\boldsymbol{x})$-values are non-zero. In other words, films are typically rough on a microscopic scale. The height variation or interface width w is generally used to describe the root-mean-square (rms) surface roughness:

$$w \equiv \sqrt{\langle \left(h(\boldsymbol{x}) - \overline{h}\right)^2 \rangle} = \sqrt{\langle h(\boldsymbol{x})^2 \rangle} \tag{3.1}$$

It is useful to quantify the correlation in height of different points over the surface, as this gives an indication of the typical length-scale at which the height varies. To extract this information we define the autocorrelation function $C_A(\mathbf{r})$:

$$C_A(\boldsymbol{r}) \equiv \langle h(\boldsymbol{x}) h(\boldsymbol{x} + \boldsymbol{r}) \rangle \tag{3.2}$$

Here, the vector $\boldsymbol{r}$ indicates the lateral displacement between points where the heights are compared and the angular brackets indicate spatial averaging over the position vector $\boldsymbol{x}$. At a distance $r \equiv |\boldsymbol{r}| = 0$, the

correlation will be maximum and from Equation 1 we obtain $C_A(0) = w^2$. From there on, the correlation decreases. The value of r above which the surface heights are no longer correlated, is known as the lateral correlation length ξ. For $r \gg \xi$, the autocorrelation fuction asymptotically reduces to $C_A(\boldsymbol{r}) = \langle h(\boldsymbol{x})\rangle\langle h(\boldsymbol{x}+\boldsymbol{r})\rangle = 0$.

Closely related to the autocorrelation function, and in fact equivalent, is the height-difference correlation function $\mathbf{C_H(r)}$:

$$\begin{aligned} C_H(\boldsymbol{r}) &\equiv \langle \big(h(\boldsymbol{x}) - h(\boldsymbol{x}+\boldsymbol{r})\big)^2 \rangle \\ &= \langle h(\boldsymbol{x})^2\rangle + \langle h(\boldsymbol{x}+\boldsymbol{r})^2\rangle - 2\langle h(\boldsymbol{x})h(\boldsymbol{x}+\boldsymbol{r})\rangle \\ &= 2(w^2 - C_A) \end{aligned} \tag{3.3}$$

From the behavior of $\mathbf{C_H(r)}$, one can extract three quantities of interest: the correlation length ξ, the roughness w, and the short-range uniformity H. The value of $\mathbf{C_H(r)}$ is characterized by two regimes [80],[81]:

$$\begin{aligned} C_H(r) &\propto r^{2H} && \textit{for } r < \xi\,, \\ C_H(r) &= 2w^2 && \textit{for } r \gg \xi \end{aligned} \tag{3.4}$$

H is the so-called Hurst exponent, and can have values in the interval $0 < H \leq 1$. The Hurst exponent is a parameter that indicates how height variations develop over short distances, up to the correlation length. Since the correlation length defines a window of distances equal or smaller than the characteristic grain size, in essence, H provides information on how rough are the surfaces of individual grains.

As a rule of thumb, for a critical value of $H = 0.5$ (i.e., $C_H(r) \propto r$ in Equation 3.4), the height profile follows a perfectly randow walk, meaning that after an upward fluctuation in the height, the surface has no preference to either continue in that direction or to return to the original level.

If $H < 0.5$, the height variations are anti-correlated. An upward fluctuation tends to be followed by a downward one, resulting in a 'jagged' surface profile. On the other hand, a value of H greater than 0.5 indicates a persistence in fluctuations; that is, an upward fluctuation will be more likely followed by another upward one. The closer H is to unity, the

stronger is the correlation. In this case, the surface is said to acquire a fractal, or self-similar, character.

As shown in Equation 3.4, at small distances, i.e. $r < \xi$, the function obeys a power-law scaling, while it quickly saturates at an average value of $2w^2$, for distances larger than the correlation length. The rms-roughness w follows directly.

Figure 3.1 shows a typical double-logarithmic plot of $C_H(r)$ as a function of the displacement r. The local roughness exponent H can be directly determined from a fit of the linear increase of $\log\big(C_H(r)\big)$ with $\log(r)$. The correlation length ξ can be either derived mathematically (ξ being equal to the distance at which $C_A(\xi) = w^2/e$ and thus $C_H(\xi) = 2w^2(1 - e^{-1})$) or geometrically, by taking ξ as the crossing point between the linear fit to the initial section in the double logarithmic plot and the horizontal asymptote, $2w^2$, as indicated by the orange dot in Figure 3.1 [82],[83]. In this thesis we have adopted the latter method.

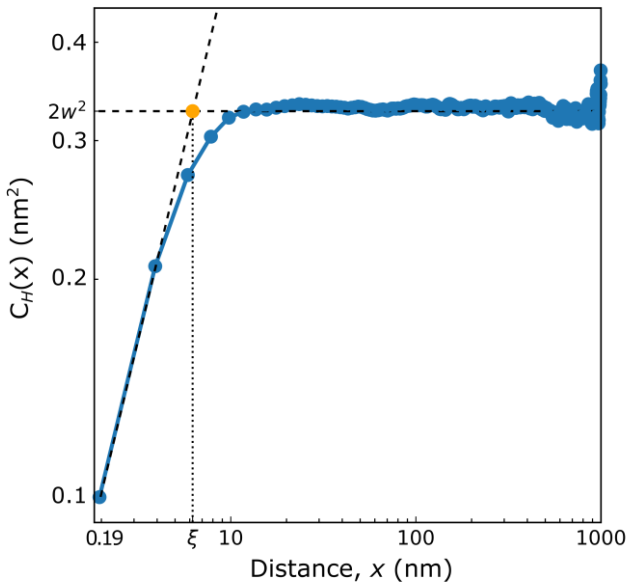

Figure 3.1 Height-difference correlation function of as-deposited Ru. The dashed lines represent the fits to the asymptotic and power law regions, respectively, used to extract the rms-roughness, w, the correlation length, ξ, and the Hurst exponent, H.

3.3 Results

Using the characterization techniques and analytical methods described above, we report on the evolution with temperature of ultrathin Ru films, deposited at different sputtering pressures. The SEM images of the as-deposited and annealed Ru series are shown in Section 3.3.1 and 3.3.2, respectively. In Section 3.3.3, the AFM images and the results of the average grain size, rms-roughness and short-range uniformity as a function of temperature are presented.

3.3.1 Ru nanolayers grown at different sputtering pressures

Figure 3.2 shows the SEM images of the three series of Ru films, each with a nominal thickness of approximately 6 nm, grown at low, dual (high followed by low) and high Ar pressures (see Table 3.1).

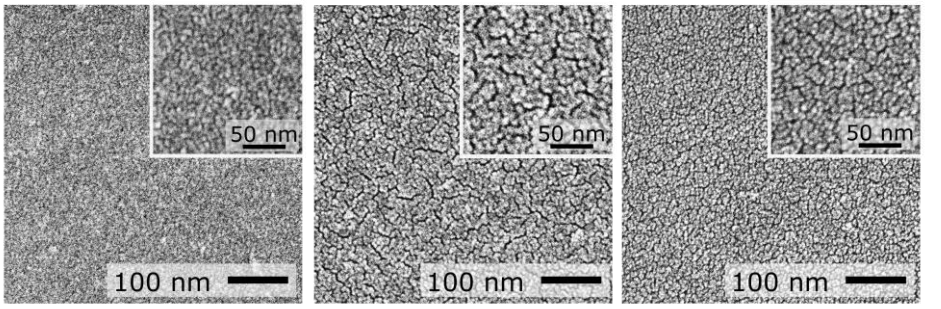

Figure 3.2 SEM images in secondary-electron (SE) mode of ~ 6 nm-thick Ru films, sputter-deposited at low (left), dual (middle) and high (right) Ar gas pressures, respectively.

The different sputtering pressures lead to films with distinct morphologies. Low-pressure deposition (left panel of Figure 3.2) leads to a dense and relatively uniform $Ru_{(l)}$ film, characterized by a fine texture with small grains of ~ 5 nm in diameter. Even though a similar fine structure is present for $Ru_{(h\text{-}l)}$ (middle panel of Figure 3.2) and $Ru_{(h)}$ (right panel of Figure 3.2), resulting from dual- and high-pressure deposition respectively, the SEM images reveal an additional, larger-scale structure that looks more open and rough. The fine grains appear in fact to be organized in larger clusters

surrounded by deep valleys*. In separate XPS measurements on the as-deposited samples (see Section B3. Elemental characterization by X-ray Photo-emission Spectroscopy (XPS) of Ru films before and after heating. of *Appendix B*) no clear Si peak is detected, suggesting that all three types of Ru films are closed. We therefore argue that the valleys in $Ru_{(h\text{-}l)}$ and $Ru_{(h)}$ represent deep grain boundary grooves, where the film is significantly thinner and yet does not expose the substrate.

3.3.2 Evolution with temperature

Figure 3.3 shows the evolution of $Ru_{(l)}$ (left), $Ru_{(h\text{-}l)}$ (center) and $Ru_{(h)}$ (right) as a function of temperature. After annealing at 250 °C, all three films present a morphology very similar to the as-deposited one (compare the first row of Figure 3.3 with Figure 3.2).

At 500 °C, the structure of $Ru_{(h\text{-}l)}$ and $Ru_{(h)}$ remains largely preserved, while we observe substantial changes in $Ru_{(l)}$. The initial finely-structured and uniform morphology of Figure 3.3*A* evolves into the much more heterogeneous surface of Figure 3.3*D*. In $Ru_{(h\text{-}l)}$ (Figure 3.3*E*), the number of prominent grain boundaries reduces with respect to Figure 3.3*B*, accompanied by a modest darkening of the remaining grooves, indicating a slight coarsening. In addition, the interior of the clusters appears less strongly structured than before. In $Ru_{(h)}$ (Figure 3.3*F*), the morphology appears unchanged with respect to the previous stage (Figure 3.3*C*).

At 600 °C, we observe the reorganization of $Ru_{(l)}$ into larger structures that suggest that the film now consists of relatively large grains with well-developed grain boundary grooves (Figure 3.3*G*). The other two films (Figure 3.3*H* and *I*), show nearly the same situation as before: in $Ru_{(h\text{-}l)}$, we

* The valleys are represented by the black solid lines and are the result of a lower escape probability of the secondary electrons from those regions. The secondary electron yield (SEY) depends not only on the electronic properties of the constituent elements (Si having a higher work function than Ru, thus emitting less electrons) but also by the geometrical properties of the surface. For instance, at protrusions electrons are emitted more easily (so-called "edge effect") while at grooves electrons are partly trapped [149].

observe only a mild increase in contrast and width of the dark features; in $Ru_{(h)}$, hardly any change can be detected.

Annealing at 700 °C results in further coarsening of the grains in $Ru_{(l)}$, as illustrated by the increase in the average grain size and the more prominent character of the grain boundary grooves (Figure 3.3*L*). In $Ru_{(h\text{-}l)}$ and $Ru_{(h)}$ (Figure 3.3*M* and *N*), the grooving process has progressed to the stage where significant parts of the substrate become exposed. In addition, we observe the formation of bright agglomerates. In Figure B3 in *Appendix B* we provide a zoomed-in view of these structures.

Finally, at 800 °C, all films undergo drastic changes. The morphology of $Ru_{(l)}$ is characterized by large crystallites surrounded by marked grooves (see inset of Figure 3.3*O*). On a larger scale, the film is found to contain 'holes', roughly rectangular in shape (Figure 3.3*O*), oriented along the **[011]** and **[0$\bar{1}$1]** directions of the underlying Si(100) substrate. In the $Ru_{(h\text{-}l)}$ and $Ru_{(h)}$ films, the history of the previous structures is completely lost, and the films have transformed into three-dimensional clusters of irregular shapes, which appear to be locally connected. In $Ru_{(h\text{-}l)}$, relatively large, dark regions appear (Figure 3.3*P*). As shown in the inset, the dark regions exhibit a morphology that is very similar to the bright regions. The difference in contrast may indicate a different composition[†] or a different layer thickness, or possibly both. In $Ru_{(h)}$, the clusters are more compact in shape and the film seems less heterogeneous (Figure 3.3*Q*). On a larger scale, we observe dark regions with shapes and orientations that are somewhat reminiscent of the rectangular 'holes' in $Ru_{(l)}$ (Figure 3.3*O*).

In *Appendix B*, we summerize the results of the XPS survey on the samples annealed at 800 °C, which confirm the presence of Si (see Table B1). In Figure B4, we add SEM micrographs of Ru films annealed at 800 °C for double the amount of time (i.e., 1 hour), which indicate that in the extra time at that temperature, the characteristic shapes found in Figure 3.3*O, P* and Q have grown larger.

[†] A potential silicidation of the Ru layer in those regions may significantly decrease the emission of secondary electrons, and thus result in a lower SEY.

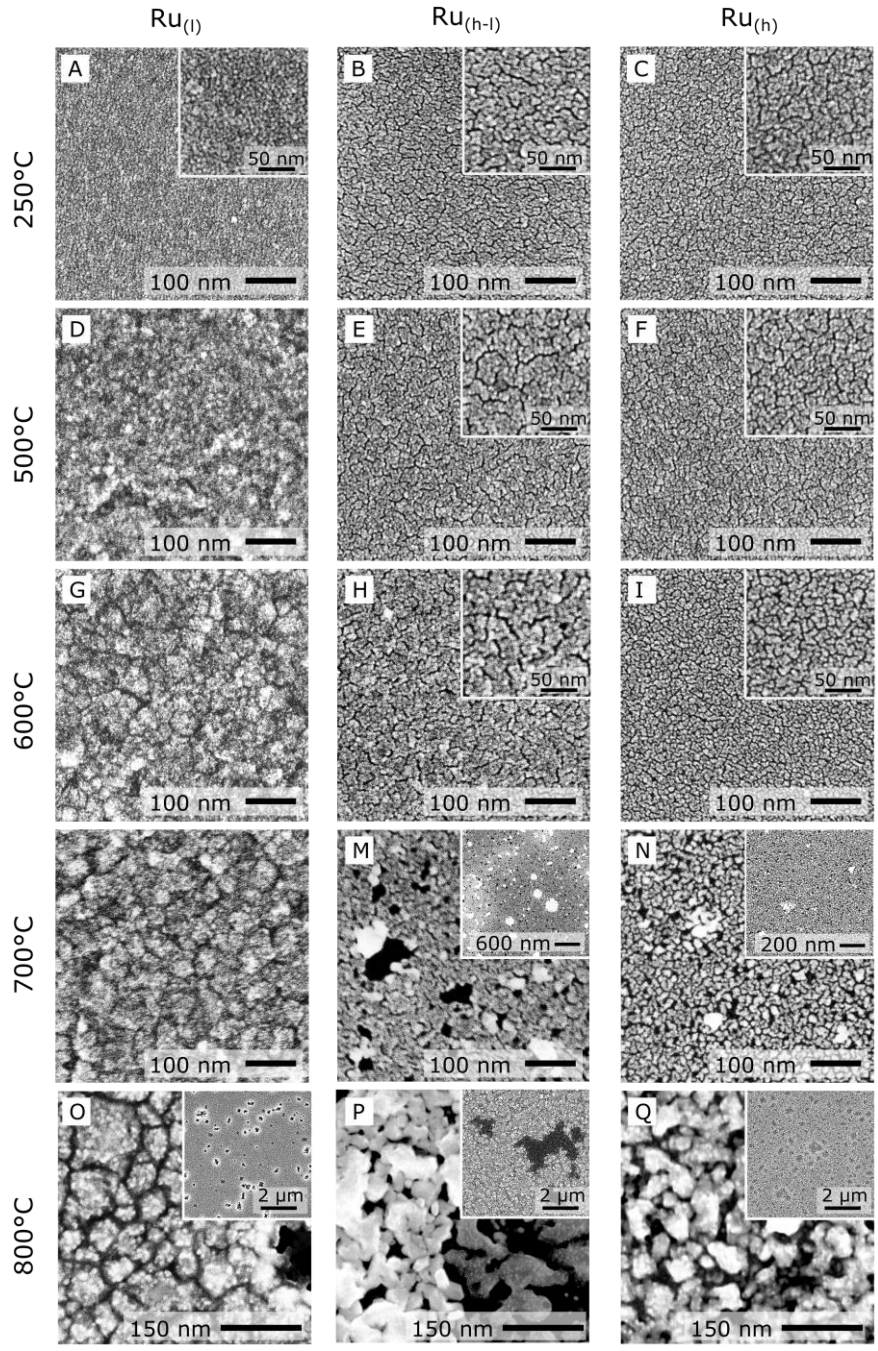

Figure 3.3. SEM micrographs of $Ru_{(l)}$, $Ru_{(h\text{-}l)}$ and $Ru_{(h)}$, after annealing.

3.3.3 Grain size, roughness and uniformity

Figure 3.5, 3.6 and 3.7 show a selection of AFM images representing the respectively $Ru_{(l)}$, $Ru_{(h\text{-}l)}$ and $Ru_{(h)}$, prior and after annealing (30 minutes at 250, 500, 600, 700 and 800 °C).

From the AFM data we obtained the height-difference correlation function, $C_H(r)$, over a range of lateral distances from 1.9 nm to 1 µm. We used the general 'recipe' provided in Section B2. AFM Data Analysis of *Appendix B,* in combination with further refinements to avoid artefacts.

The evolution of $C_H(r)$ as a function of temperature, shown in Figure B2, highlights the overall trends for the three Ru films, which turn out to be significantly different from each other. The difference is particularly strong for the increase in the asymptotic level (rms roughness) with annealing temperature, which is appreciable already at 500 °C in the case of $Ru_{(l)}$, while it remains low up to 700 °C in the other two cases.

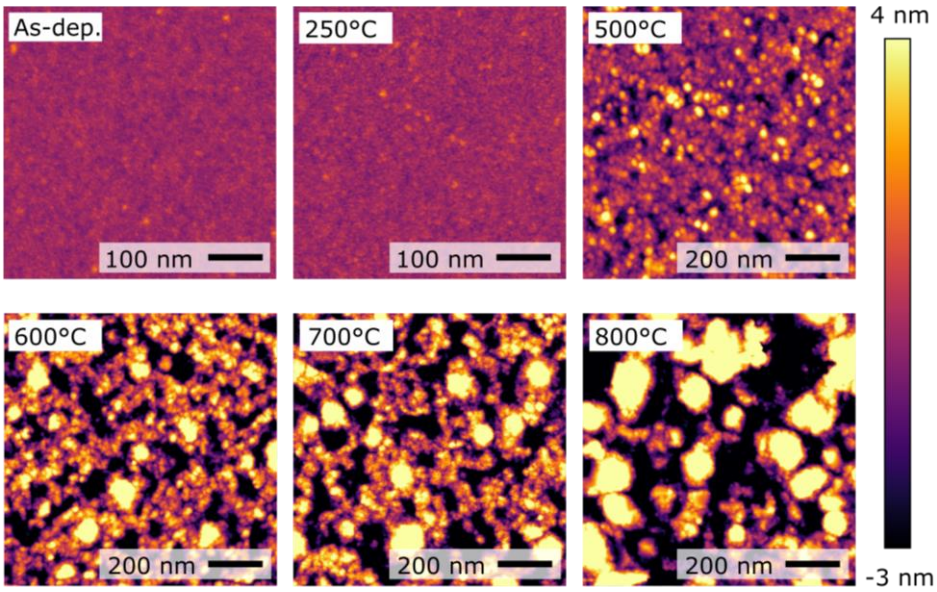

Figure 3.4 $Ru_{(l)}$. See below for description.

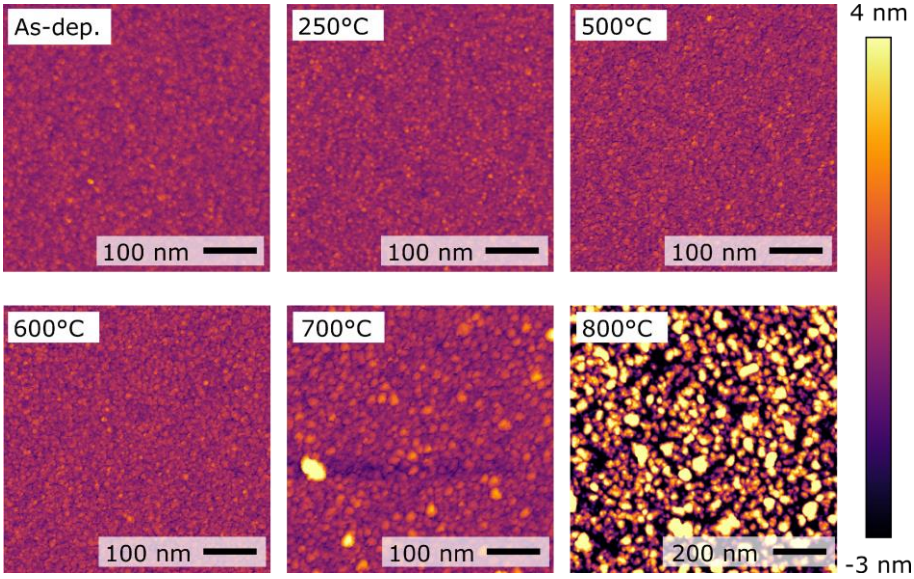

Figure 3.5 $Ru_{(h-l)}$. See below for description.

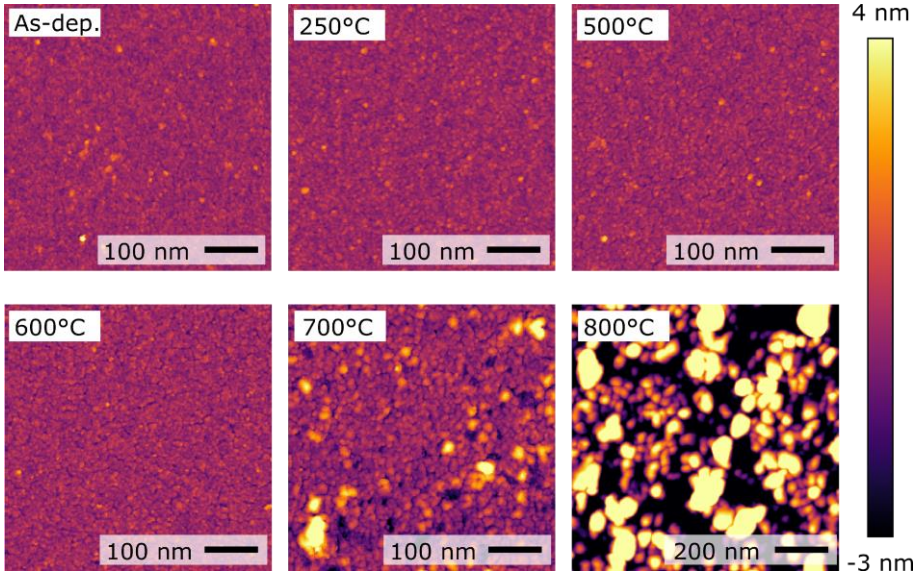

Figure 3.6 $Ru_{(h)}$. See below for description.

Figures 3.4-3.5-3.6 AFM images of as-deposited and annealed Ru films. The lateral length scales are indicated by the scale bars in the images. All images are displayed with the same color scale, to emphasize the evolution in height variations.

From the $C_H(r)$-plots, we extracted the average values of the rms roughness w, the correlation length ξ, and the Hurst exponent H, as a function of temperature, which are shown in Figure 3.7.

Before annealing, the average roughness w is low for all three Ru films deposited at the lowest pressure, namely $w_{(l)} = 0.29 \pm 0.03$ nm, $w_{(h-l)} = 0.35 \pm 0.01$ nm and $w_{(h)} = 0.37 \pm 0.01$ nm). The correlation length is the same for $Ru_{(l)}$ and $Ru_{(h)}$ within the error margin ($\xi_{(l)} = \xi_{(h)} = 6.4 \pm 0.3$ nm), while for $Ru_{(h-l)}$ it is lower ($\xi_{(h-l)} = 5.4 \pm 0.3$ nm). The values of the Hurst exponent lie slightly below 0.5 for all three films and overlap within the error margins.

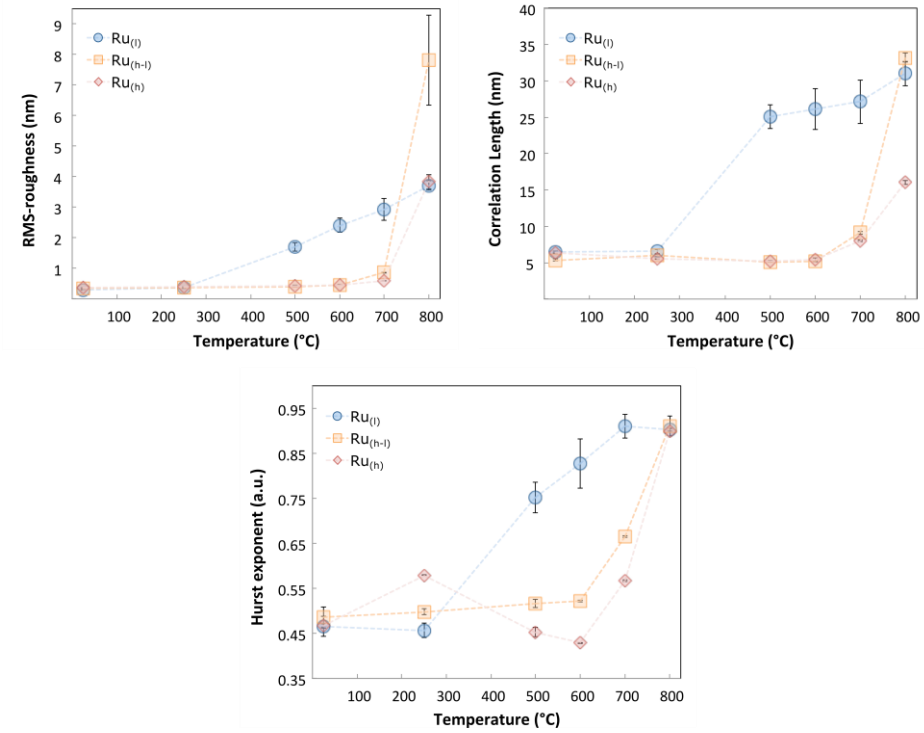

Figure 3.7 Average values of the rms roughness, correlation length and Hurst exponent, for $Ru_{(l)}$ (blue circles), $Ru_{(h-l)}$ (yellow squares) and $Ru_{(h)}$ (red rombs) as a function of temperature. Dashed lines are linear interpolations and only serve as guides to the eye. Error bars denote the standard error of the mean for each data point (see *Appendix B* for a detailed explanation of the image acquisition methods and data analysis).

At 250 °C, we observe no significant changes in surface roughness and correlation length with respect to the starting configuration, for all three films. Also the Hurst exponents of $Ru_{(l)}$ and $Ru_{(h\text{-}l)}$ remain relatively constant. On the other hand, the H-valule of $Ru_{(h)}$ goes above 0.5 at this temperature.

At higher annealing temperatures, we find that $Ru_{(l)}$ follows a drastically different evolution than $Ru_{(h\text{-}l)}$ and $Ru_{(h)}$. In $Ru_{(l)}$, at 500 °C, all parameters increase significantly, and they continue to rise roughly linearly up to 800 °C‡. At this final annealing temperature, the roughness reaches a value of of $w_{(l)} = 3.7 \pm 0.3$ nm, the correlation length of $\xi_{(l)} = 29 \pm 3$ nm, and the Hurst exponent of $H_{(l)} = 0.90 \pm 0.01$.

In contrast, $Ru_{(h\text{-}l)}$ and $Ru_{(h)}$, following a similar behavior to each other, show no significant variations in w and ξ up to 600 °C, and only a slight increase in both parameters at 700 °C. At 800 °C, both quantities increase significantly. The differences are largest for $Ru_{(h\text{-}l)}$, with w and ξ increasing roughly by factors of 10 and 4, to values of 8 ± 3 nm and 33 ± 3 nm, respectively; for $Ru_{(h)}$, w and ξ increase by factors of approximately 7 and 2, to 3.8 ± 0.5 nm and and 16.0 ± 0.5 nm, respectively. Similarly to $Ru_{(l)}$, for these two films the Hurst exponent reaches a maximum of 0.90 ± 0.04.

3.4 Discussion

The different morphologies of the three series of Ru films reflect the influence of the working gas pressure on film growth, as illustrated by the structural zone model for sputter-deposited films [18],[75]. The argon pressure strongly impacts the energy and angular distribution of the sputtered atoms, by affecting their mean free path. At high pressures, the target atoms undergo many collisions with the background gas, which leads to a high degree of thermalization and a spread of the angular distribution [75]. The low energies and shallow angles together contribute to strong self-shadowing and a columnar type of growth. On the other hand, when the working gas pressure is decreased, the sputtered atoms preserve much of

‡ The value of the w and $\xi$for the $Ru_{(l)}$ sample annealed at 800 ºC were obtained by excluding from the analysis the portion of the image containing the hole.

their initial direction - close to the surface normal - and kinetic energy. This energy can be enough to re-sputter atoms at the surface. As a result, a dense and uniform morphology forms.

These two scenarios respectively describe the growth of $Ru_{(h)}$ (Figure 3.2*C*) and $Ru_{(l)}$ (Figure 3.2*A*). At an Ar pressure of 2.7×10^{-2} mbar, the resulting $Ru_{(h)}$ morphology is characterized by grainy clusters separated by deep valleys (similar to what described in [84]) while at 2.7×10^{-3} mbar $Ru_{(l)}$ is dense and uniform. The film structure of $Ru_{(h\text{-}l)}$ (Figure 3.2*B*) may be regarded as a superposition of the other two: isolated clusters, formed during the initial, high-pressure deposition stage, are then exposed to energetic atoms that impinge almost perpendicularly on the surface to directly fill the bare regions of the Si substrate; their higher average momentum further adds to that filling, by knocking previously deposited atoms into the voids between the clusters. For a schematic drawing of our interpretation of the initial structure of the three as-deposited Ru films we refer to Figure 3.8 (dashed line).

From the analysis of the height correlation function on the AFM images, we find that the rms roughness w is the lowest for $Ru_{(l)}$, confirming the relatively dense and smooth morphology compared to $Ru_{(h\text{-}l)}$ and $Ru_{(h)}$, where shadowing effects and the absence of adtom-impact smoothening produce rougher surfaces. For all freshly deposited films we obtained values for the correlation length ξ of about 6 nm. This matches the dimension of the fine grains visible in the SEM images of Figure 3.2 and is in line with a Volmer-Weber-type growth of polycrystalline films, for which usually the average grain size is in the order of the film thickness [85]–[87]. The roughness exponent in all three films is $H \sim 0.47$. This value has been found for many films deposited by physical vapor deposition [88],[89]. In general, it represents a jagged surface profile [84],[90].

At this stage, it is important to note that, due to the finite sharpness of the probing tip, the topography images obtained with AFM can never be perfectly accurate. In our images, it appears in fact that the tip was not sharp enough to resolve the full depth of the steepest and narrowest grooves. As a result, the deeper grain boundaries in freshly deposited $Ru_{(h)}$ and $Ru_{(h\text{-}l)}$ that are clearly recognizable in the SEM images (Figure 3.2*A* and *B,* respectively), are much less pronounced in the AFM images. The

resulting height correlation function is then dominated by the shallower features, which in this case are the individual fine grains composing the clusters. Generally, due to this convolution effect of tip and surface, the true w and ξ are underestimated compared to their real values [91].

In light of these considerations, we will focus the rest of our discussion only on the relative values of the three physical parameters, w, ξ and H, refraining from commenting on the absolute ones.

The changes of w, ξ and H as a function of temperature shown in Figure 3.7 highlight important differences in the mechanisms governing the evolution of the three Ru films. As the evolution is driven by the minimization of surface free energy and as the surface geometries of the films are different, we expect the mechanisms of mass transport to be also different. The surface geometries are primarly characterized by their grain boundary configuration. Grain boundaries (GBs) are defects that are associated with an excess energy per unit area. An increase in temperature enables the system of grains and grain boundaries to reduce the total grain boundary cost by a combination of two effects: (1) grain reorientation and (2) grain boundary migration [92].

In the first process grains reorient themselves so as to minimize the free energies of their surface, of their interface with the substrate and of their interface with neighboring grains (i.e. the grain boundary energy, γ_{GB}). As a result of the decrease in the average γ_{GB}-value, the average equilbrium opening angle of the GB grooves increases, leading to a smoother surface. This is represented in Figure 3.8 by the evolution of θ_1 into θ_{eq}.

Through the second process, i.e. GB migration, the total GB energy is reduced simply by reducing the GB density (i.e., their area in a 3D picture, or their length in a 2D one, as in Figure 3.8). The decrease in density goes hand-in-hand with the growth of the average grain size and the corresponding reduction in the total number of grains, for which larger grains grow at the expenses of smaller ones. During GB migration, the grains are no longer optimized in orientation, i.e. the average free energy per unit area γ_{GB} does not change, and so does the equilibrium opening angle, θ_{eq}. This implies that an increase in the average grain diameter should be accompanied by a proportional in film roughness. This is represented in Figure 3.8 by the fact that the groove's dimensions (width

and depth) increase but their shape stays the same (compare solid lines with dashed lines).

As the growth and coarsening process continues, the deeper grooves may reach the substrate, at which point holes may form in the film. Whether or not holes form and grow larger depends on the relative surface free energies of the substrate and the film. A low relative value of the substrate's surface free energy will lead to dewetting, i.e. to a growth of holes, once they are formed. This is often the case for metals grown on Si, which have generally higher surface energies. Ultimately, the film breaks into isolated islands, at which point the dewetting is complete.

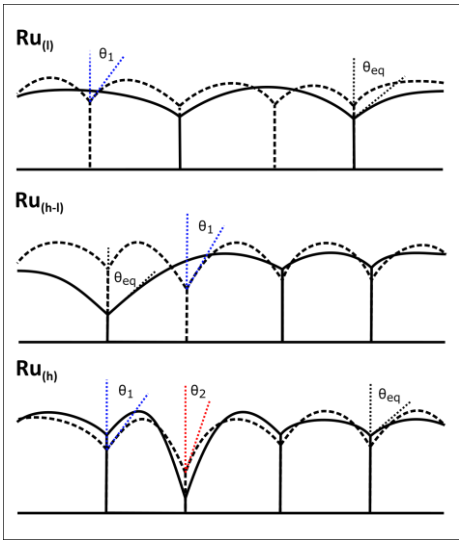

Figure 3.8 Schematic drawing of the proposed mechanisms for the evolution with temperature of the three Ru films deposited under different pressure conditions (see Table 1.1 for details about the recipe). The dashed and solid lines represent respectively the initial polycrystalline surface profile and the one after annealing at a temperature high enough to initiate surface diffusion yet low enough to prevent bulk diffusion.

Using the above considerations, we will provide our interpretation of the observed evolution of the three Ru films, schematically represented in Figure 3.8. For our discussion, we introduce the reduced temperature, T/T_m, where T is the absolute substrate temperature and $T_m = 2334$ °C is the melting point of Ru. This is important, as the evolution just described

only occurs when enough mobility is provided, i.e. when the substrate temperature is close enough to active surface or bulk diffusion.

At 250 °C ($T/T_m \sim 0.2$) we find that there is no considerable change in morphology for all three Ru films, indicating that surface diffusion and grain boundary mobility are still negligible.

Above 500 °C ($T/T_m \sim 0.3$), we observe that for $Ru_{(l)}$ all three parameters w, ξ and H, increase more or less linearly with annealing temperature, following the trend that is typical of grain growth and coarsening, as described above. Interestingly, the reduced temperature at which this process starts matches the value reported by Rost *et al.* for Au films, deposited by thermal evaporation [92]. In contrast with $Ru_{(l)}$, the other two films, $Ru_{(h\text{-}l)}$ and $Ru_{(h)}$, are remarkably more stable up to 700 °C ($T/T_m \sim 0.4$).

We propose that the difference in behavior as a function of temperature results from two main effects. First of all, as indicated before, the structure in $Ru_{(h\text{-}l)}$ and $Ru_{(h)}$ is organized in the form of clusters of grains (see Figure 3.2*B* and *C*). The shallow grooves between the grains within such a cluster indicate that these are separated by low-free-energy GBs (characterized by a larger opening angle, θ_1 in Figure 3.8). The deep grooves between the clusters are indicative instead of higher-energy GBs (characterized by a smaller opening angle, θ_2). If we describe the evolution of these films in terms of the competition between neighboring clusters, we recognize that their large in-plane radii of curvature make the driving, capillary force for cluster growth modest, thus requiring a high mobility, i.e. a high temperature to become effective. The second effect that adds to the slow evolution of $Ru_{(h\text{-}l)}$ and $Ru_{(h)}$ between 500 and 700 °C stems from the large depths of the grooves that separate the clusters. For these grooves and their accompanying GBs to move, much more atomic transport is required than for the motion of lower-energy GBs with shallow grooves, in the interior of the clusters. As a result, while the clusters increase their average radius of curvature and deepen the grooves between them, the interior of the clusters evolves towards even lower-free-energy GBs with even shallower internal grooves. With respect to the overall roughness, these two processes are competing, so that in the AFM images we do not detect a change in rms roughness. In this context, we repeat that the sensitivity

to the changes of the deeper and steeper grooves is limited due to the effect of tip convolution. In spite of the suppressed evolution of $Ru_{(h\text{-}l)}$ and $Ru_{(h)}$, at intermediate temperatures we observe the first signs of the formation of pits and a widening of the grooves for both films. At 700 °C, the edges of the GBs in the films retract further and the pits increase in size and density, exposing larger parts of the substrate.

At 800 °C ($T/T_m \sim 0.4$) the increase in mobility accelerates the processes just described for the three films, leading to significant changes in morphology and exposure of the substrate. In $Ru_{(l)}$, dewetting is mostly characterized by void nucleation, and appears to be less strong than in $Ru_{(h\text{-}l)}$ and $Ru_{(h)}$. It is localized to sparse holes with dimensions of a few hundred nanometers. These have a spatial density much lower than that of the grain boundaries, thus their formation may not be due to grooving. Other authors have attributed the nucleation of voids to excess vacancies that would collect at the interface with the substrate, and explained it as a stress relief process [93],[94]. The remaining Ru film shows high crystallinity, with grain sizes varying from 40 to 200 nm, and a dominant orientation, preferentially exposing the (100) surface plane, as we will discuss later.

In $Ru_{(h\text{-}l)}$ and $Ru_{(h)}$, dewetting proceeds with further edge retraction at the grain boundaries, resulting in a highly exposed Si substrate and irregular Ru agglomerates.

In the following, we would like to discuss additional phenomena that are likely at play in our experiments, in particular at the highest temperatures. They involve the formation of compounds and the relaxation of stress. As our own experiments provided merely circumstantial evidence on the composition, we are forced to resort to speculations on these subjects, which we will support with references to previous literature.

To begin with, the difference in surface free energy between Ru and Si is large ($\gamma_{Si} = 1.1\,J/m^2$ and $\gamma_{Ru} = 3.4\,J/m^2$ at 25 °C [95]) and provides a driving force for diffusion of the substrate Si atoms to the Ru surface [96],[97]. However, as long the Ru film is closed, such out-diffusion of Si is prevented. We note that the presence of the native oxide layer may act as an additional barrier against such a process. When, as a consequence of annealing, the Ru film exposes parts of the substrate, the native oxide can

desorb, allowing Si atoms to interact with Ru. From the phase diagram of Ru-Si (reported in Chapter 1), we find that Si is not soluble in Ru. Therefore, the Si atoms will not tend to diffuse into the Ru layer, but rather will use the open pathways to reach the surface and wet the higher-surface energy metal. Such a mechanism may be at the origin of the bright agglomerates that appear at sparse locations in the SEM images of Ru(h-l) and Ru(h) at 700 °C (see Figure B3 for zoomed-in micrographs). We propose that these consist of either Si or Ru (or a mix of the two) that has subsequently oxidized upon exposure to air, as the high secondary electron emission coefficient of oxygen would explain the high brightness of the structures.

In their work on annealed 10 nm-thick Ru films deposited on a thick SiO_2 layer, Coloma Ribera *et al.* reported the formation of rod-like structures as a consequence of annealing [86]. The authours argued that the thick silicon oxide layer blocked a direct interaction between Ru and Si, and the formation of rods was ascribed to thermal oxidation of Ru. This would suggest that the bright crystallite rods in $Ru_{(h\text{-}l)}$ consist of oxidized Ru.

In contrast with the open structures of $Ru_{(h\text{-}l)}$ and $Ru_{(h)}$, the dense and continuous initial structure of $Ru_{(l)}$ appears to block more effectively native oxide desorption, thereby suppressing the diffusion of Si atoms to the surface and the formation of large agglomerates. On the other hand, it is possible that the $Ru_{(l)}$ layer has uniformly oxidized.

The development of regions with markedly different SEM contrast in the Ru films at 800 °C (Figure 3.3*O, P* and *Q*) may be explained by ruthenium silicide formation. Ruthenium is known to form a variety of compounds with Si, among which, Ru_2Si_3, RuSi and $RuSi_2$ are the most commonly observed [21],[22]. The Si-rich phase of Ru_2Si_3 is the most stable one in the Ru-Si equilibrium phase diagram (see refs. [26],[100] and Chapter 1 of this thesis). Therefore, we propose that the dark regions in our SEM images are rich in Si (as suggested by the lower secondary electron emission) and likely consist of Ru_2Si_3, while the bright ones are rich in Ru. The notion that the dark regions contain Si is also supported by our observation that their sizes are increased after doubling the annealing time (see Figure B4), consistent with an increase in the amount of Si available for the formation of a stable ruthenium silicide.

In $Ru_{(l)}$ and $Ru_{(h)}$ at 800 °C we observe the appearance of rectangular, darker regions (Figure 3.3*O* and *Q*, respectively). These have likely followed from the consumption of the Si substrate [101],[102]. The retreat of the step edges of the Si(100) substrate induced by the out-diffusion of Si atoms is compatible in fact with the **[011]** and **[0$\bar{1}$1]** orientation of the rectangular shapes seen in both films. On the other hand, in $Ru_{(h\text{-}l)}$ (Figure 3.3*P*) we find dark fractal-like patches. At present, we do not have enough information to ascribe these shapes to a specific mechanism.

Finally, an additional driving force for the changes in morphology with temperature is stress [103]. Stress can be extrinsic, for example when it arises from the heating of a film on a substrate, where the two respective materials have different thermal expansion coefficients. This extrinsic stress is probably modest compared with the second source of stress, which is intrinsic. Intrisic stress builds up already during deposition and is known to be influenced both by material properties [33],[34] and by the employed deposition method [31],[32]. In particular, it has been shown that by changing the Ar pressure during sputter deposition, the sign of the stress may even be inverted. Negative stress (compressive) is presumably due to a so-called peening effect, as proposed by D'Heurle [106] and more recently demonstrated by Chason et al. [107]. Positive stress (tensile), on the other hand, is a natural consequence of grain boundary formation, which increases with the thickness of the layer in the case of materials with low mobility, such as Ru. Interestingly, close-to-zero residual stress has been reported in deposited layers with opposite stress signs, which appear to partly counterbalance one another [108]. Louis et al. [14] provided an overview of possible methods that can be used to decrease the net stress of a multilayer system by introducing stress compensation layers. Alagoz et al. [77] monitored the stress as a function of thickness in Ru films grown under low, high and alternating low and high Ar pressures, showing that, for the same layer thickness, these depositions result in high-compressive, low-tensile and close-to-zero-tensile residual stresses, respectively. According to their findings, we argue that the intrinsic stress in our films is tensile (and low) in the case of $Ru_{(h\text{-}l)}$ and $Ru_{(h)}$, while it is compressive (and high) in the case of $Ru_{(l)}$. The sign of the stress is important, as it will drive the direction of diffusion of the atoms.

A number of additional experiments would be extremely useful in order to shine light on the evolution of the three Ru films with temperature and on their final morphological properties. For example, we propose to perform further XPS meaurements to follow the changes in the intensities and positions of the characteristic core levels of Ru and Si during annealing, which would allow us to assess the evolution in chemical composition and distinguish the different silicide phases. For an absolute measurement of the densities of the Ru films we propose to use X-ray reflectivity measurements (XRR). X-ray differaction (XRD) could provide additional information on the phases of the various silicides, as well as on the strain in the film. Substrate curvature measurements could also be insightful for determining the stress before and after deposition, and before and after annealing. For applications where continuity of the films is important, we propose to assess this property by measuring the films' sheet resistance by use of four-point probe measurements. Further experiments could also be devoted to repeating the same experiments with a few deliberate changes, such as: (1) stripping the native silicon oxide via hydrofluoric acid etching, prior to metal deposition; (2) growing an extra thick silicon oxide layer, prior to metal deposition; (3) annealing the film+substrate samples in an N_2 atmosphere, rather than in dry air; (4) varying the ratio between the thicknesses of the layers that are sputter-deposited at high and low Ar pressure to form the $Ru_{(h\text{-}l)}$ films.

3.5 Conclusion

The thermal stability of ultrathin metal films is a necessary requirement for a vast number of applications. In our work, we investigated the thermal stability of $\sim$ 6 nm-thick Ru films on silicon with different initial morphologies. We reported on the evolution of these films as a function of annealing temperature, as observed by SEM, AFM and XPS measurements, quantifying the changes in terms of rms roughness, correlation length and Hurst exponent.

Films deposited at low pressure (2.7×10^{-3} mbar) showed a dense and uniform structure, with fine grains separated by shallow boundaries. On the other hand, the films deposited at high pressure (2.7×10^{-2} mbar) and the bilayer (deposited at 2.7×10^{-2} mbar followed by 2.7×10^{-3} mbar)

showed a more open and rough structure, with larger thickness variations in the form of deep boundaries surrounding grainy clusters. As revealed by XPS measurements, all as-deposited films were fully closed as no Si peak was detected.

In the evolution of the three Ru films with temperature, the most important finding is that the two films with a more open structure appear remarkably stable up to at least 600 °C. We propose that their structure is stabilized by the deep grain boundary grooves, surrounding the grainy clusters. On the other hand, the Ru films with a dense and initially smooth surface evolved more readily, showing a doubling of the average grain size already at 500 °C and a proportional increase in roughness, which scales approximately linearly with further raising in temperature.

At the highest annealing temperature of 800 °C, all films showed dewetting. We observed two main different types: (1) nucleation and growth of local voids in the dense Ru films, and (2) film break-up and separation at the deeper grain boundary grooves in the other two films.

Additional measurements will be required to investigate in further detail the evolution of ultrathin Ru films in terms of their chemical composition, grain orientation and film continuity and the role played in this by compound formation and stress development.

More generally, we hope that our study can provide new perspectives for controlling the thermal stability of ultrathin films of Ru and other refractory metals. The strategy explored here of changing the Ar deposition pressure may be beneficial also for tailoring the properties of films whose application does not involve high temperatures and in which the observed nanoscale morphology would be the desired outcome.

4

A combined STM and stress sensor setup for real-time studies of thin film growth

It is well known that stress arises during film growth and that it is directly linked to the atomistic mechanisms involved in the formation of the film's microstructure. In order to study the correlation between growth mechanisms and internal stress in thin films, we developed a new, combined experimental setup that is capable of imaging the surface of a growing film in real time while simultaneously monitoring substrate curvature changes. This system consists of an in-situ Scanning Tunneling Microscope (STM) and a Multi-beam Optical Stress Sensor (MOSS). As a proof-of-principle experiment, we present morphological and stress studies of the growth of ruthenium deposited by electron-beam evaporation on a Si(100) cantilever substrate.

4.1 Introduction

Stress in thin film-based devices is a persistent problem for modern technology. This stress originates from imperfections in the layers, such as lattice mismatch or free surfaces and interfaces, and is particularly strong in polycrystalline thin films. As-grown polycrystalline films develop internal compressive or tensile forces [109],[110] that can easily reach 1 GPa and cause mechanical failures such as cracking, peeling-off and blistering [76],[111]–[113]. Even when stress does not cause plastic deformation, it can still alter the physical properties of the films or render them more prone to the degradation processes just described, when external factors come into play (e.g., high temperatures or exposure to gases). In other cases, stress can be beneficial – for example, tempered glass is a material made tougher by introducing a compressive stress on the surface, by tuning the deposition conditions.

In general, understanding the origin of intrinsic stress in deposited films enables better control over the device performance, and thus has motivated a substantial amount of research. Despite recent progress [114], certain aspects of stress generation remain a subject of debate, largely due to the limited number of experimental techniques capable of capturing the atomistic phenomena at the basis of film growth, and their correlation with stress.

In this work, we developed an experimental setup that allows to image in real time the surface of a growing film with nanoscale resolution and simultaneously monitor associated substrate curvature changes. It consists of a custom-made Scanning Tunneling Microscope (STM) [58],[115],[116] integrated with a Multi-Beam Optical Stress Sensor (MOSS). To demonstrate the working principle of our combined STM-MOSS system, we present a preliminary study of the growth of ruthenium (Ru) deposited by electron-beam evaporation on a Si(100) cantilever substrate.

4.1.1 Stress in Volmer-Weber films – knowns and unknowns

Generally, metal films deposited at room temperature on a lower-surface-free-energy substrate (such as silicon or mica) follow a Volmer-Weber type of growth, i.e. a growth mode that starts with the formation of three-dimensional islands that coalesce at a later stage, leading to a polycrystalline structure. During deposition, internal forces develop in the film that are closely linked to the different growth stages, namely (I) nucleation, (II) coalescence and (III) post-coalescence (see Figure 4.1). The character of these forces depends on the material properties of film and substrate, and on the deposition process [27]. Here, we restrict ourselves to ultra-high vacuum (UHV) electron-beam evaporation at room temperature, where the growth of the film, and thus, the intrinsic stress, are predominantly influenced by thermodynamic factors[§]. In particular, the melting point of the deposited material, which is roughly proportional to its cohesive energy, determines to a large extent the activation energy for the diffusion of the deposited atoms on the surface. This, as we will see shortly, leads to two different types of possible behavior of the stress in the final stage of film growth [109].

In Figure 4.1, we show the typical behavior of high- and low-melting-point materials. The stress is expressed in terms of force per unit width, as frequently used in the literature. The positive and negative values indicate tensile and compressive stress, respectively. The average stress throughout the entire film at a specific stage during the deposition is obtained by dividing the corresponding force per unit width by the film thickness. Geometrically, this is equivalent to the slope of the line connecting the origin of the graph to that point. If the stress relaxation rate can be ignored during the experiment, the slope of the curve at each point is equal to the so-called "incremental stress". This corresponds to the stress within the last added layer of the film at that specific time during the deposition [110].

[§] In other Physical Vapor Deposition (PVD) methods such as sputter deposition, additional factors such as the working gas pressure play a major role on film growth and intrinsic stress [150].

Although the connection between film growth and stress is still a subject of research and discussion, general trends related to the different stages of growth can be identified (see Figure 4.1). In the nucleation stage, three-dimensional islands nucleate on the substrate. These islands are usually subjected to compressive stress, which is attributed to the action of the surface and/or interface stress that reduces the lattice spacing in a very small isolated crystallite compared with the spacing in a bulk crystal of the same material [109]. By further growth, the surface to bulk ratio of the islands decreases and hence their equilibrium lattice constant asymptotically increases toward the bulk value. However, when the islands are firmly attached to the substrate, the substrate resists this lattice expansion. This is responsible for the development of a compressive stress within the islands during the initial nucleation-and-growth stage (Figure 4.1) [12],[13]. In the literature, this phenomenon is also referred as capillary effect [119].

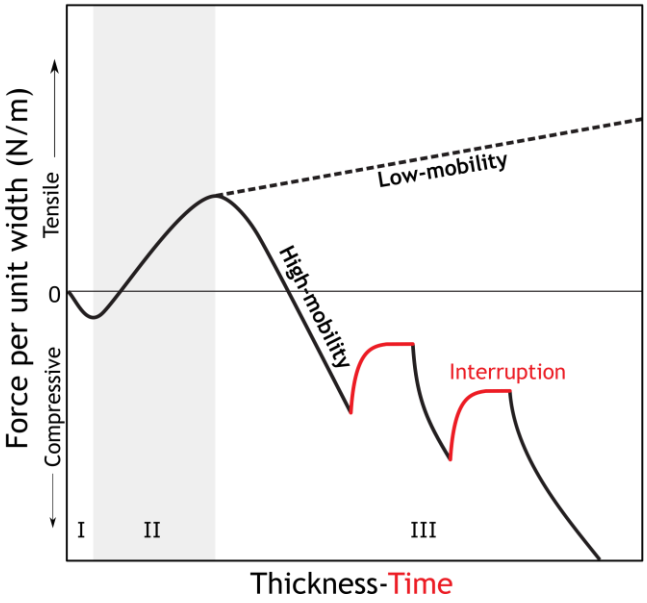

Figure 4.1 Schematics of the stress evolution as a function of thickness in Volmer-Weber polycrystalline films, in the case of high (solid line) and low (dashed line) adatom mobility, after references [120],[121]. The main stages of growth, i.e. nucleation, coalescence, and thickening are indicated with Roman numbers. The red sections represent the stress as a function of time upon interruption of the deposition process.

In the coalescence stage, the three-dimensional islands come into contact. In most cases, the crystallographic orientations of the islands are all different, as a result of which, this contact cannot lead to a seamless merger but rather introduces grain boundaries. The interfacial free energies of grain boundaries are lower than the surface free energies of the islands. Therefore, it has been proposed that once islands make contact, they tend to snap together and partly "zip up" [122], in order to reduce the total interfacial free energy of their surfaces and grain boundaries. Thus, during the so-called coalescence stage, the stress becomes increasingly tensile [123],[124].

While there is consensus on how the stress develops in the first two stages of growth, certain aspects of stress generation in the final stage (post-coalescence regime) remain a subject of debate. Previous research has shown that, after the completion of island coalescence and the formation of a continuous films, the stress evolution follows two different types of behavior, depending on the adatom mobility [109],[125]. The mobility, in turn, depends on the reduced temperature T/T_m [76],[126] (where T is the absolute temperature of the substrate and T_m is the melting point of the deposit material) and on the deposition flux [121],[127],[128]. In general, without sufficient mobility, the incremental stress stays tensile on further deposition and is constant with growth interruption (dashed line in Figure 4.1), whereas when the mobility is high enough, the total stress decreases until it becomes compressive again (solid line in Figure 4.1) [120]. The compressive stress in the post-coalescence stage has been shown to have a partly reversible nature [114]: upon interruption of the deposition, the stress jumps to more tensile (less compressive) values; by resuming the deposition, the stress returns to the compressive level it showed prior the interruption (see Figure 4.1).

Different explanations have been proposed for the observed phenomena [121],[129]. However, until today there has been no general agreement about the validity of these models. Our combined setup provides the opportunity to verify the validity of the proposed models in a direct experimental manner, in addition to providing the opportunity to discover new phenomena that may not have been recognized until now.

4.2 Description of the experimental setup

4.2.1 Real-time STM

We make use a special custom-made STM, capable of reaching scanning speeds higher than 1 frame per second (fps) with a resolution of 256 × 256 pixels [58] and appositely designed to image a surface while depositing material. These qualities make our STM an excellent tool for investigating film growth dynamics. The details of this particular STM setup and its performance have been presented in previous reports [58],[115],[116].

The STM system is integrated in an ultrahigh vacuum (UHV) chamber, pumped by a combination of a turbomolecular pump, an ion getter pump and a titanium sublimation pump. The UHV system is equipped with a separately pumped load lock chamber to exchange samples (together with their holders) without the need to break the vacuum of the main chamber. The sample holders (see Section 4.2.3) are constructed such that they make it possible to heat the samples. An ion gun is installed for Ar ion bombardment of the surface, as a part of the preparation (cleaning) procedure, or for operation during STM imaging. Like the electron-beam deposition sources, the ion gun is mounted under a grazing angle of 15°, with respect to the surface plane of the sample, in order to enable the combination of ion irradiation with live STM imaging. The entire UHV system is mounted on a sturdy frame that is supported by pneumatic vibration isolation legs. Internally, the STM system is suspendend by springs. In principle, this makes it possible to perform atomically resolved imaging of surfaces. The present work is focusing on roughness and larger-scale morphology and was performed with lower resolution.

4.2.2 In-situ stress monitoring

The two main techniques that are typically used to measure the internal stress of thin films are X-ray diffraction and sample bending. The first method uses the fact that the lattice constants of a stressed material deviate from their equilibrium values [130],[131]. By measuring the average atomic distances in the film with X-ray diffraction and thus quantifying the lattice strain, one can calculate the internal stress, when the Young's

modulus and the Poisson ratio of the material are known. The sample bending method uses instead the fact that a stressed film exerts equal and opposite forces on its substrate [16], which, depending on the stress sign, bend the substrate in either a convex or concave shape [132]–[135].

The curvature of the substrate can be measured using various techniques, including the monitoring of the differential capacitance between the substrate and a nearby electrode plate [132],[136] or the deflection of one or multiple light beams from the surface [28-31]. An advantage of the multi-beam reflection method is its outstanding insensitivity to rigid motion of the sample [133]. Mechanical vibrations of the sample may induce variations in the positions of the individual laser spots. However, all translational movements of the sample in either x-,y- or z- directions with respect to the optical system result in equal displacements of the individual spot positions, and thus the variations cancel out.

A multi-beam optical stress sensor (MOSS) [135] therefore suits our purpose of performing in-situ stress measurements with sub-second time resolution. The cancellation of the effects of rigid tranlsations is of extra importance in our case, in view of the spring suspension of the STM system within the UHV chamber, which leads to small-amplitude relative displacements of the sample with respect to the optics of the MOSS system during simultaneous stress and STM observations (see next section). The optical configuration of our MOSS setup is illustrated in

.

By shining a laser beam on an etalon, the laser beam undergoes several internal reflections, which generate two sets of parallel beams, leaving the etalon on each side. The parallel beams from one set are then directed towards the substrate, where they reflect toward an optical sensor. Depending on the curvature of the substrate, the reflected beams slightly diverge or converge.

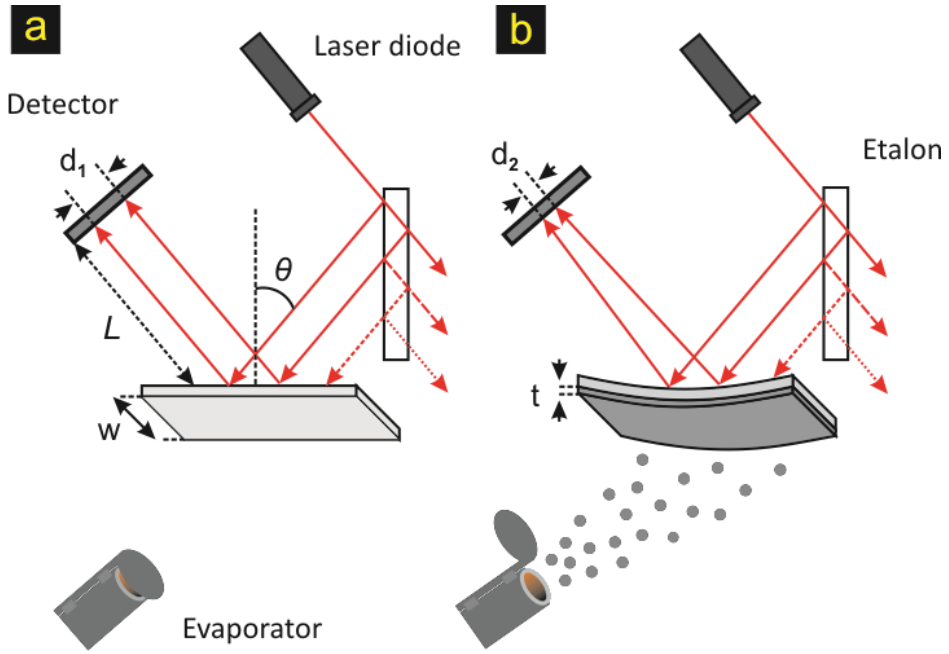

Figure 4.2 Schematics of a multi-beam optical stress sensor (MOSS). (a) The process of creating a parallel beam array using an etalon is illustrated. The beam array is reflected back by the rear side of the substrate towards the optical sensor. (b) The substrate is bent due to the film deposited on it. The corresponding relative change in the inter-spot distance on the optical sensor is equal to $(d_2\text{-}d_1)/d_1$.

The curvature of the substrate is proportional to the force per unit width in the film, F/w, which is equal to the product between the average stress $\langle\sigma\rangle$ and the film thickness t_f. Using Stoney's equation [29]:

$$\frac{F}{w} = \langle\sigma\rangle \cdot t_f = \frac{1}{6} \cdot \frac{E_s}{(1-\nu_s)} \cdot \kappa_s \tag{4.1}$$

Here, $E_s/(1-\nu_s)$ is the biaxial modulus of the substrate and κ_s is the curvature of the substrate.

For the general case shown in

the substrate curvature can be calculated from the change in distance between the spots d on the sensor screen [135]:

$$K_s = \frac{d_2 - d_1}{d_1} \frac{cos\,\theta}{2L} \tag{4.2}$$

Here L is the distance between the reflection point on the substrate and the sensor screen and θ is the angle between the beams and the projection of the substrate normal on the beam array plane. By combining equations 4.1 and 4.2 one can calculate the average stress $\langle\sigma\rangle$ in the film for a known film thickness.

4.2.3 Integrated STM/MOSS system

Figure 4.3 shows the design of our integrated STM/MOSS setup. The laser module (item 1) contains a 635 nm wavelength, 4.5 mW laser diode (item 8). The collimated laser beam (using the lens at the output of the laser diode) has an elliptical cross section with full width half maximum (FWHM) dimensions of 2.45 and 0.54 mm and divergences of 0.6 and 1.8 mrad, respectively. A 6 mm thick slab of fused silica with surface parallelism better than 10 arcseconds is used to split the original beam into parallel beams (item 7). The separation of the parallel beams can be adjusted between 1 to 4.8 mm by regulating the incident angle of the laser with respect to the etalon.

For the alignment, the whole laser module is mounted on a combined XY tilt + XY linear transfer + Z rotation stage (item 10). The two parallel beams (item 9) are then directed via a viewport into the UHV chamber, towards the sample holder (item 11). The sample holder is designed to allow the laser beams to enter and reach the rear side of the sample (item 18 and Figure 4.4) from the top flange of the chamber. When the sample holder is placed on the STM scanner (item 12) its top side reflects the laser beams to the viewport with the optical sensor (item 2). The bottom side, on the other hand, is accessible to the STM tip (item 19) and to the fluxes of an ion sputter-gun (IQ100 ion source with Wien-filter from Kremer Vakuumphysik GmbH) and a 4-pocket mini e-beam evaporator (EGCO4

Oxford Applied Research) (items 3 and 4). These two items are positioned behind the scanner and are only partly visible. The atomic flux can reach the sample via one of the three apertures in the scanner body (item 14). The sample holder includes a tungsten filament (item 15), which can be used to heat up the sample. This design makes it possible to simultaneously perform STM scanning and stress monitoring, during film deposition and ion erosion. Additionally, one can also measure the stress during heat treatment. This, however, cannot be combined with simultaneous STM imaging, due to thermal drift.

The substrate sample used for the STM/MOSS experiments has its own special structure. It consists of a cantilever (item 18 in Figure 4.3) connected to two wings on either side. Each wing is connected via a short bridge located at the midline of the long edge. These two side wings are resting on the sample holder cup (item 17) and are clamped down by molybdenum leaf springs (item 16). In this configuration, the cantilever is exposed to the deposition flux, while the side wings are shadowed by the sample holder cup. In principle, the design is such that when the stress in the deposited film causes the substrate to bend, the middle of the cantilever stays at the same height since it is being held by the bridges. This is where the STM tip is positioned (item 19). Maintaining the sample fixed at this point is essential for stable tunneling. At the same time, the maximum displacement in the curved cantilever occurs at its two free ends, where the two laser beams are reflected.

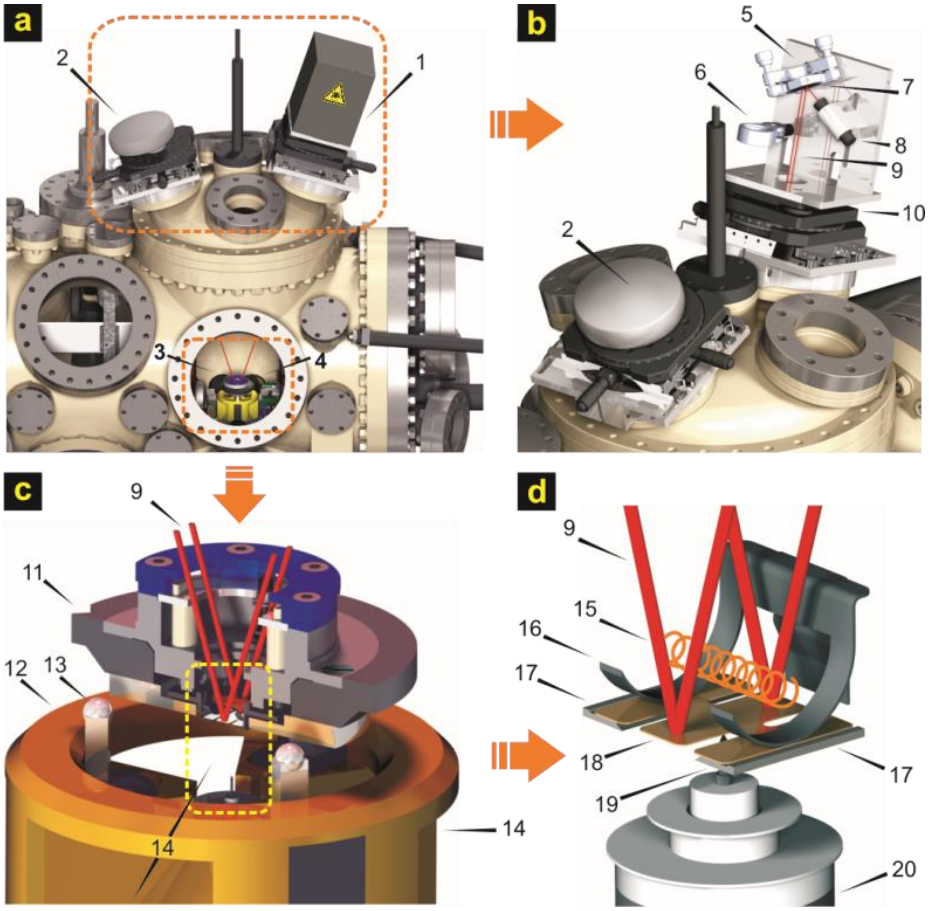

Figure 4.3 The integrated STM/MOSS setup: (a) Overview of the ultrahigh vacuum chamber: 1. laser module, 2. optical sensor module, 3. sputter gun, 4. deposition gun, (b) Close up view of the MOSS modules: 5. XY tilt mount of etalon, 6. flip mount for Neutral Density (ND) adsorptive optical filter, 7. etalon, 8. laser diode, 9. parallel laser beams, 10. combined XY tilt + XY linear transfer + Z rotation stages, (c) Close up view of the STM scanner and sample holder cross section: 11. sample holder, 12. STM scanner, 13. approach piezo "ant" motors, 14. scanner aperture for ion sputtering and deposition, (d) Close up view of the sample: 15. tungsten filament, 16. molybdenum leaf spring, 17. sample holder cup, 18. sample, 19. STM tip, 20. STM piezo element.

The samples were fabricated by using photo-lithography and deep reactive ion etching to obtain the shape shown in detail in Figure 4.4.

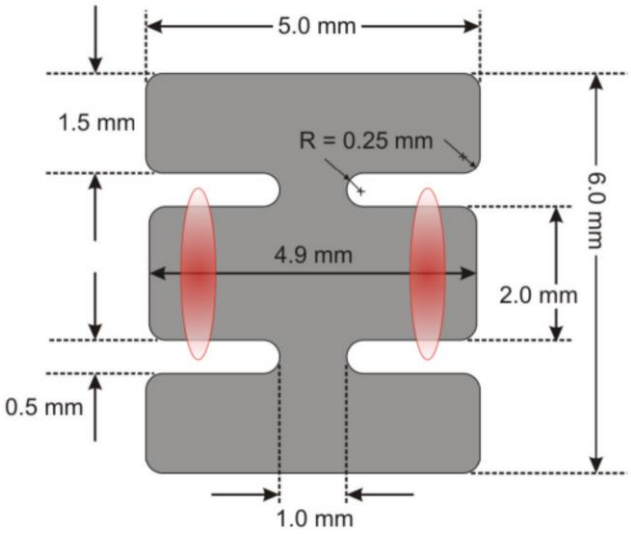

Figure 4.4 Sample design. The central cantilever area is dedicated to simultaneous STM and stress measurements. The outer two wings serve to clamp the sample in its holder and are shielded from the flux of atoms (deposition) or ions (erosion). Red elliptic regions represent the areas of incidence of the two parallel laser beams.

To maximize the sensitivity of our measurements, we aimed at obtaining the highest bending in the cantilever for any given stress. According to Equation 1, the bending effect produced by the stressed film is greater with thinner substrates. For this reason, our samples are fabricated out of 50 μm-thick Si(100) wafers, the thinnest commercially available. Moreover, the cantilevers are oriented along the <100> direction, which is direction with the lowest biaxial Young's modulus of silicon and offers a value of $E_s / (1-\nu_s) = 180.6$ GPa [137].

After the laser beams are reflected from the sample, they exit the vacuum chamber via a viewport and enter the optical sensor module (item 2 in Figure 4.3). The optical detector in our case consists of a 6.6 megapixel CMOS sensor with 3.5×3.5 μm^2 pixel size. The large sensor area makes the alignment procedure easy while the small pixel size further optimizes the stress measurement resolution. CMOS optical sensors provide more

control level and flexibility than the equivalent CCD sensors. For example, by limiting the capture window to the area around the laser spots one can obtain frame rates significantly higher than the equivalent CCDs.

While the laser and optical sensor modules are fixed on the UHV chamber's viewports, the STM module - weighing approximately 18 kg – can move, as it hangs from four springs [58]. While the mechanical filtering effect of the mass-spring assembly is important for imaging, oscillations of the STM platform cause the reflected laser spots arriving on the optical sensor to oscillate with the same frequency. As will be shown, the combination of the mass-spring assembly, which by design filters out mechanical vibrations above 1.3 Hz, with the dual-beam sensor, which cancels out changes in spacing due to translational movements of the suspended STM for the MOSS module, allows this setup to achieve stable STM imaging and low noise levels in the MOSS signal.

For the stress data acquisition, a LabVIEW script, running on a dedicated PC, controls the sensor and analyzes each frame immediately after it is captured. For each frame, the distance between the spots is calculated and stored in a data file. In addition, a Digital-to-Analog-Converter card is used to convert the calculated $(d_2\text{-}d_1)/d_1$ value to an electrical signal that is provided to one of the input channels of the STM electronics. In this way the stress signal can be recorded as an additional channel in the STM data files. This makes the direct mapping possible between the evolution of the topography and the stress evolution, without the risk of offsets in the timing of both measurements.

4.3 Performance

4.3.1 Stability and resolution of the MOSS module

The maximum data acquisition rate of our MOSS module is determined by the optical sensor characteristics and settings, the combination of the employed programming language and the code efficiency and the CPU speed. Without implementing any special optimization of either the software or the hardware, the MOSS module is able to record more than 18 stress data points per second, corresponding to a 54 ms time resolution.

Given that the fastest observed stress variations in the literature typically take place with time constants in the order of 20 seconds, this time resolution is sufficient to capture the stress phenomena we aim to explore (see Section 4.1.1).

The noise characteristics in the raw F/w signal recorded by our MOSS module on a Si cantilever sample are illustrated in Figure 4.5. The measurement was obtained over a period of 100 seconds, during which the stress should have been constant, as no deposition or erosion took place. The F/w signal shows a remarkable stability, with the standard deviation of the F/w data remaining limited to 2.7 mN/m. The observed F/w noise separates into a high-frequency component, above 2 Hz, with a standard deviation in the order of 1 mN/m and a component at much lower frequencies that is responsible for most of the observed 2.7 mN/m. We associate the high-frequency component with the residual effect of the mechanical vibrations of the STM chamber, the STM spring system, and/or the cantilever sample, and ascribe the lower-frequency component to external factors such as the ventilation system, floor vibrations and temperature changes.

Few factors limit the performance of our MOSS instrument. First of all, as mentioned before, due to the limited space and small size of the sample only two laser beams are used to measure the stress. In commercial MOSS devices, where there is no such limitation for the sample size, arrays of of more than two laser beams can be directed onto the surface, thus allowing for an even more accurate measurement of the sample curvature [135].

Secondly, the presence of the two side wings, attached to the center of our cantilevers, can have an influence on the curvature of our samples during thin film growth and introduce an error in the derived stress values. In traditional MOSS measurements, samples are usually fixed on one end, with the entire cantilever left free to bend. These two differences between our MOSS system and others, may introduce modest systematic errors and noise in the stress values measured by our MOSS device. Nonetheless, the high time resolution and excellent stress sensitivity make our MOSS system a very useful tool to obtain relevant insights into the precise relation between the morphology and the forces of growing thin films.

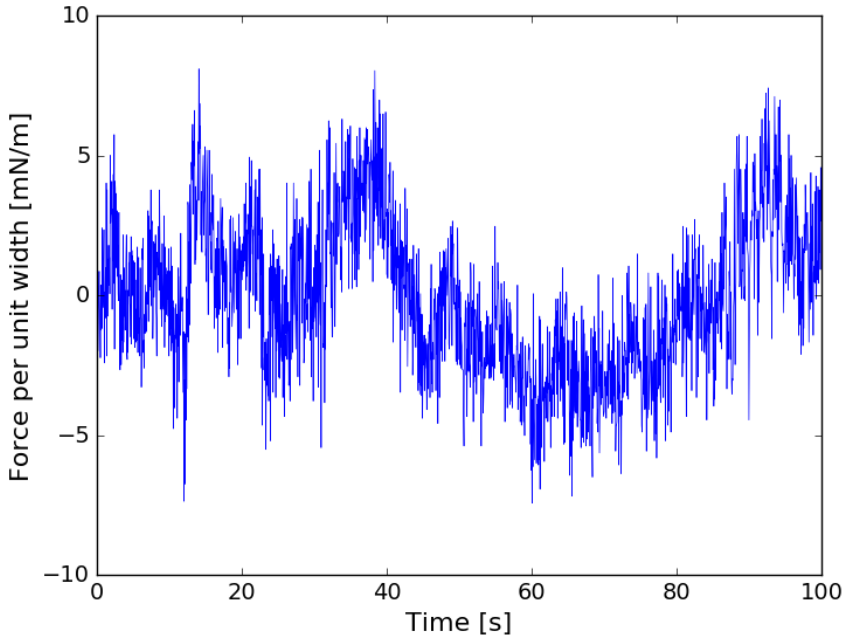

Figure 4.5 Raw F/w signal recorded by the MOSS module during a time window of 100 seconds, during which the Si substrate was not subjected to atom or ion beams. The time resolution and standard deviation of F/w readings were 54 ms and 2.7 mN/m respectively.

4.3.2 STM and stress measurements during Ru growth

Here we present an example of a combined STM-stress study of the growth of Ru on a Si(100) cantilever substrate. For further comparison, in the *Appendix C* we report an additional stress experiment, where we show the stress evolution during the growth of silver (Ag), using the same setup.

Prior to the deposition, the Si surface was prepared by removing the native oxide using Ar^+ ion bombardment at a grazing incidence angle (75° from the surface normal). We used an ion energy of 800 eV and an ion flux on the sample of 2.6×10^{20} ions s^{-1} m^{-2} for a total duration of 60 minutes, which resulted in a clean, amorphized Si surface. After this preparation, the sample holder was placed on the STM scanner and through an automated coarse approach the tip-surface combination was brought into the control range of the piezoelectric scanner. We then started scanning and the deposition of Ru.

Ru was deposited from a 99.95% pure rod by e-beam evaporation. The base pressure of the UHV system was below 5×10^{-11} mbar. During the deposition, the pressure did not rise above 2.3×10^{-9} mbar. Due to its high melting point (2310 °C) and relatively low vapor pressure (10^{-4} Torr at 2260 °C), Ru is difficult to evaporate at a stable deposition rate [71]. Conditioning treatments are therefore important to avoid large flux fluctuations, especially in view of in-situ STM experiments. For this reason, we slowly ramped up the power and outgassed the rod for several hours. The deposition rate was calibrated using a quartz crystal microbalance (QCM). For a filament current of 4.45 ± 0.01 A and an applied electron acceleration voltage of 2 kV, we obtained a prevalently stable deposition rate of ~ 0.05 nm/min, which is what we used in our experiments. Nevertheless, outburst of material during the experiment could not be avoided completely, which forced us to repeat the combined STM and MOSS experiment several times.

What we present in the following is the combination of measurements of the stress and the STM imaging obtained from two separate experiments: one in which we successfully inspected the growing surface by STM (Figure 4.6), without stress measurements, and one in which we measured the stress (Figure 4.7), but "lost" the tip at 1/3 into the deposition process. Owing to the fact that the experimental conditions (i.e., evaporation rate, UHV background pressure, substrate and cleaning treatment) were practically identical in the two experiments, and in view of the similarity between the STM images in the first 1/3 of the two sequences, we are confident that there are no significant differences in film growth and resulting film morphology between the two data sets. We therefore present the data from the two Ru depositions in combination with each other, e.g. by indicating with which stages of the stress evolution of the second run, the individual STM images of the first run are to be associated.

In the first experiment, constant-current STM images were recorded during the deposition at a tunneling current of 200 pA and a starting sample bias voltage of +2.0 V, which we could progressively decrease to +0.5 V as the metal covered the semiconducting surface. The resulting STM movie is available as supplementary material [138].

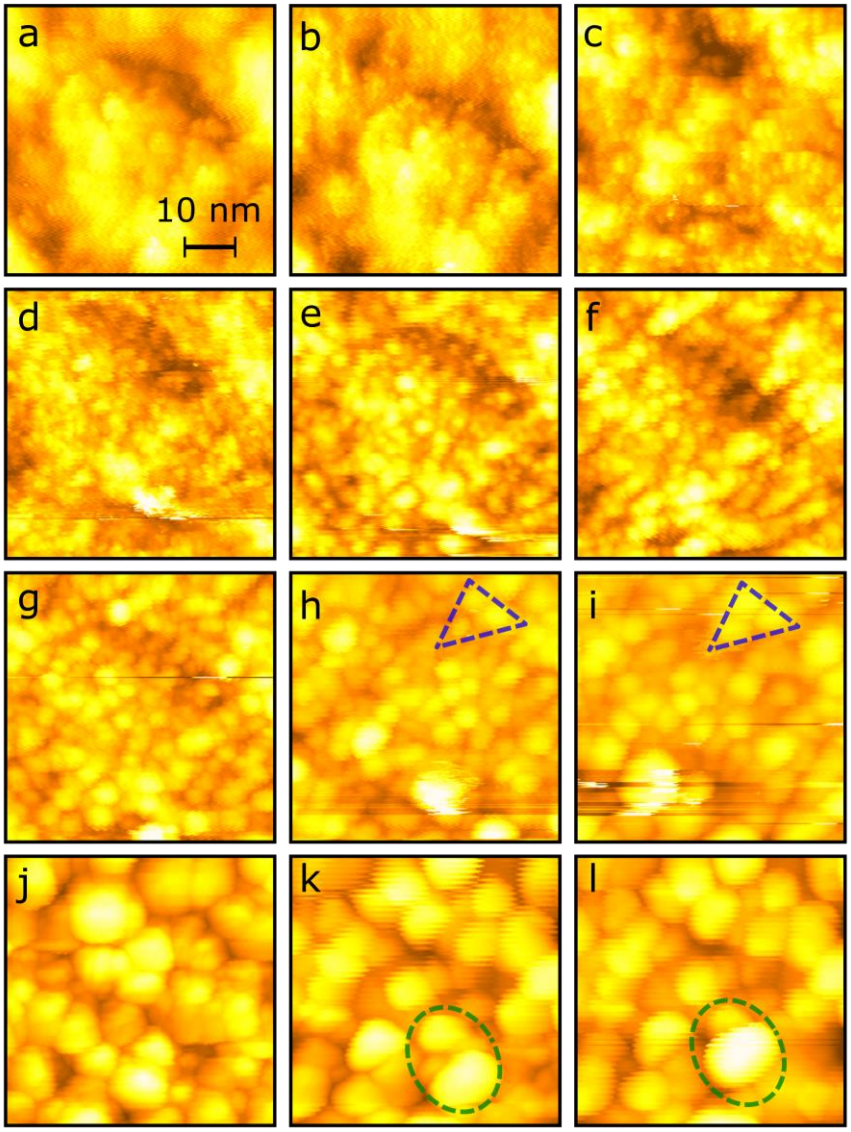

Figure 4.6 STM images (50×50 nm^2) of the growth of Ru on the amorphous Si surface. The images are part of an STM movie [138] and show the same surface area from a. to i., and from j. to l. The atomic flux came in under a grazing angle of 15° with respect to the surface plane and was directed in the images from bottom right to upper left. The images have been filtered using a line-by-line regression. The full color scale spans a. 1.09, b. 1.25, c. 1.30, d. 1.79, e. 1.87, f. 1.92, g. 2.78, h. 4.26, i. 4.38, j. 5.15, k. 5.29 and l. 5.57 nm. The marked triangles (panel h. and i.) and ellipses (panel k. and l.) show examples of GB zip-up and merging events, respectively.

Figure 4.6 shows a selection of 12 images taken from the STM movie in [138], illustrating the key stages in the morphology evolution. The 50 × 50 nm^2 images were acquired at a rate of 3 frames/min (fpm) and a resolution of 256 × 256 pixels^2. Due to thermal radiation from the evaporation source, the sample temperature rose by an estimated amount of ~ 30 °C over the course of the experiment [58]. The increase in temperature caused a drift in the STM images of ~ 30 nm/min, which we manually corrected for at the end of each frame. The deposition of Ru was stopped after 110 minutes, corresponding to a nominal film thickness of ~ 5.5 nm.

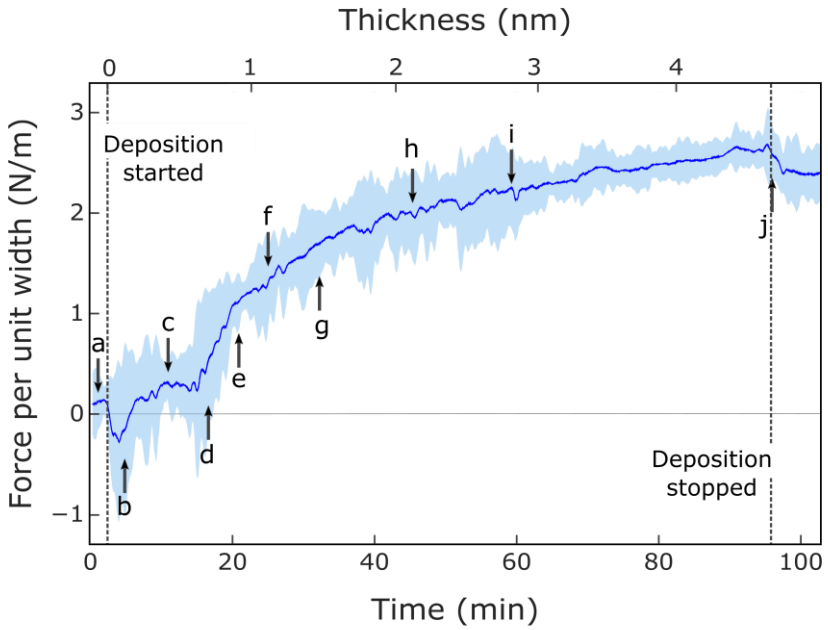

Figure 4.7 *F/w* as a function of time and thickness, during the growth of Ru on a Si(100) cantilever substrate. The shutter of the evaporator was opened at t=3 minutes and closed at t=98 minutes. The deposition rate was kept constant at 0.05 nm/min for the whole duration. The sampling rate was 43 ms. The raw data are indicated by the light blue area, while a 700-point, i.e. 30-sec, moving average is indicated by the solid blue curve. Arrows with labels indicate the corresponding STM images shown in Figure 4.6.

In the second experiment, we concentrated on the measurement of the stress. Ru evaporation was started 3 minutes after starting the recording of the data, and it was stopped after 98 minutes (note that, on the other hand, the STM experiment was stopped after 110 minutes). Using the same

evaporation rate of the STM experiment (i.e. 0.05 nm/s), we deposited in total ~ 4.75 nm of Ru. The results of F/w as a function of film thickness-time are shown in Figure 4.7. The deposition time at which each STM image of Figure 4.6 was recorded is marked in Figure 4.7, with corresponding labels. In the following paragraphs, we provide a first discussion in which we attempt to correlate the morphological developments of Figure 4.6 with the stress evolution of Figure 4.7.

Figure 4.6-a shows the amorphized Si surface that formed the starting substrate. The selected area features a characteristically shaped depression, which we used as a convenient 'landmark' in our attempts to correct for thermal drift and keep the scan area more or less the same during the experiment.

Soon after the start of the deposition we observe the nucleation of Ru islands, as can be recognized from the high density of small extra protrusions that Figure 4.6-b shows with respect to the starting configuration of Figure 4.6-a. At this deposition stage, the stress in Figure 4.7 has already dropped to negative values, indicating compressive internal forces. As discussed in Section 4.1.1, the emergence of compressive stress in the pre-coalescence stage is usually associated with capillary forces [119].

After 3 minutes of deposition, corresponding to a nominal thickness of 0.15 nm or, equivalently, ~ 1 monolayer (ML) of Ru, the number of nucleated islands has presumably already saturated, which we read off from the fact that at this stage the incremental stress (the slope in Figure 4.7) becomes tensile.

Between 3 and 15 minutes of deposition (0.15 to 0.75 nm) the stress remains close to stationary at a modest, tensile level (images c and d of Figure 4.6). At present, we can only speculate about the origin for this behavior. One observation that we can make from the images is that in these early stages of the deposition the Ru islands have sizes that are smaller than the initial roughness of the starting substrate (see caption of Figure 4.6). What we see at point -e and beyond in Figure 4.7, is that the further increase in tensile stress, after the plateau between 3 and 15 minutes of deposition, only begins when the deposited islands are large enough to 'overcome' the intial substrate roughness. We realize that this observation in itself is not an explanation, but emphasizes that it would be hard to

imagine a full explanation, in which the starting substrate configuration would not play a role in the initial stages and that it is only by directly matching the surface structure obervations with stress measurements, that this role can be identified experimentally.

After 15 minutes of deposition, the stress increases sharply, suggesting that the coalescence of grains and the formation of new grain boundaries (GBs) dominates the stress development in this stage. It has been previously reported that coalescence takes place over a relatively narrow film thickness interval, leading to a characteristic sharp increase in tensile stress [122]. Once coalescence is complete, we expect to observe the onset of grain growth.

The STM frames from -f to -l in Figure 4.6 describe the post-coalescence stage. Here the film grows in thickness from ~ 1.5 nm to ~ 5.5 nm. The reorientation of grains and the motion of grain boundaries lead to a steady growth of the average grain size and an accompanying, progressive reduction in the total number of grains, as can be recognized by comparing frame -l with the earlier growth stages, e.g. frame -f. Examples of GBs "zipping-up" and of grains merging into a larger, single grain are shown by the triangles in Figure 4.6-h and -i and the ovals in Figure 4.6-k and -l, respectively. At the final film thickness of ~ 5.5 nm, the maximum height difference measured by STM is ~ 5.6 nm.

We point out that the grazing geometry of the deposition could lead to specific textures in the resulting film structure, deriving from shadowing effects by the deposition-induced surface protrusions in combination with a low surface adatom mobility and possibly with measurable effects in the observed stress.

In Figure 4.7, beyond a thickness of roughly 1 nm the tensile stress keeps increasing, but at a slower pace. This seems to follow the low-mobility scenario, sketched in Figure 4.1. Interestingly, as already stated before, we also recognize that the average grain size increases significantly over this part of the deposition, which amounts to a strong reduction in the density of grain boundaries. We speculate that this plays an important role in the stress curve. Again, we see that the STM images identify a relevant structural development that should be taken into consideration in any

realistic explanation of the thickness dependent stress development of a growing thin metal film.

The evaporation in the stress experiment was stopped at 98 minutes (note that this time does not match the one at which the deposition was interrupted in the STM experiment, which was 110 minutes). After the termination of the deposition, we observed changes that are indicative of stress relaxation. The measured force decreases rapidly at first and then gradually levels off. Further investigations could aim at understanding the atomic-scale mechanisms behind this relaxation. An important ingredient of such an explanation could be that the system is constantly driven out of equilibrium during the deposition of material, resulting in an offset in the tensile stress. As soon as the deposition stops, however, the atoms in or on the film may have sufficient mobility to rearrange themselves to bring the system closer to equilibrium, accompanied by a reduction in the internal stress [13].

4.4 Conclusion

In this work, we presented a novel experimental setup to study the underlying origins of intrinsic stress by the combination of real-time STM imaging and multi-beam optical stress sensing. We showed that we are able to achieve adequate resolution and stability to observe the growth of ruthenium on a Si cantilever substrate and measure the accompanying stress evolution. Our setup has therefore the capability of investigating a wide range of surface and stress phenomena. With this we aim to contribute to a better control over the intrinsic stress for thin-film based technological applications.

Appendix A

Supplementary materials of Chapter 2.

A1. EUV reflectivity spectra

Here we show the calculated reflectivity profiles in the 12.5-14.5 nm spectral range for the multilayer mirrors reviewed in this article. For all cases, we calculated both the reflectivity curve for a single mirror (left panels) and that for a combination of ten consecutive mirrors in series (right panel), obtained by raising the single-mirror reflectivity values to the power 10. The reflectivity values reported in Chapter 2 (Table 2.1, 2.2 and 2.4), including the normalized, integral reflectivities, are based on the calculated single-MLM and 10-MLM spectra shown here.

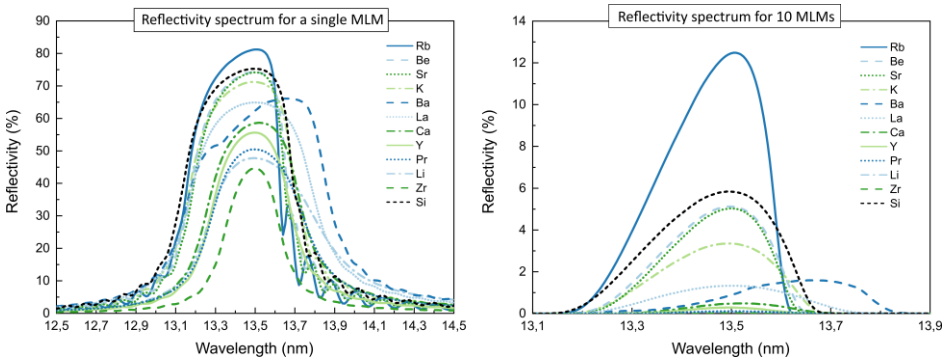

Figure A1 Calculated reflectivity spectra for Mo/X multilayer mirrors (elements X are indicated in the legend) for a single mirror (left) and for 10 mirrors in series (right). See main text of Chapter 2 and Table 2.1 for more details.

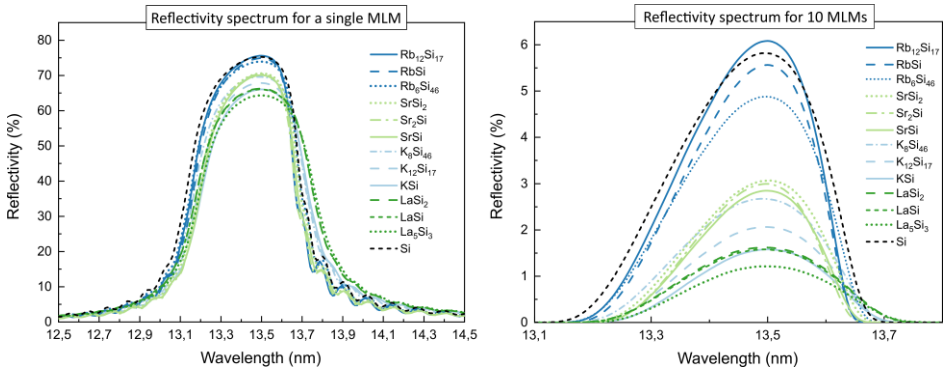

Figure A2 Calculated reflectivity spectra for Mo/X_nSi$_m$ multilayer mirrors (X_nSi$_m$ compounds are indicated in the legend) for a single mirror (left panel) and for 10 mirrors in series (right panel). See main text of Chapter 2 and Table 2.2 for more details.

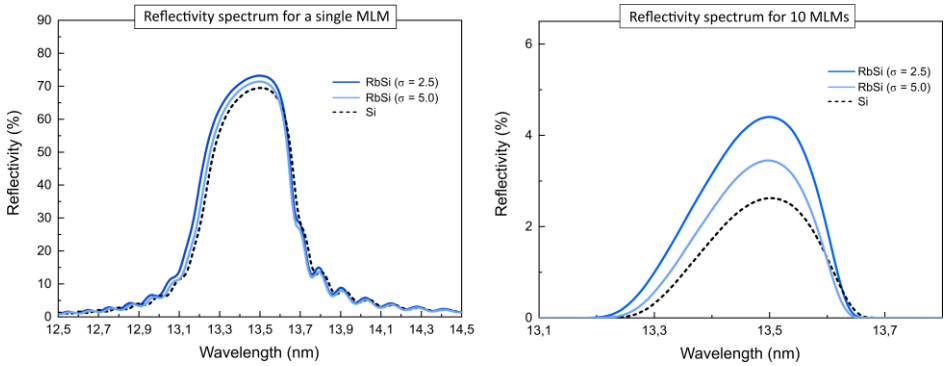

Figure A3 Calculated reflectivity spectra for Mo/RbSi and Mo/Si multilayer mirrors, for a single mirror (left panel) and for 10 mirrors in series (right panel). Where applicable, the diffusion barriers are mentioned after the slash sign. The assumed interface width values (σ) values are indicated for the two Mo/RbSi mirrors. For the Mo/Si mirrors we took into account the presence of B$_4$C diffusion barriers and an interface width. See main text of Chapter 2 and Table 2.4 for more details.

A2. Calculation of the chemical shift in Si induced by the formation of rubidium silicide

The precise magnitude of the chemical shift of the L-edge in Si (~100 eV) depends on the spatial arrangement of the atoms and the nature of the chemical bonds within the silicide. Qualitatively, the chemical shift of the

absorption edge is proportional to the effective charge of the absorbing ions [55]. The negative charge transfer to Si is expected to be strong for Rb_nSi_m, as Rb has one of the lowest electronegativity values in the periodic table. Suchet's empirical rule approximates the effective charge of an ion, q, in a binary compound as [55]:

$$q_{a(c)} = u_{a(c)}\left(1 - 0.01185\left(\frac{z_{a(c)}}{r_{c(a)}} + \frac{z_{c(a)}}{r_{a(c)}}\right)\right) \quad \text{(A1)}$$

where u is the oxidation state of an ion, z the total number of electrons, r the ionic radius, and the subscripts a and c denote anions and cations, respectively. For Rb_nSi_m, the predicted effective charges of Rb ($z_c = 37$, $r_c = 0.148$ nm, $u_c = +1$) and Si (z_a=14, $r_a = 0.384$ nm, $u_a = -1$) are $q_c = +0.77$ and $q_a = -0.77$ electrons per atom. Here, for r_c and r_a, the Pauling ionic radii of Rb^{+1} and Si^{-1} have been used [139]. From the experimental L-edge absorption data of SiC, Si_3N_4, SiO_2, and SiF_4 [140], the proportionality factor between the chemical shift of the L-edge and the effective charge the Si is estimated to be 1.24 eV per electron per atom (the R^2-value for the linear fit being 0.12). From this we deduced the value of approximately -1 eV for the chemical shift of the Si L-edge in Rb_nSi_m used in the main article.

A3. Calculation of the reaction enthalpy for the formation of molybdenum silicide in Mo/RbSi multilayer mirrors

Here we show the calculations performed in order to obtain the enthalpy values for the formation of molybdenum silicide in Mo/RbSi MLMs reported in Table 2.3, Chapter 2. We first calculated the enthalpy of formation for molybdenum silicide in Mo/Si MLMs, in the following way. There are three known Mo_nSi_m phases Mo/Si MLMs: Mo_3Si, Mo_5Si_3 and $MoSi_2$ [59],[60]. Their reaction equations (see Eq. A2, left side) lead respectively to the enthalpies of formation for one mole of atoms in Mo_nSi_m (see Eq. A2, right side):

$$\tfrac{1}{4}\mathrm{Si} + \tfrac{3}{4}\mathrm{Mo} \rightarrow \tfrac{1}{4}\mathrm{Mo_3Si} \qquad \Delta H_r = \tfrac{1}{4}(-122.1 \pm 6.0) = -30.5 \pm 1.5\ \mathrm{kJ} \quad \text{(A2a)}$$

$$\tfrac{3}{8}\mathrm{Si} + \tfrac{5}{8}\mathrm{Mo} \rightarrow \tfrac{1}{8}\mathrm{Mo_5Si_3} \qquad \Delta H_r = \tfrac{1}{8}(-313.5 \pm 12.0) = -39.2 \pm 1.5\ \mathrm{kJ} \quad \text{(A2b)}$$

$$\tfrac{2}{3}\mathrm{Si} + \tfrac{1}{3}\mathrm{Mo} \rightarrow \tfrac{1}{3}\mathrm{MoSi_2} \qquad \Delta H_r = \tfrac{1}{3}(-135.8 \pm 4.5) = -45.3 \pm 1.5\ \mathrm{kJ} \quad \text{(A2c)}$$

The molar coefficients in the above reactions are chosen such that there is one mole of atoms at either side of the equation. The standard enthalpies of formation of Mo_nSi_m indicated between brackets are taken from [141] and are in units of kJ per mole.

To our knowledge, the enthalpy of formation for RbSi has not been reported yet. However, the closely related Zintl compound of RbGe has a standard enthalpy of formation of -100.4 ± 4 kJ/mole [142] and the decomposition temperatures (onset of rapid Rb sublimation and conversion of Zintl phase into clathrate) of RbGe and RbSi are reported to be T_{dc} = 663 ± 5 and 623 ± 5 K, respectively [51]. Hence, by linear scaling, we estimate the standard enthalpy of formation of RbSi to be -94.3 ± 5.3 kJ/mole. Owing to the addition of Rb to Si, the reaction enthalpies for the formation of Mo_nSi_m phases at the interfaces between RbSi and Mo change considerably:

$$\tfrac{1}{5}\mathrm{RbSi} + \tfrac{3}{5}\mathrm{Mo} \rightarrow \tfrac{1}{5}\mathrm{Mo_3Si} + \tfrac{1}{5}\mathrm{Rb}$$
$$\Rightarrow \Delta H_r = \tfrac{1}{5}(-122.1 \pm 6.0) - \tfrac{1}{5}(-94.3 \pm 5.3) = -5.6 \pm 2.3\ \mathrm{kJ} \qquad \text{(A3a)}$$

$$\tfrac{3}{11}\mathrm{RbSi} + \tfrac{5}{11}\mathrm{Mo} \rightarrow \tfrac{1}{11}\mathrm{Mo_5Si_3} + \tfrac{3}{11}\mathrm{Rb}$$
$$\Rightarrow \Delta H_r = \tfrac{1}{11}(-313.5 \pm 12.0) - \tfrac{3}{11}(-94.3 \pm 5.3) = -2.8 \pm 2.5\ \mathrm{kJ} \qquad \text{(A3b)}$$

$$\tfrac{2}{5}\mathrm{RbSi} + \tfrac{1}{5}\mathrm{Mo} \rightarrow \tfrac{1}{5}\mathrm{MoSi_2} + \tfrac{2}{5}\mathrm{Rb}$$
$$\Rightarrow \Delta H_r = \tfrac{1}{5}(-135.8 \pm 4.5) - \tfrac{2}{5}(-94.3 \pm 5.3) = +10.6 \pm 3.0\ \mathrm{kJ} \qquad \text{(A3c)}$$

Again the molar coefficients are adjusted to give one mole of atoms at either side of the reaction equation.

Appendix B

Supplementary materials of Chapter 3.

B1. SEM images of thick Ru films sputter-deposited at low and high Ar pressures

Thick Ru films were deposited by DC magnetron sputtering at low (2.7×10^{-3} mbar) and high (2.7×10^{-2} mbar) Ar pressures, at a fixed power of 200 W. Characteristic SEM-images of the resulting films are shown in Figure B1.

Low-pressure-deposited Ru shows a dense and uniform microstructure, while high-pressure-deposited Ru shows a columnar and open strcuture. In particular, we find a great similarity of the low-pressure-deposited structures of Ru with those reported for Mo in [143]. From the SEM cross-sectional images (third row in Figure B1), we obtained the thicknesses of these films, of 183 nm and 212 nm for low- and high-pressure-deposited Ru, respectively.

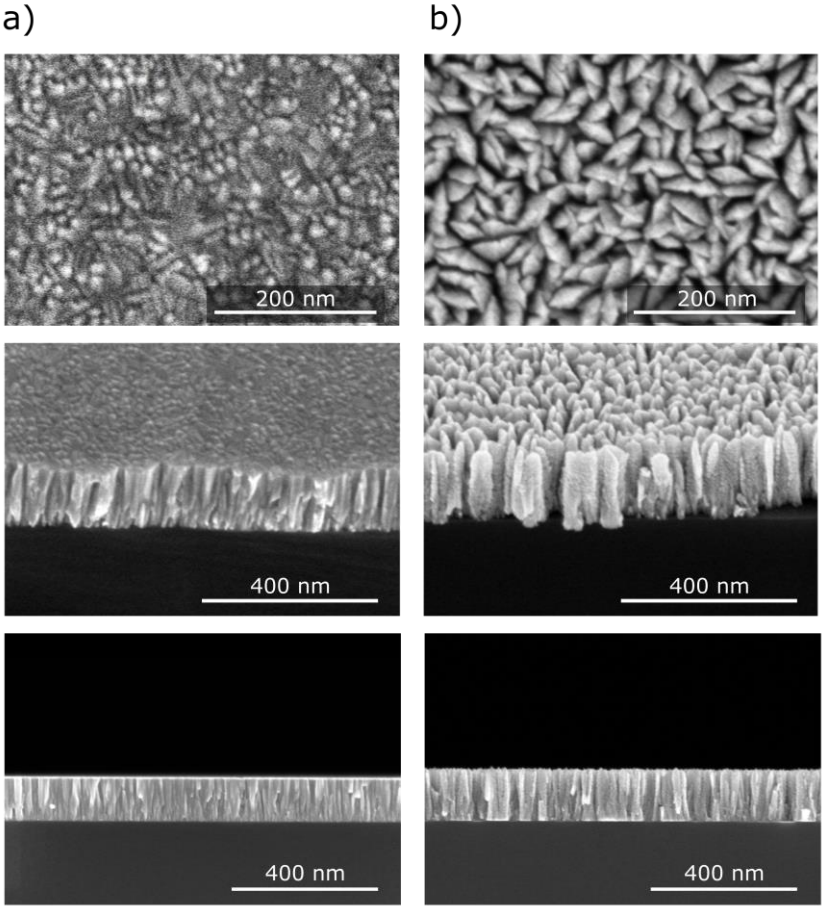

Figure B1 Top and cross-sectional views obtained with SEM of ~200 nm thick Ru films, sputter-deposited at Ar pressures of a) 2.7×10^{-3} mbar and b) 2.7×10^{-2} mbar.

B2. AFM Data Analysis

The quantitative data analysis of our AFM images was performed in Python. It is publicly available at https://github.com/cristinasfiligoj/PhD. This repository contains the AFM measurements, the scripts (Jupyter Notebooks) to analyze them and the library at the basis: "AFM_lib". The library was designed to read individual AFM images from their text files and to determine the height-difference correlation function $\mathbf{C_H(r)}$.

In order to remove the contribution of artefacts in the images, such as 'dust particles', we excluded rows with spurious outliers from the analysis. For that, we calculated the Z-score for every row, and deleted those rows that contained any height value that deviated significantly from the mean. The convention is to designate points as outliers when they have a Z-score beyond 3. However, after running the calculation for different Z-score values ranging from 3 to 7 (a number we declared in our script), we found that 3.5 would allow for enough tolerance, yet discarding outliers unrelated to intrinsic morphological variations. Note that the AFM data are usually collected as line scans along the x-axis that are concatenated together to form the two-dimensional image. Therefore, the scanning speed in the x direction is considerably higher than the scanning speed in the y direction. As a result, the statistical properties of AFM data are usually evaluated along the x profiles as these are less affected by low frequency noise and interference in the AFM measurement. We therefore calculated $\mathbf{C_H(r)}$ as $\mathbf{C_H(x)}$, evaluated along the fast-scanning axis, as the average square of the height difference between two points separated within a single row by a distance x, where the averaging is performed over all point pairs at this distance within the row and over all rows in the image. We then used a built-in function to fit the power law region of the $\mathbf{C_H(x)}$-curve, from which we could extract the Hurst exponent, H. The correlation length, ξ, was taken as the point of intersection between the asymptotic line w^2 (where w is the root mean square roughness) and the linear fit, in the double logarithmic plot.

In order to reduce statistical noise and check for consistency, for every $\mathbf{C_H(x)}$ curve, we acquired data from three AFM measurements at different locations on the surface. We then calculated the average values of the three morphological descriptors extracted from each of the three individual $\mathbf{C_H(x)}$ plots. For the graphic representation of the average $\mathbf{C_H(x)}$, we calculated the average of the three independent curves.

In Figure B2 we show the evolution of the average $C_H(x)$ as a function of temperature. The standard deviations are indicated by the faint color band underlying the curves. In some cases, these are so narrow, i.e. the standard deviations are so small, that these bands are difficult to recognize.

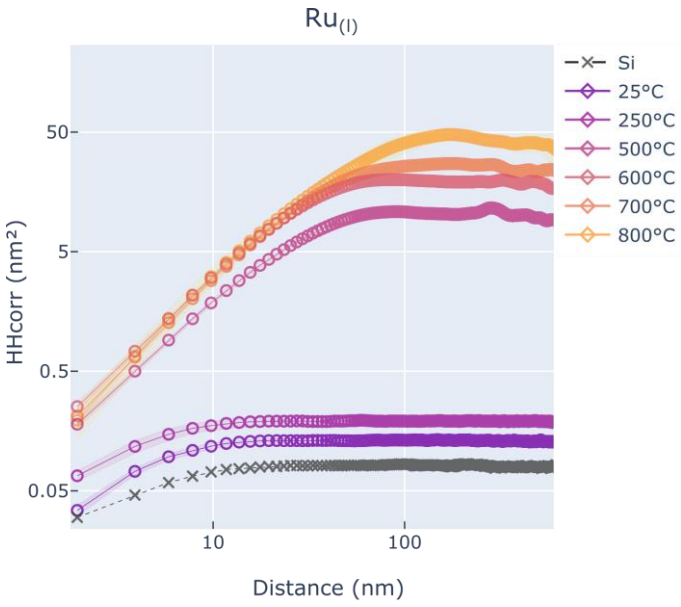

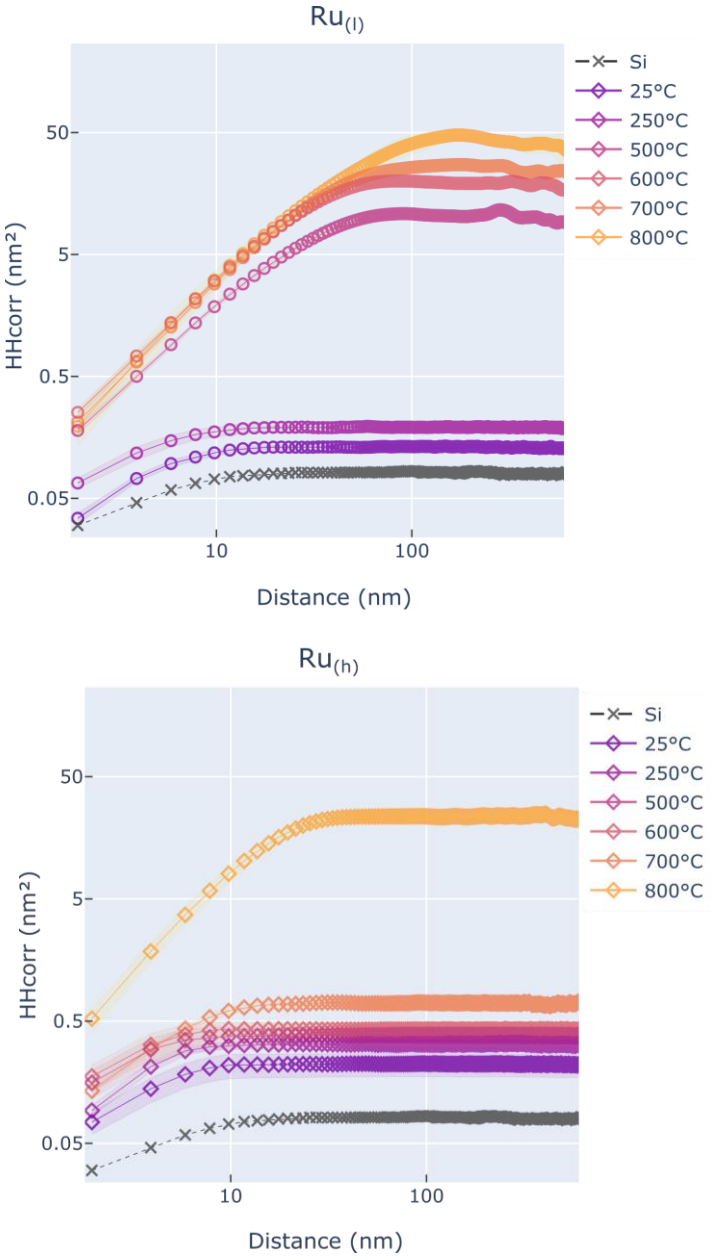

Figure B2 Thermal evolution of $C_H(x)$ for Ru(l) (top), Ru(h-l) (middle) and Ru(h) (bottom) films. The $C_H(x)$-curve of the Si substrate surface is also plotted and indicated by the gray crosses. The faint color bands indicate the standard deviations on the measured values.

B3. Elemental characterization by X-ray Photo-emission Spectroscopy (XPS) of Ru films before and after heating.

The compositions of the samples before and after annealing at 800°C were obtained by means of XPS, with a monochromatic Al K_α source (1486.6 eV) and a Scienta R4000 HiPP-3 analyzer. The background pressure during measurements was 5×10^{-9} mbar. The percentages of Si,Ru and O were obtained by fitting the peaks of wide-scan spectra, using the available 'UNIFIT 2018 Scientific' software.

Table B1 Elemental composition of Ru thin films sputter-deposited at Ar gas pressures of 2.7×10^{-3} mbar ($Ru_{(l)}$), 2.7×10^{-2} mbar followed by 2.7×10^{-3} mbar ($Ru_{(h\text{-}l)}$) and 2.7×10^{-2} mbar ($Ru_{(h)}$) . The percentages of Ru, Si, and O are indicated for samples before and after annealing at 800 °C for 30 minutes.

	$Ru_{(l)}$		$Ru_{(h\text{-}l)}$		$Ru_{(h)}$	
Element	As-dep.	800°C	As-dep.	800°C	As-dep.	800°C
Ru	65.07%	16.04%	65.33%	34.46%	67.32%	11.09%
Si	-	66.90%	-	52.37%	-	70.03%
O	34.93%	17.07%	34.67%	13.17%	32.68%	18.88%

B4. Additional SEM images.

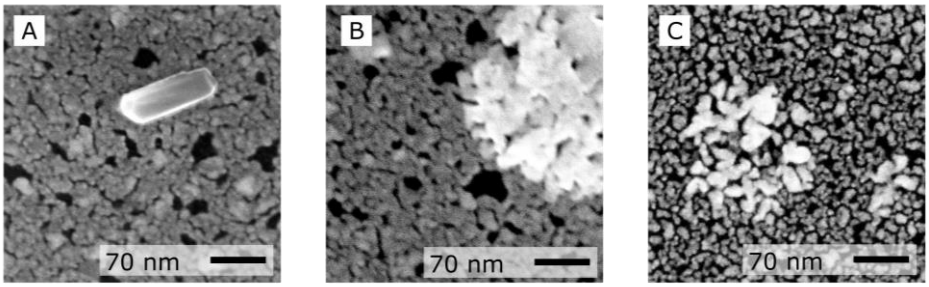

Figure B3 SEM micrographs of crystallites forming on the surface of $Ru_{(h-l)}$ (A and B) and $Ru_{(h)}$ (C) after annealing at 700 °C for 30 minutes.

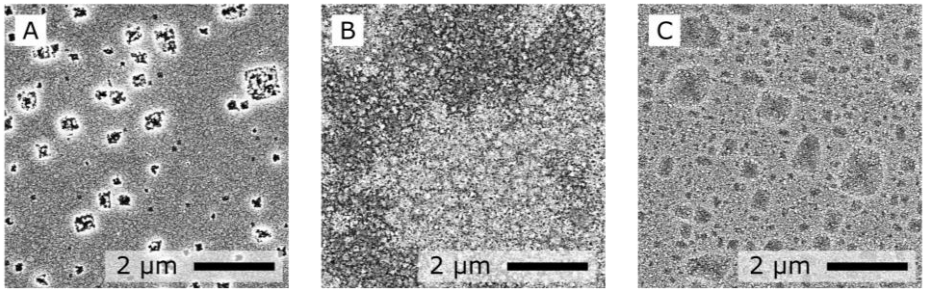

Figure B4 SEM images of Ru films deposited at working gas pressures of $Ru_{(l)}$ (A), $Ru_{(h-l)}$ (B) and $Ru_{(h)}$ (C), after annealing at 800 °C for 1 hour.

Appendix C

Supplementary material of Chapter 4.

C1. Stress measurement during silver deposition

Here, we present an additional measurement of the development of surface stress during thin-film growth, as measured with our multi-beam optical stress sensor. In this experiment, the stress was measured during the deposition of silver (Ag) on a Si(100) cantilever sample. Prior to the deposition, the surface oxide was removed and the surface was amorphized by Ar ion-bombardment.

The stress was recorded over a timespan of ~ 5 hours. After the first 10 minutes, the deposition was started. During the first 30 minutes of the deposition, the evaporator ion current was 20 nA, which corresponds to a deposition rate of roughly 0.01 nm/minute at the shallow incidence angle of 15 degrees [144]. The remainder of the deposition was performed at an ion current set at 40 nA, corresponding to a doubled deposition rate of approximately 0.02 nm/minute.

Silver on an amorphous Si surface is known to develop a polycrystalline structure. The typical stress evolution observed during the Volmer-Weber-type of growth of a high mobility material such as Ag is shown in the main text of Chapter 4 (see Figure 4.1) [145].

Figure C1 shows the evolution of F/w during the growth of Ag. By starting the deposition, the stress decreases slightly towards compressive values. As mentioned, capillary forces (surface tension) are known to lead to the emergence of compressive stress in the pre-coalescence stage of thin film growth [119]. After this, the stress changes to tensile and progressively increases during the deposition, without returning to compressive.

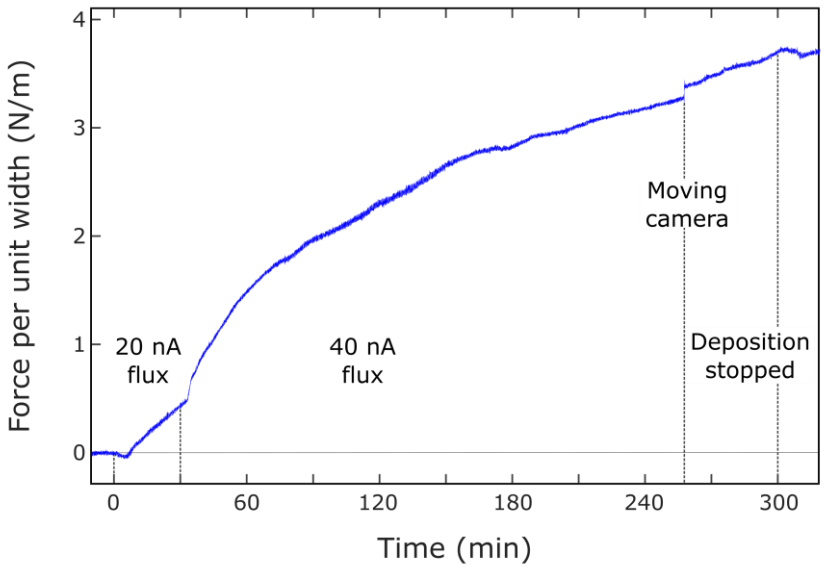

Figure C1 Force per unit width during silver deposition as a function of time. The deposition rate was doubled after 30 minutes the deposition was started. After 256 minutes the camera was moved because the spots were at the edge of the sensor.

At the deposition rates indicated above, after 300 minutes, the deposited layer is expected to be ~ 5.7 nm thick. This thickness is not expected to be enough to bring the silver film into the closure regime [146],[147], which might explain the absence of a final compressive regime in our experiment. In addition, it is known that deposition at grazing incidence angles can lead to enhanced surface roughness, due to the shadowing effect [148]. Due to this, the sides of the islands receive significantly less flux during the deposition. This is expected to lead to an extended coalescence stage, and it is likely responsible for the delay in the onset of the typical compressive stress regime.

References

[1] Jonas, G. *Arthur C. Clarke, Author Who Saw Science Fiction Become Real, Dies at 90.* The New York Times (March 19, 2008).

[2] Dafermos, C.M. *The second law of thermodynamics and stability.* Arch. Ration. Mech. Anal. **70**, 167 (1979).

[3] Van Schoot, J., Lok, S., van Setten, E., Maas, R., Troost, K., Peeters, R., Finders, J., Stoeldraijer, J., Benschop, J., Graeupner, P. and Kuerz, P., *High-NA EUV lithography exposure tool: advantages and program progress.* Extreme Ultraviolet Lithography **11517**, 1151712. International Society for Optics and Photonics (2021).

[4] Antonov, P. *Towards thermo- and superlubricity on the macroscopic scale: from nanostructures to graphite and graphene lubrication.* (PhD thesis, Leiden University, 2017).

[5] Kurilovich, D. *Laser-induced dynamics of liquid tin microdroplets.* (PhD thesis, Vrije Universiteit Amsterdam, 2019).

[6] Yu, Z. *Organotin Photoresists for extreme ultraviolet lithography.* (PhD thesis, University of Amsterdam, 2019).

[7] Boonzajer Flaes, D.E. *Reconstructive imaging based on indirect measurements From lensless imaging to waveguide analysis.* (PhD thesis, Vrije Universiteit Amsterdam, 2019).

[8] Haitjema, J. *Exciting tin-oxo cages: light-induced chemistry for nanopatterning.* (PhD thesis, University of Amsterdam, 2020).

[9] Torretti, F. *Spectroscopy of highly-charged Sn ions for extreme ultraviolet nanolithography.* (PhD thesis, Vrije Universiteit Amsterdam, 2019).

[10] Edward, S. *Detection of hidden gratings using light and sound.* (PhD thesis, University of Amsterdam, 2019).

[11] Scheers, J. *Charge-state-resolved spectroscopy of multiply-charged tin ions*. (PhD thesis, Vrije Universiteit Amsterdam, 2020).

[12] Wu, L. *Metal oxo clusters: molecular design for extreme ultraviolet lithography*. (PhD thesis, University of Amsterdam, 2020).

[13] Macleod, A. *The early days of optical coatings*. J. Opt. A: Pure Appl. Opt. **1**, 779(1999).

[14] Louis, E., Yakshin, A.E., Tsarfati, T., Bijkerk, F. *Nanometer interface and materials control for multilayer EUV-optical applications*. Prog. Surf. Sci. **86**, 255 (2011).

[15] Houweling, Z. S., Ande, C.K., De Graaf, D., Kater, T., Kuijken, M. A. J., Valefi, M. *EUV pellicles*. U.S. Patent Application No. 16/758,250 (2020).

[16] Ohring, M. *The Materials Science of Thin Films, 2nd Edition* (Academic Press, 2001).

[17] Wagendristel, A., Wang, Y. *An Introduction to Physics and Technology of Thin Films* (World scientific, 1994).

[18] Smith, D.L. *Thin-Film Deposition: Principles and Practice* (McGraw-Hill, 1995).

[19] Mehrer, H. *Diffusion in solids: fundamentals, methods, materials, diffusion-controlled processes* (Springer, 2007).

[20] Antczak, G., Ehrlich, G. *Surface Diffusion: Metals, Metal Atoms, and Clusters* (Cambridge University Press, 2010).

[21] Thompson, C.V., Floro, J., Smith, H.I. *Epitaxial grain growth in thin metal films*. J. Appl. Phys. **67**, 4099 (1990).

[22] Torchinsky, I., Rosenman, G. *Wettability Modification of Nanomaterials by Low-Energy Electron Flux*. Nanoscale Res. Lett. **4**, 1209 (2009).

[23] Cote, L.J., Kim, J., Zhang, Z., Sun, C., Huang, J. *Tunable assembly of graphene oxide surfactant sheets: wrinkles, overlaps and impacts on thin film properties*. Soft Matter **6**, 6096 (2010).

[24] Callister, W.D., William D.J., *Materials Science and Engineering: An Introduction* (Wiley, 2006).

[25] Cottrell, A. *An Introduction to Metallurgy* (CRC Press, 1997).

[26] Okamoto, H., Massalski, T.B. *Binary Alloy Phase Diagrams*. Binary Alloy Phase Diagrams (ASM International, 1990).

[27] Thornton, J.A., Hoffman, D.W. *Stress-related effects in thin films*. Thin Solid Films **171**, 5 (1989).

[28] Chason, E., Guduru, P.R. *Tutorial: Understanding residual stress in polycrystalline thin films through real-time measurements and physical models*. J. Appl. Phys. **119**, 191101 (2016).

[29] Stoney, G.G. *The tension of metallic films deposited by electrolysis*. Proc. R. Soc. London. A, **82**, 172 (1909).

[30] Polop, C., Vasco, E., Perrino, A.P., Garcia, R. *Mapping stress in polycrystals with sub-10 nm spatial resolution*. Nanoscale **9**, 13938 (2017).

[31] Louis, E., Yakshin, A.E., Goerts, P.C., Oestreich, S., Stuik, R., Maas, E.L., Kessels, M.J.H., Bijkerk, F., Haidl, M., Muellender, S. and Mertin, M. *Progress in Mo/Si multilayer coating technology for EUVL optics*. Proceedings Proceedings SPIE, **3997**, Emerging Lithographic Technologies IV**,** 406 (2000).

[32] Yakshin, A.E., Van De Kruijs, R.W.E., Nedelcu, I., Zoethout, E., Louis, E., Bijkerk, F., Enkisch, H. and Müllender, S. *Enhanced reflectance of interface engineered Mo/Si multilayers produced by thermal particle deposition*. Proceedings PIE **6517**, Emerging Lithographic Technologies XI, 65170 (2007).

[33] Bosgra, J., Zoethout, E., van der Eerden, A.M., Verhoeven, J., van de Kruijs, R.W., Yakshin, A.E. and Bijkerk, F. *Structural properties of subnanometer thick Y layers in extreme ultraviolet multilayer mirrors*. Appl. Opt. **51**, 8541 (2012).

[34] Chkhalo, N.I., Gusev, S.A., Nechay, A.N., Pariev, D.E., Polkovnikov, V.N., Salashchenko, N.N., Schäfers, F., Sertsu, M.G., Sokolov, A., Svechnikov, M.V. and Tatarsky, D.A. *High-reflection Mo/Be/Si multilayers for EUV lithography*. Opt. Lett. **42**, 5070 (2017).

[35] Kondratenko, V.V., Pershin, Y.P., Poltseva, O.V., Fedorenko, A.I., Zubarev, E.N., Yulin, S.A., Kozhevnikov, I.V., Sagitov, S.I., Chirkov, V.A., Levashov, V.E. and Vinogradov, A.V. *Thermal stability of soft x-ray Mo-Si and $MoSi_2$-Si multilayer mirrors*. Appl. Opt. **32**, 1811 (1993).

[36] Takenaka, H., Kawamura, T. *Thermal stability of Mo/C/Si/C multilayer soft X-ray mirrors.* J. Electron Spectros. Relat. Phenomena **80**, 381 (1996).

[37] Feigl, T., Yulin, S.A., Kaiser, N., Thielsch, R. *Magnetron sputtered EUV mirrors with high thermal stability.* Proceedings SPIE **3997**, Emerging Lithographic Technologies IV, 420 (2000).

[38] Fedorenko, A.I., Kondratenko, V.V., Palatnik, L.S., Yulin, S.A., Zubarev, E.N., Nikitskiy, V.P. and Ryabukha, S.B., *Space test of Mo-Si, $MoSi_2$-Si, W-Si, and WSi_2-Si x-ray multilayer mirrors on the Russian orbital station.* Proceedings SPIE **2453**, X-Ray Optics and Surface Science 11 (1995).

[39] Singh, M., Braat, J.J.M. *Design of multilayer extreme-ultraviolet mirrors for enhanced reflectivity.* Appl. Opt. **39**, 2189 (2000).

[40] Windt, D.L. *IMD-Software for modeling the optical properties of multilayer films.* Comput. Phys. **12**, 360 (1998).

[41] Hoffman, J.R., Bykanov, A.N., Khodykin, O.V., Ershov, A.I., Fomenkov, I.V., Partlo, W.N. and Myers, D.W. *LPP EUV conversion efficiency optimization.* Proceedings SPIE **5715**, Emerging Lithographic Technologies IX, 892 (2005).

[42] The integral reflectivities are all normalized to that of Mo/Si MLMs in the 12.5-14.5 nm spectral range. The integral reflectivity values for a single MLM and for a combination of 10 consecutive MLMs are, respectively: 48.9 and 1.68 (in units of $\% \cdot \mathrm{nm}$), for Mo/Si MLMs with ideally sharp and flat interfaces (see Table 2.1 and 2.2); these values drop to 37.6 and 0.584 (in units of $\% \cdot \mathrm{nm}$) for MLMs with modest interfacial diffuseness (see Table 2.3).

[43] Okamoto, H. *Be-Si (Beryllium-Silicon).* Phase Equilib. Diffus. **30,** 115 (2009).

[44] Schnering, H.G. von, Schwarz, M., Chang, J.H., Peters, K., Peters, E.M., Nesper, R. *Refinement of the crystal structures of the tetrahedrotetrasilicides K_4Si_4, Rb_4Si_4 and Cs_4Si_4.* Zeitschrift für Krist. - New Cryst. Struct. **220**, 555 (2005).

[45] Quéneau, V., Todorov, E., Sevov, S.C. *Synthesis and Structure of Isolated Silicon Clusters of Nine Atoms.* J. Am. Chem. Soc. **120**, 3263 (1998).

[46] Hoch, C., Wendorff, M., Röhr, C. *Synthesis and crystal structure of the tetrelides $A_{12}M_{17}$ (A=Na, K, Rb, Cs; M=Si, Ge, Sn) and A_4Pb_9 (A=K, Rb).* J. Alloys Compd. **361**, 206 (2003).

[47] Palenzona, A., Pani, M. *The phase diagram of the Sr–Si system.* J. Alloys Compd. **373**, 214 (2004).

[48] Ramachandran, G. K., McMillan, P. F., Dong, J., Sankey, O. F. *$K_{7.62(1)}Si_{46}$ and $Rb_{6.15(2)}Si_{46}$: Two Structure I Clathrates with Fully Occupied Framework Sites.* J. Solid State Chem. **154**, 626 (2000).

[49] Bulanova, M.V., Zheltov, P.N., Meleshevich, K.A., Saltykov, P. A., Effenberg, G., Tedenac, J.C. *Lanthanum–silicon system.* J. Alloys Compd. **329**, 214 (2001).

[50] Cros, C., Pouchard, M., Hagenmuller, P. *Sur une nouvelle famille de clathrates minéraux isotypes des hydrates de gaz et de liquides. Interprétation des résultats obtenus.* J. Solid State Chem. **2**, 570 (1970).

[51] Hohmann, E. *Silicide und Germanide der Alkalimetalle.* Zeitschrift fur Anorg. Chemie **257**, 113 (1948).

[52] Custer, J.S., Thompson, M.O., Jacobson, D.C., Poate, J.M., Roorda, S., Sinke, W.C. and Spaepen, F. *Density of amorphous Si.* Appl. Phys. Lett. **64**, 437 (1994).

[53] Henke, B.L., Gullikson, E.M., Davis, J.C. *X-Ray Interactions: Photoabsorption, Scattering, Transmission, and Reflection at E = 50-30000 eV, Z = 1-92.* At. Data Nucl. Data Tables **54**, 181 (1993).

[54] Siegbahn, H. *Electron spectroscopy for chemical analysis of liquids and solutions.* J. Phys. Chem. **89**, 897 (1985).

[55] Ghatikar, M.N., Padalia, B.D., Nayak, R.M. *Chemical shifts and effective charges in ternary and complex systems.* J. Phys. C Solid State Phys. **10**, 4173 (1977).

[56] Boer, F.R. de, Mattens, W. C. M., Boom, R., Miedema, A. R., and Niessen, A. K. *Cohesion in metals. Transition metal alloys,* the Netherlands (1988).

[57] Clemens, B.M., Nix, W.D., Ramaswamy, V. *Surface-energy-driven intermixing and its effect on the measurement of interface stress.* J. Appl. Phys. **87**, 2816 (2000).

[58] Fokkema, V. *Real-time scanning tunneling microscopy studies of thin film deposition and ion erosion.* (PhD thesis, Leiden University, 2011).

[59] Nedelcu, I., van de Kruijs, R.W.E., Yakshin, A.E., Bijkerk, F. *Temperature-dependent nanocrystal formation in Mo/Si multilayers.* Phys. Rev. B **76**, 245404 (2007).

[60] Yakshin, A.E., Louis, E., Görts, P.C., Maas, E.L.G. and Bijkerk, F. *Determination of the layered structure in Mo/Si multilayers by grazing incidence X-ray reflectometry.* Phys. B Condens. Matter **283**, 143–148 (2000).

[61] Moffatt, W.G. *'Mo-Rb'.* The Handbook of Binary Phase Diagrams 3/82 (Genium Pub. Corp., USA, 1978).

[62] Yulin, S., Feigl, T., Kuhlmann, T., Kaiser, N., Fedorenko, A.I., Kondratenko, V.V., Poltseva, O.V., Sevryukova, V.A., Zolotaryov, A.Y. and Zubarev, E.N., *Interlayer transition zones in Mo/Si superlattices.* J. Appl. Phys. **92**, 1216 (2002).

[63] Nedelcu, I., van de Kruijs, R.W.E., Yakshin, A.E., Bijkerk, F. *Thermally enhanced interdiffusion in MoSi multilayers.* J. Appl. Phys. **103**, 083549 (2008).

[64] Kuznetsov, A.S., Gleeson, M.A., Bijkerk, F. *Hydrogen-induced blistering mechanisms in thin film coatings.* J. Phys. Condens. Matter **24**, 052203 (2012).

[65] Schlatmann, R., Keppel, A., Xue, Y., Verhoeven, J., van der Wiel, M. J. *Enhanced reflectivity of soft x-ray multilayer mirrors by reduction of Si atomic density.* Appl. Phys. Lett. **63**, 3297 (1993).

[66] The work described in this chapter forms the basis of Patent. Nr. WO2017076694A1, entitled 'Multilayer reflector, method of manufacturing a multilayer reflector and lithographic apparatus'.

[67] Van Zwol, P.J., Vles, D.F., Voorthuijzen, W.P., Péter, M., Vermeulen, H., Van Der Zande, W.J., Sturm, J.M., van de Kruijs, R.W.E. and Bijkerk, F. *Emissivity of freestanding membranes with thin metal coatings.* J. Appl. Phys. **118**, 213107 (2015).

[68] Bajt, S., Chapman, H.N., Nguyen, N., Alameda, J., Robinson, J.C., Malinowski, M., Gullikson, E., Aquila, A., Tarrio, C. and Grantham, S. *Design and performance of capping layers for extreme-ultraviolet multilayer mirrors*. Appl. Opt. **42**, 5750 (2003).

[69] Sutter, P.W., Flege, J.I., Sutter, E.A. *Epitaxial graphene on ruthenium*. Nat. Mater. **7**, 406 (2008).

[70] Clarke, M.J. *Ruthenium metallopharmaceuticals*. Coord. Chem. Rev. **232**, 69 (2002).

[71] Ferrari, P., Rojas, S., Diaz-Droguett, D. E., Cabrera, A.L. *Evaporation of low-vapor pressure metals using a conventional mini electron beam evaporator*. Instrum. Sci. Technol. **42**, 142 (2014).

[72] Aaltonen, T., Alén, P., Ritala, M., Leskelä, M. *Ruthenium Thin Films Grown by Atomic Layer Deposition*. Chem. Vap. Depos. **9**, 45 (2003).

[73] Lee, W.K., Wong, H.Y., Chan, K.Y., Yong, T.K., Yap, S.S., Tou, T.Y. *Effects of laser fluence on the structural properties of pulsed laser deposited ruthenium thin films*. Appl. Phys. A **100**, 561 (2010).

[74] Arunagiri, T.N., Zhang, Y., Chyan, O., El-Bouanani, M., Kim, M.J., Chen, K.H., Wu, C.T. and Chen, L.C. *5nm ruthenium thin film as a directly plateable copper diffusion barrier*. Appl. Phys. Lett. **86**, 083104 (2005).

[75] Thornton, J.A. *The microstructure of sputter-deposited coatings*. J. Vac. Sci. Technol. A Vacuum, Surfaces, Film. **4**, 3059 (1986).

[76] Abadias, G., Chason, E., Keckes, J., Sebastiani, M., Thompson, G.B., Barthel, E., Doll, G.L., Murray, C.E., Stoessel, C.H. and Martinu, L. *Review Article: Stress in thin films and coatings: Current status, challenges, and prospects*. J. Vac. Sci. Technol. A Vacuum, Surfaces, Film. **36**, 020801 (2018).

[77] Alagoz, A.S., Kamminga, J.D., Grachev, S.Y., Lu, T.M., Karabacak, T. *Residual stress reduction in sputter deposited thin films by density modulation*. MRS Proceedings **1224,** 1 (2009).

[78] Kaemmar, S.B. *Introduction to Bruker's ScanAsyst and PeakForce Tapping AFM Technology*. Appl. note (2011).

[79] Bruker application note. *ScanAsyst^{TM} tip specifications*. https://www.brukerafmprobes.com/p-3726-scanasyst-air.aspx.

[80] Meakin, P. *The growth of rough surfaces and interfaces*. Phys. Rep. **235**, 189 (1993).

[81] Amorphous, C.O.F. *Characterization of Amorphous and Crystalline Rough Surface: Principles and Applications* Experimental Methods in the Physical Sciences (Elsevier, 2001).

[82] Meakin, P. *Fractals, scaling and growth far from equilibrium* Choice Reviews Online (Cambridge University Press, 1998).

[83] Michely, T., Krug, J. *Islands, Mounds and Atoms.* Thin Solid Films (Springer, 2012).

[84] Nakahara, S. *Microporosity induced by nucleation and growth processes in crystalline and non-crystalline films*. Thin Solid Films **45**, 421(1977).

[85] Yu, H.Z., Thompson, C.V. *Grain growth and complex stress evolution during Volmer–Weber growth of polycrystalline thin films*. Acta Mater. **67**, 189 (2014).

[86] Coloma Ribera, R., van de Kruijs, R.W.E., Kokke, S., Zoethout, E., Yakshin, A.E., Bijkerk, F. *Surface and sub-surface thermal oxidation of thin ruthenium films*. Appl. Phys. Lett. **105**, 131601 (2014).

[87] Gadkari, P.R., Warren, A.P., Todi, R.M., Petrova, R.V., Coffey, K.R. *Comparison of the agglomeration behavior of thin metallic films on SiO_2*. J. Vac. Sci. Technol. A Vacuum, Surfaces, Film. **23**, 1152 (2005).

[88] Meakin, P., Ramanlal, P., Sander, L.M., Ball, R.C. *Ballistic deposition on surfaces*. Phys. Rev. A **34**, 5091 (1986).

[89] Kardar, M., Parisi, G., Zhang, Y.C. *Dynamic Scaling of Growing Interfaces*. Phys. Rev. Lett. **56**, 889 (1986).

[90] Krim, J., Indekeu, J.O. *Roughness exponents: A paradox resolved*. Phys. Rev. E **48**, 1576 (1993).

[91] Aué, J., De Hosson, J.T.M. *Influence of atomic force microscope tip–sample interaction on the study of scaling behavior*. Appl. Phys. Lett. **71**, 1347 (1997).

[92] Rost, M.J., Quist, D.A., Frenken, J.W.M. *Grains, Growth, and Grooving*. Phys. Rev. Lett. **91**, 026101 (2003).

[93] Kwon, J.Y., Yoon, T.S., Kim, K.B., Min, S.H. *Comparison of the agglomeration behavior of Au and Cu films sputter deposited on silicon dioxide*. J. Appl. Phys. **93**, 3270 (2003).

[94] Bai, Y., Yan, L., Wang, J., Yin, Z., Chen, N., Wang, F. and Tan, Z.A. *Tailoring film agglomeration for preparation of silver nanoparticles with controlled morphology*. Mater. Des. **103**, 315 (2016).

[95] Mezey, L.Z., Giber, J. *The Surface Free Energies of Solid Chemical Elements: Calculation from Internal Free Enthalpies of Atomization*. Jpn. J. Appl. Phys. **21**, 1569 (1982).

[96] Perring, L., Bussy, F., Gachon, J.C., Feschotte, P. *The Ruthenium–Silicon system*. J. Alloys Compd. **284**, 198 (1999).

[97] Coloma Ribera, R., van de Kruijs, R.W.E., Sturm, J.M., Yakshin, A.E., Bijkerk, F. *In vacuo growth studies of Ru thin films on Si, SiN, and SiO_2 by high-sensitivity low energy ion scattering*. J. Appl. Phys. **120**, 065303 (2016).

[98] Pasquali, L., Mahne, N., Montecchi, M., Mattarello, V., Nannarone, S. *Formation and distribution of compounds at the Ru–Si(001) ultrathin film interface*. J. Appl. Phys. **105**, 044304 (2009).

[99] Buschinger, B., Guth, W., Weiden, M., Geibel, C., Steglich, F., Vescoli, V., Degiorgi, L., Wassilew-Reul, C. *RuSi: metal-semiconductor transition by change of structure*. J. Alloys Compd. **262–263**, 238 (1997).

[100] Petersson, C.S., Baglin, J.E.E., Dempsey, J.J., D'Heurle, F. M., La Placa, S.J. *Silicides of ruthenium and osmium: Thin film reactions, diffusion, nucleation, and stability*. J. Appl. Phys. **53**, 4866 (1982).

[101] Lenssen, D., Lenk, S., Bay, H., Mantl, S. *Molecular beam epitaxy of Ru_2Si_3 on silicon*. Thin Solid Films **371**, 66 (2000).

[102] Shudo, K., Ohno, S., Kawamura, N., Toramaru, M., Kobayashi, N., Miyamoto, Y. *Thermally formed Ru–Si nanostructures gron on Si(001) surface*. Surf. Rev. Lett. **20**, 1350018 (2013).

[103] Srolovitz, D.J., Goldiner, M.G. *The Thermodynamics and Kinetics of film agglomeration*. JOM **47**, 31 (1995).

[104] Abadias, G., Fillon, A., Colin, J.J., Michel, A., Jaouen, C. *Real-time stress evolution during early growth stages of sputter-deposited metal films: Influence of adatom mobility*. Vacuum **100**, 36 (2014).

[105] Windt, D.L., Brown, W.L., Volkert, C.A., Waskiewicz, W.K. *Variation in stress with background pressure in sputtered Mo/Si multilayer films*. J. Appl. Phys. **78**, 2423 (1995).

[106] D'Heurle, F.M. *Aluminum films deposited by rf sputtering*. Metall. Mater. Trans. B **1**, 725 (1970).

[107] Chason, E., Karlson, M., Colin, J.J., Magnfält, D., Sarakinos, K., Abadias, G. *A kinetic model for stress generation in thin films grown from energetic vapor fluxes*. J. Appl. Phys. **119**, 145307 (2016).

[108] Freitag, J.M., Clemens, B.M. *Stress evolution in Mo/Si multilayers for high-reflectivity extreme ultraviolet mirrors*. Appl. Phys. Lett. **73**, 43 (1998).

[109] Floro, J.A., Chason, E., Cammarata, R.C., Srolovitz, D.J. *Physical Origins of Intrinsic Stresses in Volmer–Weber Thin Films*. MRS Bull. **27**, 19 (2002).

[110] Spaepen, F. *Interfaces and stresses in thin films*. Acta Mater. **48**, 31 (2000).

[111] Erdem Alaca, B., Saif, M.T.A., Sehitoglu, H. *On the interface debond at the edge of a thin film on a thick substrate*. Acta Mater. **50**, 1197 (2002).

[112] Hutchinson, J.W., He, M.Y., Evans, A.G. *The influence of imperfections on the nucleation and propagation of buckling driven delaminations*. J. Mech. Phys. Solids **48**, 709 (2000).

[113] Malerba, C., Valentini, M., Ricardo, C.A., Rinaldi, A., Cappelletto, E., Scardi, P. and Mittiga, A., *Blistering in Cu_2ZnSnS_4 thin films: correlation with residual stresses*. Mater. Des. **108**, 725 (2016).

[114] Jagtap, P., Chason, E. *A unified kinetic model for stress relaxation and recovery during and after growth interruptions in polycrystalline thin films*. Acta Mater. **193**, 202 (2020).

[115] Rost, M.J., Van Baarle, G.J.C., Katan, A.J., Van Spengen, W.M., Schakel, P., Van Loo, W.A., Oosterkamp, T.H. and Frenken, J.W.M., *Video-rate scanning probe control challenges: setting the stage for a microscopy revolution*. Asian J. Control **11**, 110 (2009).

[116] Rost, M.J., Crama, L., Schakel, P., Van Tol, E., van Velzen-Williams, G.B.E.M., Overgauw, C.F., Ter Horst, H., Dekker, H., Okhuijsen, B., Seynen, M. and Vijftigschild, A. *Scanning probe microscopes go video rate and beyond*. Rev. Sci. Instrum. **76**, 053710 (2005).

[117] Laugier, M. *Intrinsic stress in thin films of vacuum evaporated LiF and ZnS using an improved cantilevered plate technique*. Vacuum **31**, 155 (1981).

[118] Cammarata, R.C., Trimble, T.M., Srolovitz, D.J. *Surface stress model for intrinsic stresses in thin films*. J. Mater. Res. **15**, 2468 (2000).

[119] Koch, R., Hu, D., Das, A.K. *Compressive Stress in Polycrystalline Volmer-Weber Films*. Phys. Rev. Lett. **94**, 146101 (2005).

[120] Abermann, R. *Measurements of the intrinsic stress in thin metal films*. Vacuum **41**, 1279 (1990).

[121] Saedi, A., Rost, M.J. *Thermodynamics of deposition flux-dependent intrinsic film stress*. Nat. Commun. **7**, 10733 (2016).

[122] Freund, L.B., Chason, E. *Model for stress generated upon contact of neighboring islands on the surface of a substrate*. J. Appl. Phys. **89**, 4866 (2001).

[123] Hoffman, R.W. *Stresses in thin films: The relevance of grain boundaries and impurities*. Thin Solid Films **34**, 185 (1976).

[124] Nix, W.D., Clemens, B.M. *Crystallite coalescence: A mechanism for intrinsic tensile stresses in thin films*. J. Mater. Res. **14**, 3467 (1999).

[125] Koch, R. *The intrinsic stress of polycrystalline and epitaxial thin metal films*. J. Phys. Condens. Matter **6**, 9519 (1994).

[126] Yu, H.Z., Thompson, C.V. *Grain growth and complex stress evolution during Volmer–Weber growth of polycrystalline thin films*. Acta Mater. **67**, 189–198 (2014).

[127] Chason, E., Sheldon, B.W., Freund, L.B., Floro, J.A., Hearne, S.J. *Origin of Compressive Residual Stress in Polycrystalline Thin Films*. Phys. Rev. Lett. **88**, 156103 (2002).

[128] Del Vecchio, A.L., Spaepen, F. *The effect of deposition rate on the intrinsic stress in copper and silver thin films*. J. Appl. Phys. **101**, 063518 (2007).

[129] Vasco, E., Ramírez-Peral, M.J., Michel, E.G., Polop, C. *Understanding the intrinsic compression in polycrystalline films through a mean-field atomistic model*. J. Phys. D. Appl. Phys. **54**, 065302 (2021).

[130] Welzel, U., Ligot, J., Lamparter, P., Vermeulen, A.C., Mittemeijer, E.J. *Stress analysis of polycrystalline thin films and surface regions by X-ray diffraction*. J. Appl. Crystallogr. **38**, 1 (2005).

[131] Luo, Q., Jones, A.H. *High-precision determination of residual stress of polycrystalline coatings using optimised XRD-sin2ψ technique*. Surf. Coatings Technol. **205**, 1403 (2010).

[132] Koch, R., Leonhard, H., Thurner, G., Abermann, R. *A UHV-compatible thin-film stress-measuring apparatus based on the cantilever beam principle*. Rev. Sci. Instrum. **61**, 3859 (1990).

[133] Pan, J.T., Blech, I. *In situ stress measurement of refractory metal silicides during sintering*. J. Appl. Phys. **55**, 2874 (1984).

[134] Schell-Sorokin, A., Tromp, R. *Mechanical stresses in (sub)monolayer epitaxial films*. Phys. Rev. Lett. **64**, 1039 (1990).

[135] Chason, E., Sheldon, B.W. *Monitoring Stress in Thin Films During Processing*. Surf. Eng. **19**, 387 (2003).

[136] Narushima, T., Kinahan, N.T., Boland, J.J. *Simultaneous scanning tunneling microscopy and stress measurements to elucidate the origins of surface forces*. Rev. Sci. Instrum. **78**, 053903 (2007).

[137] Wortman, J.J., Evans, R.A. *Young's Modulus, Shear Modulus, and Poisson's Ratio in Silicon and Germanium*. J. Appl. Phys. **36**, 153 (1965).

[138] The STM movie "Ru growth on Si", underlying the still frames of Figure 4.6, is available as supplementary material at http://www.youtube.com/arcnlnl. The movie plays 120 times faster than the rate at which it was recorded. In the movie, the deposition starts after 2 s.

[139] Huheey, L., Keiter, J.E., Keiter, E.A. *Inorganic chemistry: Principles of structure and reactivity (4th edition)* Journal of Chemical Education (Harper & Row, 1983).

[140] Waki, I., Hirai, Y. *The silicon L-edge photoabsorption spectrum of silicon carbide*. J. Phys. Condens. Matter **1**, 6755 (1989).

[141] Fujiwara, H., Ueda,Y. *Thermodynamic properties of molybdenum silicides by molten electrolyte EMF measurements*. J. Alloys Compd. **441**, 168 (2007).

[142] Chuntonov, K., Yatsenko, S.P., Bushmanov, V.D. *Heats of Formation of Equiatomic Compounds of Rb and Non-Transition Group IV Elements*. Russ. J. Phys. Chem. **52**, 902 (1978).

[143] Akcay, N., Akin Sonmez, N., Zaretskaya, E.P., Ozcelik, S. *Influence of deposition pressure and power on characteristics of RF-Sputtered Mo films and investigation of sodium diffusion in the films*. Curr. Appl. Phys. **18**, 491 (2018).

[144] Mini e-beam evaporator from Oxford Applied Research, Witney, UK. http://www.oaresearch.co.uk/oaresearch/ebeam/.

[145] Koch, R., Winau, D., Führmann, A., Rieder, K. *Intrinsic stress of polycrystalline and epitaxial Ag, Cu and Au films on mica (001)*. Vacuum **43**, 521 (1992).

[146] Floro, J.A., Hearne, S.J., Hunter, J.A., Kotula, P., Chason, E., Seel, S.C. and Thompson, C.V. *The dynamic competition between stress generation and relaxation mechanisms during coalescence of Volmer–Weber thin films*. J. Appl. Phys. **89**, 4886 (2001).

[147] Abermann, R., Koch, R. *The internal stress in thin silver, copper and gold films*. Thin Solid Films **129**, 71 (1985).

[148] Rechendorff, K., Hovgaard, M.B., Chevallier, J., Foss, M., Besenbacher, F. *Tantalum films with well-controlled roughness grown by oblique incidence deposition*. Appl. Phys. Lett. **87**, 073105 (2005).

[149] Bajek, D., Wackerow, S., Zanin, D.A., Baudin, L., Bogdanowicz, K., Valdivieso, E.G.T., Calatroni, S., Di Girolamo, B., Sitko, M., Himmerlich, M. and Taborelli, M. *Role of surface microgeometries on electron escape probability and secondary electron yield of metal surfaces*. Sci. Rep. **10**, 250 (2020).

[150] Thornton, J.A. *Influence of apparatus geometry and deposition conditions on the structure and topography of thick sputtered coatings*. J. Vac. Sci. Technol. **11**, 666–670 (1974).

Summary

This thesis revolves around the question: what determines the stability of ultrathin films? To address this question, I explored three different approaches, one based on theory (Chapter 2), one on fabrication methods (Chapter 3) and one based on instrumentation (Chapter 4). The subject and the specific materials that have been investigated, were directly inspired by the goal of improving the efficiency and lifetime of the EUV optics, applied to the field of next-generation photolithography.

In Chapter 2, I proposed a theoretical method for approaching a known problem in Mo/Si multilayer mirrors, which is the intermixing and roughening at the interfaces. Our proposed solution is to substitute the pure Si layer with a silicide compound, which has the promise that it might partly or even completely prevent the interaction between the multilayer materials. Among the possible candidates, we find rubidium to be very promising. It forms a silicide that improves the thermodynamic stability with respect to the formation of silicides with Mo, which is the desired effect. In addition, the rubidium silicide also introduces favorable EUV-optical properties. With this material choice, we expect that it should be possible to improve the EUV reflectivity with respect to regular Mo/Si multilayer mirrors, which could significantly increase the throughput of EUV light and, thereby, the throughput of illuminated semiconductor wafers, in comparison with current EUV lithography machines.

In Chapter 3 I investigated the influence of the fabrication conditions on the thermal stability of ruthenium (Ru) nanolayers, deposited by DC magnetron sputtering. This study is of potential relevance in the context of the lifetime of EUV pellicles, membranes with a thickness of only a few tens of nanometers that are used in transmission. At high temperatures, the Ru layers that are used in some of these membranes can suffer from dewetting and even rupturing. We varied the pressure of the working gas

(Ar), applied during sputter deposition. This pressure is known to affect the physical properties of the film, such as its initial structure and internal stress. To study the thermal stability of the films, we accelerated the aging process by submitting the Ru nanolayers to elevated temperatures. By comparing the film morphologies before and after a heat treatment, we found that the films that had been deposited at high Ar pressures, or partly at a high pressure and partly at a low pressure, are more thermodynamically stable than those that had been deposited at low Ar pressures. Possible mechanisms were discussed that could underly the difference in evolution, with special attention to the role played by the initial grain boundary configuration, originating from the sputter deposition conditions.

In Chapter 4, I presented a novel experimental setup, designed to explore the atomistic processes/mechanisms underlying the origin of stress in thin films. The setup features the combination of a scanning tunneling microscope for real-time imaging of a surface during film deposition and a multi-beam optical stress sensor for simultaneous, in-situ monitoring of the stress-induced substrate bending. This system makes it possible to directly correlate the atomic-scale processes that dominate the development of structure and morphology in thin films during their deposition with the evolution of stress, starting from the earliest stages of the film's growth – a combination that has never been achieved before. As a proof-of-principle experiment, we deposited thin Ru films by e-beam evaporation on a thin, cantilever-shaped silicon substrate and followed this deposition with STM and stress measurements.

In conclusion, using experimental and theoretical tools, I shined more light on the mechanisms underlying the formation of ultrathin films and their thermodynamic stability.

Samenvatting

Dit proefschrift is gewijd aan de vraag: wat is bepalend voor de stabiliteit van ultradunne lagen? Ik heb dit vraagstuk op drie verschillende manieren benaderd, eenmaal op basis van theorie (Hoofdstuk 2), eenmaal via de fabricagemethodes van dunne lagen (Hoofdstuk 3) en eenmaal op basis van nieuwe instrumentatie (Hoofdstuk 4). Het hoofdonderwerp en de specifieke materialen die ik heb bestudeerd werden direct geïnspireerd door de wens om de werkzaamheid en levensduur te vergroten van zogenaamde EUV-optiek, die zijn toepassing o.a. vindt bij moderne en toekomstige fotolithografie.

In Hoofdstuk 2 stel ik een theoretische aanpak voor om een bekend probleem op te lossen of minder ernstig te maken, dat optreedt bij Mo/Si multilaag-spiegels, namelijk de vermenging en verruwing aan de grensvlakken. Onze oplossing bestaat uit de vervanging van de pure Si laag door een verbinding, een silicide, hetgeen de belofte in zich heeft dat daarmee de ongewenste interactie tussen de materialen in de multilaagstructuur geheel of gedeeltelijk kan worden voorkomen. Onder de mogelijke kandidaten identificeren wij vooral rubidium als veelbelovend materiaal. Het vormt een silicide dat de thermodynamische stabiliteit verhoogt ten opzichte van de vorming van silicides met Mo, hetgeen het gewenste effect is. Bovendien blijkt rubidium silicide gunstige EUV-optische eigenschappen met zich mee te brengen. We verwachten daarom dat het met deze materiaalkeuze zelfs mogelijk zou moeten zijn om de EUV-reflectiviteit te verbeteren in vergelijking met de gebruikelijke Mo/Si multilaag-spiegels. Dit zou dus naast een verbetering in de levensduur ook een significante verbetering kunnen opleveren van de transmissie van EUV-licht en daardoor van de doorstroom van belichte halfgeleiderplakken, ten opzichte van de huidige EUV-lithografiemachines.

In Hoofdstuk 3 onderzocht ik de invloed van de fabricage-omstandigheden op de thermische stabiliteit van ruthenium (Ru) nanolagen die aangebracht worden met de welbekende methode van DC-magnetron-sputterdepositie. Deze studie is van mogelijk belang binnen de context van de levensduur van EUV-pellicles, vrijstaande membranen met een dikte van slechts enkele tientallen nanometers, die in een transmissiegeometrie worden toegepast. Bij hoge temperaturen kunnen de Ru-lagen, die in sommige van deze membranen worden gebruikt, opbreken in druppeltjes, een proces dat bekend staat onder de Engelse naam 'dewetting', en zelfs scheuren. We varieerden de druk van het werkgas, argon (Ar), dat bij de sputterdepositie werd gebruikt. Het is bekend dat deze druk de fysieke eigenschappen van de nanolaag beïnvloedt, zoals de structuur en de mechanische spanning. Om een beeld te krijgen van de thermische stabiliteit van de lagen, versnelden we het verouderingsproces door de Ru-nanolagen opzettelijk te onderwerpen aan hoge temperaturen. Uit een vergelijking van de laagstructuren vóór en na een dergelijke hittebehandeling, vonden we dat lagen die gedeponeerd worden bij een hoge Ar-druk, of voor het eerste deel bij een hoge druk en voor de rest bij een lage druk, een betere thermodynamische stabiliteit vertonen dan lagen die bij een lage Ar-druk worden aangebracht. In het hoofdstuk worden mechanismen besproken die verantwoordelijk kunnen zijn voor het verschil in evolutie van de lagen en die hun oorsprong kunnen vinden in het verschil in de sputterdepositie-omstandigheden.

In Hoofdstuk 4, presenteerde ik een nieuwe experimenteeropstelling, die ontworpen is om de atomaire processen en mechanismen te onderzoeken die ten grondslag liggen aan de mechanische spanning in dunne lagen. Bijzonder aan deze opstelling is de combinatie van een rastertunnelmicroscoop, waarmee een oppervlak 'real-time' kan worden afgebeeld, tijdens de depositie van een nanolaag, en een optisch systeem met meervoudige lichtbundels voor de gelijktijdige meting van de kromtrekking van het substraat onder invloed van de spanning die de gedeponeerde nanolaag introduceert. Deze unieke combinatie maakt het voor het eerst mogelijk om de atomaire-schaal processen die tijdens de depositie bepalend zijn voor de vorming van de structuur en morfologie van dunne lagen te correleren met de opbouw van mechanische spanning, vanaf de vroegste stadia van de laaggroei. Bij wijze van 'proof of principle'

experiment, deponeerden wij dunne Ru-lagen met behulp van een elektronenstraalverdamper op een dun siliciumsubstraat, dat we een vorm hadden gegeven die de vrijheid had om te verbuigen. De depositie kon met zowel STM als met spanningsmetingen in detail worden gevolgd.

De hier samengevatte combinatie van experiment en theorie stelde mij in staat om meer licht te werpen op de mechanismen die een rol spelen bij de vorming van ultradunne lagen en bij hun thermodynamische stabiliteit.

List of publications

- *Effect of rubidium incorporation on the EUV optical properties and intermixing in Mo/Si multilayer mirrors*, M. Saedi[**], C. Sfiligoj[**], J. Verhoeven, J.W.M. Frenken, Applied Surface Science, **507**, 144951 (2020). (Chapter 2)

- *Multilayer reflector, method of manufacturing a multilayer reflector and lithographic apparatus,* M. Saedi, J.M.W. Frenken, C. Sfiligoj, J. Verhoeven, Patent No. WO2017076694A1 (2017). (Chapter 2)

- *Ruthenium nanolayers under heat – the influence of the sputtering pressure on the thermal stability,* C. Sfiligoj, G. Yetik, J.W.M. Frenken, In preparation (2021). (Chapter 3)

- *A combined STM and stress sensor setup for real-time studies of thin film growth,* M. Saedi[**], C. Sfiligoj[**], M. van Stee, V. Vollema, G. Verdoes, M. Rost, J.W.M. Frenken, In preparation (2021). (Chapter 4)

[**] The first two authors contributed equally to this publication

Acknowledgements

Towards the end of my PhD, my supervisor used to encourage me by jokingly comparing to a runner just few kilometers away from the finish line of a marathon. Today I can finally say that I made it! And that it would have been impossible to do so without the help and support of the incredible group of people I was accompanied by along the way.

First of all, I would like to thank my supervisor, Joost, for taking me under his guidance. Thank you, Joost, for keeping me motivated and inspired. Our Monday meetings, discussing the fundamentals, grew my passion for materials science. Thank you for explaining how surfaces behave by giving life and personality to those atoms. Thank you also for being a great director for ARCNL. I believe our institute really needed someone with your strength and perseverance. Marjan, if ARCNL managed to stay strong it is also thanks to you. Thank you for encouraging me with your kindness and firmness in the most difficult moments. Paul, I was very happy when you joined ARCNL, thinking back at your lectures on THz technology in Delft. I'm glad you accepted the task of accompanying me until the finish line. Thank you also for the times you joined our table at lunch feeding us with interesting topics. I would like to thank also all the other professors at ARCNL, for their questions on my work and the inspiring research. Petra, Roland, Daniel, Marcelo, Mark, thank you for being part of my committee and reading this manuscript.

My PhD project would have not been possible without the driving force provided by ASML. Wim, thank you for bridging the research between ARCNL and ASML, feeding our institute with freshly-baked problems to solve. I look back with excitement at the days of the FEL consortium (ASML, UTwente, Zeiss) and the meeting in Hamburg. Gosse and Silvester, thank you for the open communication, giving direction and

purpose to my research and that of the group. I would like to thank also all the other collaborators for the constructive discussions, in particular Eric, Edgar, Maarten, Maria, Andrey Z. and Y., Fred, and Hartmut.

To my Nanolayers group, I am proud and happy to have worked with you. Mehdi, I'm deeply indebted to you: thank you for teaching me an enormous amount about STM and thin films, for all the insight and feedback. Your humour made it a joy to work in the lab, even the continuous reparations on our Naughtylus STM submarine. Your humblness and broad culture are very inspiring to me. Victor, I am glad you decided to stay for a PhD after your Master's, and work together on the STM. Your presence was precious for solving those technical issues with methodology and a good dose of laughs. Görsel, thank you for the XPS measures on my Ru nanolayers, for the moral support with our STMs and for being my paranymph (more on that later). Pavel, thank you for introducing me to AFM and for making me feel immediately welcome by inviting me to your wedding in the first week of my PhD. Renfeng, thank you taking care of my well-being. Arend-Jan, thanks for all the support in the lab, for your dedication, kindness and hard work. Thanks also to Reinout, Thomas, Nik, for your technical support, and for bringing much more creativity and positive energy into ARCNL. Jan, thank you for all your jokes and all your kindness. For sparking so many new ideas. For your passion for research, with which you continue to inspire everyone around you, even after your retirement. I hope that in the future I will be able to 'borrow' parts from other groups and forge second-hand incredible setups, like you do.

To my foster group in Leiden, thank you for giving a great start to my PhD adventure. Marcel, thank you for crafting our STM, together with Vincent. Gijsbert, for the help with the moving and for the innumerous fixes on the sample holder that still followed. For setting up the new lab in Amsterdam I wish to deeply thank also Hinco and Thomas C.S.. Gertjan, for the assistance with the STM electronics and support. Unforgettable were the paint ball outing, the barbecue and coffee breaks with a (lab) view, also with Ellie, Irene, Pavel, Matthijs, Dirk, Rik, Sander, and Tjerk.

To my ARCNL crew, we worked on quite different topics, nonetheless this diversity helped me hugely to get a broader perspective. Thank you for teaching me about all the ingredients for a EUV lithography machine.

Stephen, thank you for our small collaboration on ruthenium and for your calm presence and wit. Vanessa, for your prompt help with the final touches to my thesis, as well as for lifting the atmosphere with your wild curliness and warm smile, two sides of the same coin (cit.). Fiona, for being my office mate in the old and the new building, for your British expressions, and for your unfading smile. Thank you to Cathelijne, Romy and Rosa for your warm daily welcome and the administrative support. Thank you to the PV, my lunchtime circle, my fussball enemies, and all my ARCNL-lers, for making my PhD days much brighter.

AMOLF, thank you for being, quite literally, always by our side while we grew into a mature institute. I'd like to thank in particular the fine mechanics, design, electronics and software departments, for their vital help. Hans, Andries, Bob, Charles, and Dimitri, thank you for allowing magic to happen in the cleanroom and for sharing your wisdom with me. Henk-Jan, thank you, not only for the technical drawings, but more importantly for your friendship. Thank you for the tools and tips you offered for the works around my house, and for your unforgettable wedding in Texel.

AMOLF gave me the pleasure to meet many good friends and colleagues. Simone, Maga, Adeline, Jeanette, Old Ale, Nicola, Sebastian, Benjamin and Galja, Claire, Giuli Giubs & Judith, Oleg, Giorgione and Andrea, Marco, Lorenzo, Mario and Olga, Roberto and Katia, Giada, thank you all for being a big source of inspiration and fun times. Lutz, thank you for enjoying our introversion together and for amusing me with your creative side projects. Lukas, thank you for being a truly unconventional friend, for your passion for experimentation, for helping me release the tension, and for the sourdough yeast, starter of many loaves of bread.

A very special group of friends made my PhD journey incredibly precious. My sciencegirls, thank you for being my lifeboat, my crazy catamaran, and my peaceful raft. Agata, thank you for your funny anecdotes, truthfulness, and pragmatism. You gave me strength beyond imagination. Thank you also for generating so many nice plans, from a yoga class to a night at the opera. Jenny, you are my Sunshine, spreading good mood also on rainy days. Thank you for teaching me to trust more, myself and others. Parisa, your colourful elegance matches you so well. Thank you for the

determination you infuse, for reminding me to fight hard and voice my opinions. I look forward to reunite soon, 'somewhere sunny', and to discover what the future holds for us!

Görsel and Federica, I'm very lucky to have you by my side on the big day. Görsel, thank you for always making my mood with your extremely dark sense of humour and for the never boring conversations. For always being there for me, yet giving me a good shake when I needed it. My movie and music repertory also would like to thank you. Fede, Thank you for the long chatty walks, for your witty jokes, and your heartwarming presence. For inspiring me with your thirst for books and travelling.

My climbing buddies, Wing, Felix, Sunil, thank you for all the times you caught my falls, pushed me higher, celebrated with drinks and cakes. Mic, your style was so funny – squeezing your eyes to actually see the grips – but somehow so effective. Thank you for the climbs and for being the host of the most amazing nights I had in Amsterdam, at Levantkade!, together with Jacopo and Pepe. For the food, coast-to-coasts, movie nights, music. Thanks also to Titta & Tark, Steven and Bertus. Fra and Dieh, thank you for making life of those around you more beautiful and more meaningful.

Two tiny excursions helped me regain momentum. Astrid, Yvon, Ronaldo, Mario, Redmond, Tadeo and Tommaso, thank you for being one of the most diverse and incredible group of people I had the pleasure to work with, and for you hard-core friendship born from the MIT bootcamp. Yogis, Anne and Liisa (my Yin and my Yang), thank you being my peace and my energy. Maarten, I'm very thankful for the meditations and the unforgettable "make it playful".

Thank you to my Italian friends for providing a solid anchor to my old sea. Zizza, Barbara, Giorgia, Eli, Carlotta, for always being there for me, for the laughs and the tears. Fede, Butti Acci, Blade, Giulio grazie per le visite, gli spritz in allegria, e l'amicizia sincera sin dai tempi del liceo. Giulia, Tere, Roland, Benedetta, Fabai, for the long chats, the laughter, the hospitality. Ste, for being a very special person. Sarita, per essere come una seconda sorella, con cui condividere pazzie e sviscerare problemi. Mi familia Granaina, por los viajes, las bromas, las memorias mas bonitas. Peppe, Metiu, for keeping each other good company, in this wandering of ours.

Nii, Shoshan, Gonçalo, Merijn, Jurren, thank you for our good old Dutch friendship, you are incredible. Nathan, thank you for your contagious laugh and sweetness, giving me happiness and tranquillity. Akira, your ways of communicating science still are polar star to me.

Max and Maien, Cole and Nilou, Nick and Katie, thank you for all the adventures. I loved exploring nature with you. Chiara e Dre, thank you for your sweetness, silly jokes, and for making me feel at home. Douwe, Sevgi, Marica, Andrea e Marcella, Fabio, MC, Cocca e Doro, for hanging out with me and being so important also for Luca.

Of course my education started before I came to ARCNL, and I thank Andrea, Akira, and Erik, for being great mentors. Andrea, in your group I made the first step into the world of steel machines, noisy pumps and million cables, and loved it from the start. Akira, your playful ways for conveying science using toy models, together with your enthusiasm and rigour, still are a polar star to me. Erik, thank you for the fun and productive intership in your group, which showed me what nanowries are capable of!

To my colleagues and friends at QuTech, thank you for welcoming me in your team and fuelling me with excitement and motivation. Leo, I'm very thankful my journey can continue with you.

Luca, amore, thank you for illuminating my journey with your knoweldge, energy and smile. Thank you for all you've taught me, by showing me the beauty in any task, from chopping veggies to codying with Python. For cheering me up with your jokes and offering me your shoulder (il posto più bello del mondo). For encouraging me to go beyond my limits. Grazie infinite anche alla tua famiglia, per avermi ospitata in un sogno fatto di tanto calore, cibo buono, e romagnolità.

Infine, grazie alla mia famiglia, per le tutto l'affetto, il sostegno e le risate. Papà, grazie per avere sempre creduto in me, per avermi trasmesso la tua passione per le nanotecnologie e l'innovazione, per avermi insegnato il valore del rispetto e della collaborazione. Sorella, grazie per la nostra intesa di sorelle bandiera, ma soprattutto per la fiducia totale che posso riporre in te, che mi consente continuamente di migliorare e accettare nuove sfide.

Grazie anche ad Alberto, Giacomino e Carletto, perchè vi voglio un bene infinito. Paloma, grazie per essere entrata a fare parte della nostra famiglia.

Mamma, grazie per essere la mia forza e guida interiore. Per avermi insegnato ad arrivare fino in fondo ad ogni sfida, e ad affrontarla con coraggio e con speranza.